A free-running oscillator times and executes centriole biogenesis

Mustafa G. Aydogan[1], Thomas L. Steinacker[1], Mohammad Mofatteh[1], Lisa Gartenmann[1], Alan Wainman[1], Saroj Saurya[1], Paul T. Conduit[1,†], Felix Y. Zhou[2], Michael A. Boemo[1,*], Jordan W. Raff[1,*]

Affiliation:

[1]Sir William Dunn School of Pathology, University of Oxford, Oxford, UK.

[2]Ludwig Institute for Cancer Research, University of Oxford, Oxford, UK.

*Corresponding author. E-mail: michael.boemo@path.ox.ac.uk (MAB); jordan.raff@path.ox.ac.uk (JWR)

[†]Present address: Department of Zoology, University of Cambridge, Cambridge, UK.

Keywords:

Organelle biogenesis, organelle sizing, centriole duplication, cell cycle, biological oscillator, biological timing.

Abbreviations and symbols:

A: Amplitude; ***T***: Full width at half maximum; **Ω**: Area under the curve; **CCO**: Cdk-cyclin oscillator

Abstract

The accurate timing of organelle biogenesis and the precise regulation of organelle size are crucial for cell physiology. Centriole biogenesis initiates exclusively in S-phase, when a daughter centriole emerges from the side of a pre-existing mother and grows until it reaches its mother's size. This process is regulated by Polo-like kinase 4 (Plk4), which is recruited to centrioles in oscillatory waves in flies and human cells [1,2]. The nature and function of Plk4 oscillations is, however, unknown. Here we discover that Plk4 forms an adaptive oscillator at the base of the growing centriole, whose function is to time and set the duration of centriole biogenesis in *Drosophila* embryos. We demonstrate that the Plk4 oscillator is free-running of, but is entrained and calibrated by, the core Cdk/Cyclin cell-cycle oscillator, explaining how centrioles can duplicate independently of the cell cycle [3-5]. Mathematical modelling and further experiments indicate that the Plk4 oscillator is generated by a time-delayed negative-feedback loop in which Plk4 recruitment to, and dissociation from, the centriole is monitored via changes in the affinity-state of its centriolar receptor, Asterless. We postulate that such organelle-specific autonomous oscillators could regulate the timing and execution of organelle biogenesis more generally.

Main text

Albert Claude's landmark paper [6] challenged the idea that cells are a mere bag of enzymes whose contents grow freely in the cytoplasm with no active regulation. We now appreciate the diverse and compact nature of the many organelles in the cytoplasm [7], yet the physical mechanisms that regulate the amount and size of these organelles remain largely unknown.

In order to study the question of organelle size control, we recently established the *Drosophila* centriole as a model, whose linear structure makes its size easy to define and measure [1]. Most cells are born with a single centriole pair that duplicates precisely once during S-phase, when a single daughter centriole grows out from each mother [8]. To monitor the dynamics of centriole growth, we used living *Drosophila* embryos where hundreds of centrioles duplicate in near-synchrony in a common cytoplasm [9]. Centriole growth in these embryos is homeostatic: when centrioles grow slowly, they grow for a longer period; when centrioles grow quickly, they grow for a shorter period. As a result, centrioles grow to a consistent size. The centriolar kinase Plk4 is essential for this process and helps to establish the inverse relationship between the rate and period of centriole growth [1]. Plk4 can regulate the rate of centriole growth, because it phosphorylates Ana2/STIL to promote centriole assembly [10-12]. But, how Plk4 might regulate the period of centriole growth remains unknown.

It has recently been shown that centriolar Plk4 levels oscillate in both fly embryos and human cultured cells, but the significance of these oscillations is

unclear [1,2]. To investigate the physical nature of these oscillations, we generated flies transgenically expressing Plk4-mNeonGreen (Plk4-NG) under the control of its own promoter in a *Plk4* mutant background and monitored Plk4-NG recruitment to centrioles over nuclear cycles 11-13 in living embryos (Figs. 1, A and B, S1 and S2, and Movie S1). Plk4-NG oscillations were maximal in early-mid S-phase and minimal by the start of mitosis, and they showed evidence of adaptive behaviour: the amplitude (*A*) of the oscillations dampened during successive cycles, while their period—as judged by the full width at half maximum amplitude (*T*)—lengthened, so that the total amount of Plk4 recruited to centrioles remained approximately the same over each cell cycle (i.e., the area under the oscillation curve, Ω) (Fig. 1C). Moreover, *A* and *T* were negatively correlated, explaining how Ω is kept constant through successive nuclear cycles (Fig. S3; Pearson r =-0.5666, P<0.0001).

We next used 3D-Structured Illumination super-resolution Microscopy (3D-SIM) in living embryos to assess the precise location of Plk4 oscillations around the mother centriole. Plk4 is initially recruited to a ring around the mother centriole and then resolves into a single hub that defines the site of daughter centriole assembly [13,14]. In our experiments, Plk4-NG was only very briefly detectable in a ring during late-mitosis; at all other stages it appeared as a single-focus (Fig. S4). Thus, in these embryos, centriolar Plk4-NG levels are largely oscillating during S-phase at the single-focus present at the base of the growing daughter centriole.

To test whether the Plk4 oscillations were important for centriole biogenesis we generated flies co-expressing Plk4-NG (in a *Plk4* mutant background) and Sas-6-mCherry, which is incorporated into the base of the growing daughter centriole and can be used to monitor centriole growth [1]. These flies laid embryos that often failed to hatch (Fig. S5A), but we could simultaneously measure Plk4 oscillations (Fig. S6A) and centriole growth (Fig. S6B) in the embryos that developed normally (Fig. 2A; Movie S2). The centrioles in these embryos were often slightly delayed in initiating growth (Figs. 2A and S5, B and C), allowing us to determine the precise points within the Plk4 oscillation at which daughter centrioles started and stopped growing (Fig. 2A and S6). We found that during each cycle the centriolar levels of Plk4 at which centriole growth was initiated ("start", Fig. 2A) was not significantly different from the centriolar Plk4 levels at which the growth stopped ("stop", Fig. 2A). These data suggest that there is a "threshold" level of centriolar Plk4 at each cycle that is required to support centriole growth: above this threshold the centrioles can grow, below this threshold they cannot. Although this threshold was similar at successive nuclear cycles (Fig. 2, A and B), its absolute level may depend upon the relative concentrations of key centriole biogenesis regulators (see, for example, *Plk4-NG* and *asl* "half-dose" embryos, below).

If the centriolar Plk4 "threshold" concept is correct, then mother centrioles that failed to recruit the threshold level of Plk4 should not be able to grow a daughter. We observed that the centrioles in several of these embryos separated at the start of S-phase, but did not detectably incorporate Sas-6-mCherry, indicating that daughter centrioles did not grow (Fig. S5, B and C).

Importantly, centriolar Plk4 levels still oscillated in these embryos, but the peak amplitude of these oscillations was almost always below the average threshold at which centriole growth was initiated in the other embryos (Fig. S5D). Taken together, these results strongly indicate that the Plk4 oscillations initiate, and then determine the duration of, centriole biogenesis.

We next investigated whether Plk4 oscillations were generated by the core Cdk-Cyclin Oscillator (CCO) that is thought to drive cell cycle progression in most eukaryotic cells. This seemed to be the case, as there was a strong positive correlation between the time at which the Plk4 oscillations peak (oscillation *centre, C*) and the length of S-phase (Fig. S7; Pearson r =0.8668, P<0.0001). Moreover, if we manipulated S-phase length—by decreasing cytoplasmic Cyclin B levels to elongate S-phase [15] (*CycB*$^{1/2}$ embryos), or decreasing cytoplasmic Chk1 (*grapes*) levels to shorten S-phase [16] (*grp*$^{1/2}$ embryos) (Fig. 3, A and B; a total of ~23% difference in S-phase length, denoted with *N*)—the phase of the Plk4 oscillation shifted accordingly (Fig. 3A and B). Thus, the Plk4 oscillator is entrained by the CCO.

There has been some debate, however, about whether the CCO acts as a "ratchet" that triggers the sequential execution of cell cycle events [17,18], or as a "phase-locker" that entrains the phase of several autonomous oscillators to ensure the timely execution of different cellular events [19-21]. In many systems centrioles can continue to duplicate when other aspects of cell cycle progression have been blocked, but it is unclear how they do so [3-5]. To test whether centriolar Plk4 levels could continue to oscillate and drive centriole

biogenesis if the CCO was perturbed, we injected embryos with double-stranded RNAs (dsRNAs) targeting the three embryonic mitotic cyclins: A, B and B3. This arrests embryos in an interphase-like state with intact nuclei that do not duplicate their DNA or divide, but where centrosomes can continue to duplicate [5]. We initially injected embryos in nuclear cycle 7-8 and monitored Plk4-NG behaviour ~30min later. The nuclei in these “late” embryos were arrested in an interphase-like state, but the centrioles continued to duplicate (Movie S3); the timing of these duplication events was more erratic and asynchronous than normal, but a clear Plk4-NG oscillation was associated with each duplication event (Figs. 3C and S8).

We next injected embryos at an earlier stage (nuclear cycles 2-4) and monitored them ~90min later. These “early” embryos contained a small number of nuclei but many more centrioles (Movie S4). Some of these centrioles were “fertile”, and duplicated one or more times in an apparently stochastic fashion (i.e. in a manner that was not synchronised with the other duplicating centrioles), while others were “sterile” and did not duplicate at all (Fig. S9A; Movie S4). We measured Plk4-NG levels at individual centrioles in these embryos. This data was noisy, but fertile centrioles associated with more Plk4-NG than sterile centrioles, and they exhibited clear Plk4-NG oscillations, whereas sterile centrioles did not (Fig. S9, B–D). Moreover, an unbiased computational analysis of all 45 centrioles tracked from 3 different embryos revealed that centriolar Plk4-NG levels could accurately predict whether centrioles were fertile or sterile (Fig. S9, E and F), and that the timing of individual centriolar Plk4-NG oscillations was strongly correlated with

duplication events (Fig. S9, F and G), which were statistically stochastic (Fig. 9H). Together, these results indicate that the CCO normally entrains an autonomous centriolar Plk4 oscillator to synchronize individual centriole duplication events to the frequency of nuclear divisions in the early fly embryo. In the absence of a robust CCO, the Plk4 oscillator can continue to drive centriole duplication events, but in a stochastic manner.

It is well documented that centrioles can continue to duplicate when systems are arrested in an interphase- or S-phase-like states, but a mitotic-state is generally considered to be refractory for centriole duplication [22]. To test whether Plk4 oscillations could continue when embryos were arrested in mitosis, we injected embryos with the microtubule-depolymerising drug colchicine [23] (Movie S5). Plk4-NG oscillations were detectable in these arrested-embryos (Fig. 3D and S10), but their amplitude was dramatically reduced; these oscillations were all sub-threshold for centriole biogenesis (Fig. S11), and we observed no centriole duplication events. Thus, the Plk4 oscillator appears to be calibrated by the CCO so that it can normally execute centriole biogenesis only at the right stage of the cell cycle.

Finally, we injected the protein synthesis inhibitor cycloheximide [24] (Movie S6). This treatment blocked Plk4 oscillations, and we observed no further centriole duplication (Fig. 3E and S12), indicating that the machinery that generates the Plk4 oscillations in these embryos requires active protein synthesis. Taken together, our observations are consistent with a model where the CCO functions to phase-lock autonomous oscillators that are

responsible for different events in the cell cycle [19,20]. We propose that Plk4 forms one such autonomous oscillator that governs centriole biogenesis, and that Plk4 oscillations are induced by a self-sustained enzymatic event on the centriole.

How are Plk4 oscillations generated? Our observation that the Plk4 oscillator is adaptive (i.e., the *A* and *T* of the oscillations are inversely correlated to ensure a constant Ω; Fig. 1C and S3), suggests that centrioles are somehow measuring (i.e. integrating) the total amount of Plk4 bound to them in each nuclear cycle, which remains constant. *Drosophila* Asterless (Asl) recruits Plk4 to centrioles and appears to activate it, allowing Plk4 to phosphorylate itself and Asl at multiple sites [25-27]. Moreover, human Asl (Cep152) also binds, and is phosphorylated by, Plk4 *in vitro* [28,29]. These findings, along with our observation that the *Drosophila* Asl is specifically phosphorylated at centrioles *in vivo* (Fig. S13), led us to propose the following model: At the start of each oscillation cycle, Asl binds Plk4 with high affinity to recruit it to centrioles and activate it (Fig. 4A, step 1; k_1 in Fig. 4B). The active Plk4 then phosphorylates itself [30-32] and Asl [27] at multiple sites, providing a mechanism for each Asl receptor to monitor how much Plk4 activity it has experienced over time (Fig. 4A, step 2; k_2 in Fig. 4B). The active Plk4 also phosphorylates Ana2/STIL to promote centriole growth [10-12]—explaining why a threshold level of centriolar Plk4 is required to promote centriole growth—but this reaction is not important for the generation of Plk4 oscillations *per se*, and so we do not consider it further here. Once Asl is phosphorylated at multiple sites, we hypothesise that it switches to a state that binds Plk4 with low-affinity. The Asl-bound

phosphorylated Plk4 is then released and/or degraded (Fig. 4A, step 3; k_3 in Fig. 4B), leaving behind the unbound, but phosphorylated, Asl-receptor that can no longer recruit Plk4 and so can no longer promote centriole growth.

This model is a regulatory network whereby an inhibitor (Plk4) inhibits its own activator (Asl) [33]. This network maps onto a set of coupled linear ordinary differential equations (see *Mathematical Modelling* section in *Materials and Methods)* (Fig. 4B), which we solved analytically. This model fits the discrete Plk4 oscillation data from each S-phase of nuclear cycles 11-13 well (Fig.4C; R^2=0.998, 0.999 and 0.998, respectively; Table S1 and Figs. S14 and S15), so we tested two predictions suggested by this model.

First, the model predicts that the main difference between the Plk4 oscillations at nuclear cycles 11-13 is the initial rate at which Plk4 binds to Asl (k_1, Fig. 4B and Table S1), which depends on the concentration of cytoplasmic Plk4. This cytoplasmic concentration of Plk4 is predicted to decrease at successive cycles (k_1, Table S1). We therefore tested whether simply decreasing the cytoplasmic concentration of Plk4 would make the *A* and *T* of cycle 12 more like that of cycle 13, while ensuring a constant Ω. We halved the genetic dose of *Plk4-NG* in embryos (hereafter *Plk4-NG*$^{1/2}$ embryos) and found that this was indeed the case, and that our mathematical model fitted the experimental *Plk4-NG*$^{1/2}$ embryo data well (R^2=0.996) (Figs. 4D and S16, A and B; see Table S2 and *Supplementary Text*). Thus, when we perturb the input to the system (cytoplasmic Plk4 levels) and measure the output (total centriole-bound Plk4 over S-phase), the system adapts to changes in the input to

produce the same output. Importantly, we previously showed that centrioles in *Plk4*$^{1/2}$ embryos grow at a slower rate, but for a longer period, and so grow to their normal size [1]. This confirms that the ultimate output of the Plk4 oscillator, i.e., centriole biogenesis, also adapts to changes in the input.

Second, the model predicts that the total amount of the Asl-receptor at the centrioles is the same at each cycle (A_{tot}, Table S1). We confirmed that this was the case (Fig. S17), and used Fluorescence Correlation Spectroscopy (FCS) to show that the cytoplasmic concentration of Asl-GFP—that determines the amount of Asl on the centrioles [34]—also remained constant at the start of each nuclear cycle (Fig. S18). Interestingly, this suggests that Asl may function as an integrator (i.e., a monitoring factor) whose levels are kept constant to allow the oscillation machinery to sense any changes in the input (e.g. Plk4 concentration) and adapt accordingly [35,36]. To test this possibility, we monitored Plk4-NG oscillations in embryos laid by mothers in which we genetically halved the dose of *asl* (hereafter *asl*$^{1/2}$ embryos) (Fig. 4E). This change broke the adaptive nature of the Plk4 oscillator: The *A* was reduced, but *T* hardly changed, and so Ω was reduced (Fig. 4E). Again, the mathematical model fitted the experimental data well (R^2=0.999) (Figs. 4E and S16, C – E; see Table S3 and *Supplementary Text*). If centriole size is kept constant by adapting *A* and *T* to maintain a constant Ω, then the centriole cartwheel should be too small in *asl*$^{1/2}$ embryos (as Ω is now too small), and we confirmed that this was the case (Fig. S19). Thus, the Plk4 oscillator, and so centriole biogenesis, can adapt to lower Plk4 levels, but not to lower Asl

levels—supporting the idea that Asl functions as an integrator in this oscillatory network.

Here we show that Plk4 forms a free-running sub-cellular oscillator that times and executes centriole biogenesis in flies. Importantly, our data mining of a recently published diurnal proteome from mouse liver [37] indicates that Plk4 may also form a free-running oscillator in non-dividing mammalian cells that, like the basic cell cycle oscillator [38,39], can be entrained to the circadian clock (Fig. S20). We speculate that the Plk4 oscillator may exemplify a more general mechanism for regulating organelle biogenesis, whereby autonomous oscillations in the levels/activity of key regulatory factors essential for organelle biogenesis could precisely define the timing and duration of the growth process. Such oscillations are likely to be phase-locked to the oscillators of both the cell cycle and the circadian clock to precisely coordinate organelle biogenesis with other cellular events and processes.

Acknowledgements:

We are grateful to Laura Hankins, Fabio Echegaray, Drs. Marjorie Fournier, Christoffer Lagerholm, Pedro Carvalho and Bela Novak for advice and discussion, the Carvalho Lab (Oxford, UK) for sharing cycloheximide, and Dr. Alain Goriely, Alissa Kleinnijenhuis and the members of our laboratory for critically reading the manuscript. Super-resolution microscopy was performed at the Micron Oxford Advanced Bioimaging Unit, funded by a Strategic Award from the Wellcome Trust (107457). The research was funded by a Wellcome Trust Senior Investigator Award (104575; T.L. Steinacker, M. Mofatteh, A. Wainman, S. Saurya, P.T. Conduit, J.W. Raff), an Edward Penley Abraham Scholarship (to M.G. Aydogan and L. Gartenmann), Ludwig Institute for Cancer Research funding (to F.Y. Zhou), and a Biotechnology and Biological Sciences Research Council grant BB/N016858/1 (to M.A. Boemo).

Author contributions:

This study was conceptualised by M.G.A., M.A.B. and J.W.R. Investigation was done by M.G.A., T.L.S., M.M., L.G., A.W., S.S., P.T.C. and M.B.A. Data were analysed by M.G.A., T.L.S., L.G., F.Y.Z. and M.B.A. Methodology was developed by M.G.A., T.L.S., M.M., F.Y.Z., M.A.B. and J.W.R. Project was administered by M.G.A., M.A.B and J.W.R. Resources were shared/made by M.G.A., M.M., L.G., A.W., S.S. and M.A.B. Software development was carried out by M.G.A., T.L.S., F.Y.Z., and M.A.B. Overall supervision was done by M.G.A. and J.W.R. Validation experiments/analyses were carried out by M.G.A., A.W., S.S. and J.W.R. Finally, M.G.A., M.A.B. and J.W.R. wrote, reviewed and edited the draft.

Competing interests:

Authors declare no competing interests for this study.

Data and materials availability:

All the equations used for mathematical modelling and regressions are available in *Supplementary Materials* and in the following web link: <https://github.com/MBoemo/centriole_oscillator_model.git>. The rest of the data is available upon request.

Figure 1

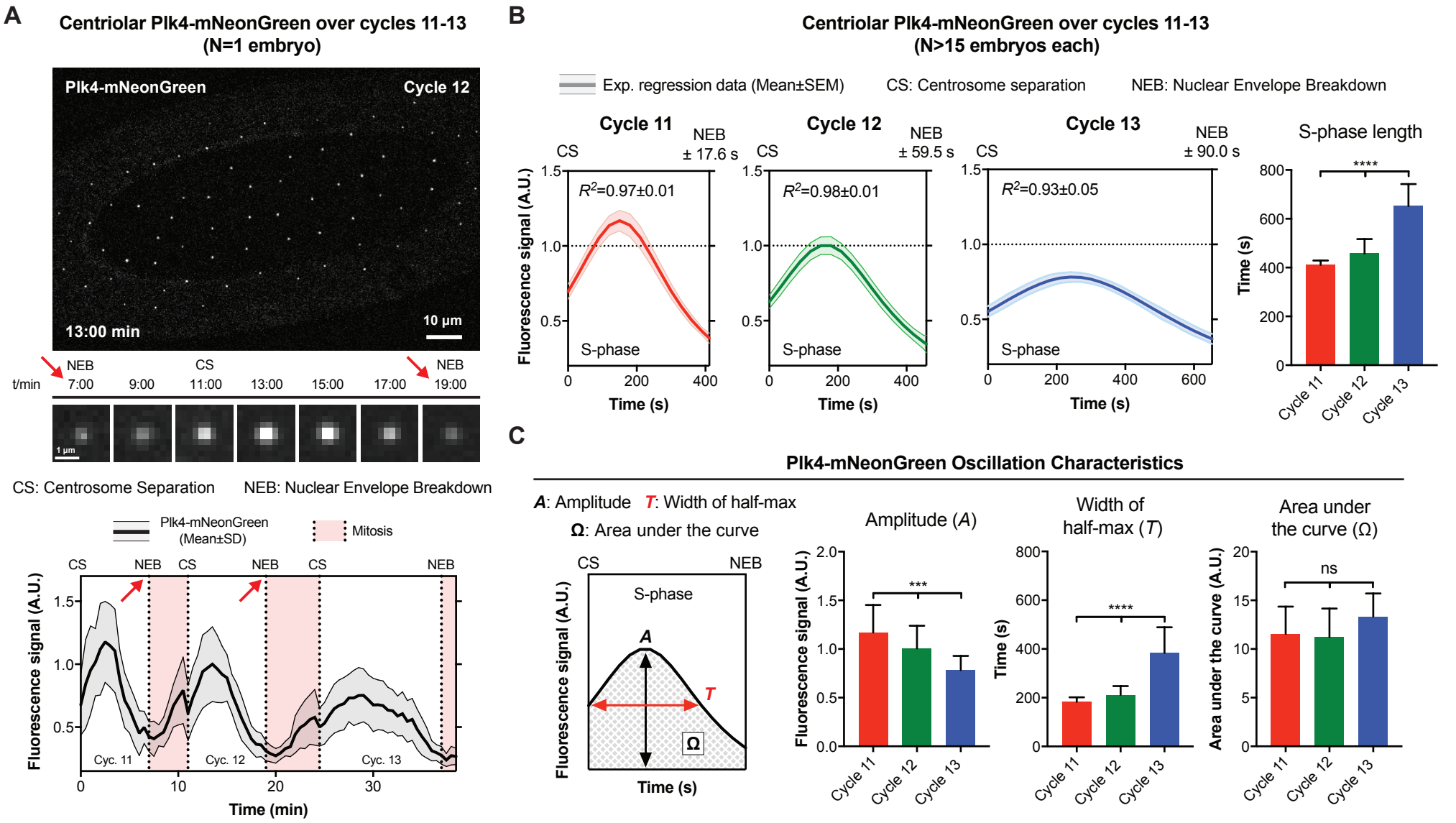
A
Centriolar Plk4-mNeonGreen over cycles 11-13
(N=1 embryo)
Plk4-mNeonGreen
Cycle 12
13:00 min
10 µm
t/min
NEB
CS
NEB
7:00
9:00
11:00
13:00
15:00
17:00
19:00
1 µm
CS: Centrosome Separation
NEB: Nuclear Envelope Breakdown
Plk4-mNeonGreen
(Mean±SD)
Mitosis
CS
NEB
CS
NEB
CS
NEB
Fluorescence signal (A.U.)
Cyc. 11
Cyc. 12
Cyc. 13
Time (min)
B
Centriolar Plk4-mNeonGreen over cycles 11-13
(N>15 embryos each)
Exp. regression data (Mean±SEM)
CS: Centrosome separation
NEB: Nuclear Envelope Breakdown
Cycle 11
Cycle 12
Cycle 13
CS
NEB
± 17.6 s
± 59.5 s
± 90.0 s
R²=0.97±0.01
R²=0.98±0.01
R²=0.93±0.05
S-phase
Fluorescence signal (A.U.)
Time (s)
S-phase length
Time (s)
****
Cycle 11
Cycle 12
Cycle 13
C
Plk4-mNeonGreen Oscillation Characteristics
A: Amplitude
T: Width of half-max
Ω: Area under the curve
CS
NEB
S-phase
A
T
Ω
Fluorescence signal (A.U.)
Time (s)
Amplitude (A)
***
Width of
half-max (T)
****
Area under
the curve (Ω)
ns
Time (s)
Area under the curve (A.U.)
Cycle 11
Cycle 12
Cycle 13

Figure Legends

Figure 1. Plk4 levels at the centriole oscillate.

(A) (Top panel) Micrograph shows an image from a time-lapse movie of an embryo expressing Plk4-NG. (Middle panels) Micrographs illustrate the centriolar Plk4-NG oscillation during nuclear cycle 12—obtained by superimposing all the Plk4-NG foci (n=60) at each timepoint (see *Materials and Methods*). (Bottom panel) Quantification of centriolar Plk4-NG levels during nuclear cycles 11-13 in a single embryo (*red arrows* highlight equivalent timepoints in the middle panels). **(B)** Graphs show the mathematical regression of centriolar Plk4-NG dynamics during S-phase of cycles 11-13 (Regression Mean±SD). Bar chart shows how S-phase length increases at each cycle. R^2 values indicate goodness-of-fit. N≥15 embryos; n=~24, 37, and 53 centrioles (mean) per embryo over cycles 11-13, respectively. **(C)** Cartoon illustrates the oscillation parameters quantified in the bar charts—derived from the data shown in (B). Data are presented as Mean±SD. Statistical significance was assessed using an ordinary one-way ANOVA test (for Gaussian-distributed data) or a Kruskal-Wallis test (***, P<0.001; ****, P<0.0001; ns, not significant).

Figure 2

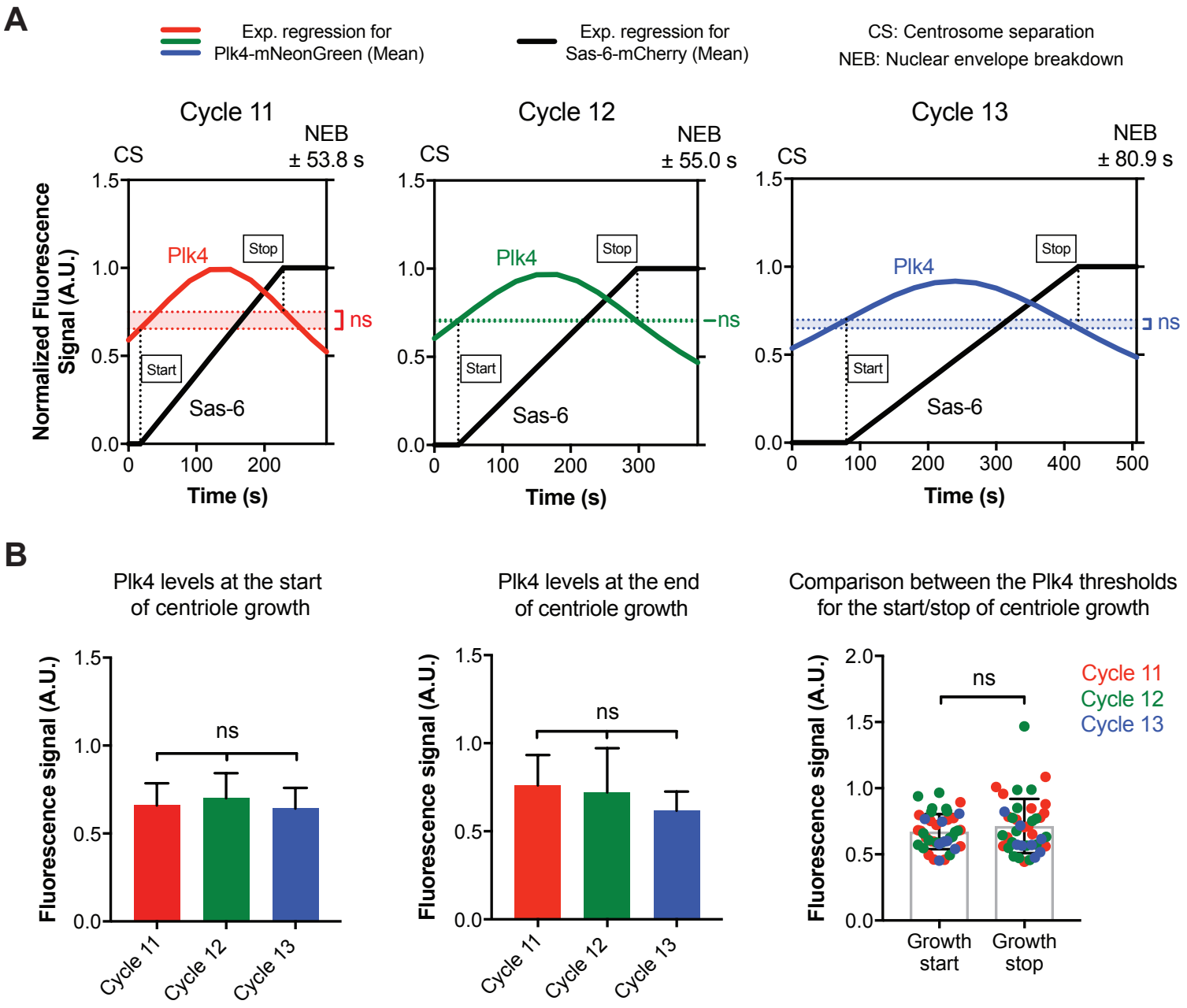
A
Exp. regression for Plk4-mNeonGreen (Mean)
Exp. regression for Sas-6-mCherry (Mean)
CS: Centrosome separation
NEB: Nuclear envelope breakdown
Cycle 11
Cycle 12
Cycle 13
CS
NEB
± 53.8 s
± 55.0 s
± 80.9 s
Normalized Fluorescence Signal (A.U.)
Plk4
Sas-6
Stop
Start
ns
Time (s)
B
Plk4 levels at the start of centriole growth
Plk4 levels at the end of centriole growth
Comparison between the Plk4 thresholds for the start/stop of centriole growth
Fluorescence signal (A.U.)
Cycle 11
Cycle 12
Cycle 13
Growth start
Growth stop

Figure 2. Plk4 oscillations initiate and time centriole biogenesis.

(A) Graphs show the mean regression of Plk4-NG oscillations (*red*, *green* and *blue* lines for cycles 11-13, respectively) and centriole growth (monitored by Sas-6-mCherry incorporation—*black* lines) measured simultaneously in embryos during S-phase of cycles 11-13. For ease of presentation, the standard errors of the mean for these data are not shown here, but are presented in Fig. S6. Dotted lines indicate the centriolar Plk4 levels at which centrioles "start" or "stop" growing; N=17 embryos (cycles 11 and 12), and 8 embryos (cycle 13); n=19, 31, and 45 centrioles (mean) per embryo in cycle 11-13, respectively. See *Materials and Methods* for an explanation of data normalisation and scaling. **(B)** Bar charts quantify the centriolar Plk4-NG threshold levels at which centrioles start and stop growing during cycles 11-13 – derived from the data shown in (A). Data are presented as Mean±SD. For multiple group comparisons, statistical significance was assessed using an ordinary one-way ANOVA test (for Gaussian-distributed data) or a Kruskal-Wallis test. For comparisons between two groups, an unpaired *t* test with Welch's correction (for Gaussian-distributed data) or an unpaired Mann-Whitney test was used (ns, not significant). Embryos in which the centrioles did not grow were excluded from this analysis, but were analysed separately (see Fig. S5, B–D).

Figure 3

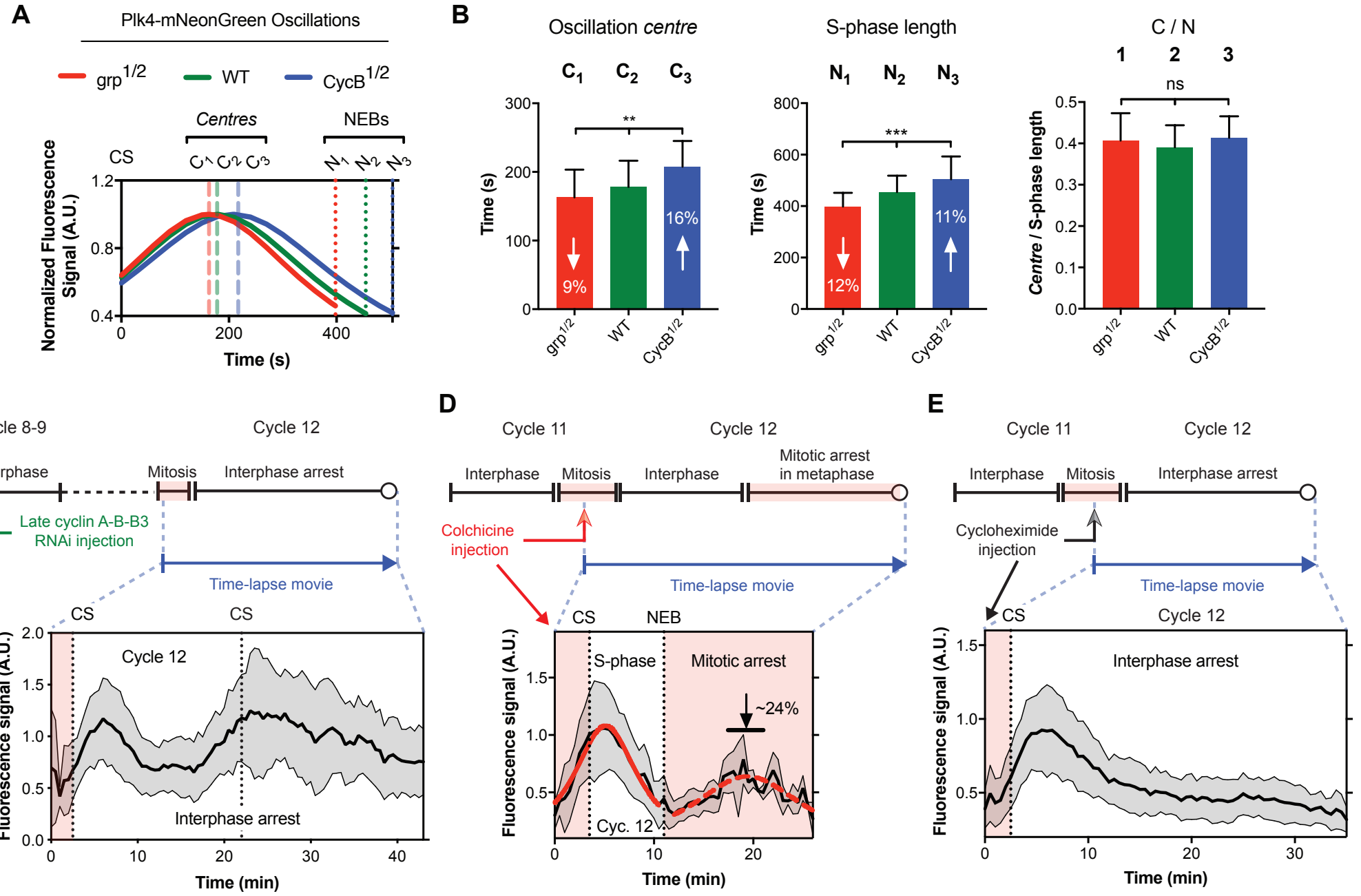
A
Plk4-mNeonGreen Oscillations
grp1/2
WT
CycB1/2
Centres
NEBs
CS
C1 C2 C3
N1 N2 N3
Normalized Fluorescence Signal (A.U.)
Time (s)
B
Oscillation centre
S-phase length
C / N
C1 C2 C3
N1 N2 N3
1 2 3
ns
**
***
Time (s)
Centre / S-phase length
9%
16%
12%
11%
C
Cycle 8-9
Cycle 12
Interphase
Mitosis
Interphase arrest
Late cyclin A-B-B3 RNAi injection
Time-lapse movie
CS
CS
Cycle 12
Interphase arrest
Fluorescence signal (A.U.)
Time (min)
D
Cycle 11
Cycle 12
Interphase
Mitosis
Interphase
Mitotic arrest in metaphase
Colchicine injection
Time-lapse movie
CS
NEB
S-phase
Mitotic arrest
~24%
Cyc. 12
Fluorescence signal (A.U.)
Time (min)
E
Cycle 11
Cycle 12
Interphase
Mitosis
Interphase arrest
Cycloheximide injection
Time-lapse movie
CS
Cycle 12
Interphase arrest
Fluorescence signal (A.U.)
Time (min)

Figure 3. The Plk4 oscillator is free running of, but is entrained and calibrated by, the Cdk-cyclin cell cycle oscillator.

(A) Graph shows the mean regression of nuclear cycle 12 Plk4-NG oscillations in WT (*green*), *CycB*$^{1/2}$ (*blue*) and *grp*$^{1/2}$ (*red*) embryos. *Dashed* lines mark the *centre* (peak) of the Plk4-NG oscillations (denoted with C) and, *dotted* lines indicate the time of NEB (denoted with N) for each genotype. **(B)** Bar charts quantify the time at which the Plk4-NG oscillations peaked, the length of S-phase, and the ratio between them (C/N)—derived from the data shown in (A). N≥14 embryos for each condition; n=55, 43, and 44 centrioles (mean) per embryo in WT, *CycB*$^{1/2}$ and *grp*$^{1/2}$ embryos respectively. To clearly illustrate the phase shift in the oscillations, the highest mean fluorescence signal for each group was normalised to 1. Data are presented as Mean±SD. Statistical significance was assessed using an ordinary one-way ANOVA test (for Gaussian-distributed data) or a Kruskal-Wallis test (**, P<0.01; ***, P<0.001; ns, not significant). **(C – E)** Graphs show the Plk4-NG oscillations in embryos injected with either cyclin A-B-B3 dsRNA, colchicine or cycloheximide (as indicated); the schema above each graph illustrates the experimental protocol. Arrow in (D) indicates the percentage dampening from the expected mean amplitude of Plk4-NG oscillations in cycle 13 (calculated from Fig. 1B). N=6 embryos for C and E, and 10 embryos for D; n=30, 34 and 43 centrioles (mean) per embryo in (C), (D) and (E)**,** respectively. Data are presented as Mean±SD. Regression analysis was performed on colchicine-injected embryos (D)—*solid red line* for the 1st oscillation after drug-injection; *dashed red line* for the 2nd oscillation (see Fig. S10). CS=centrosome separation; NEB=nuclear envelope breakdown.

Figure 4

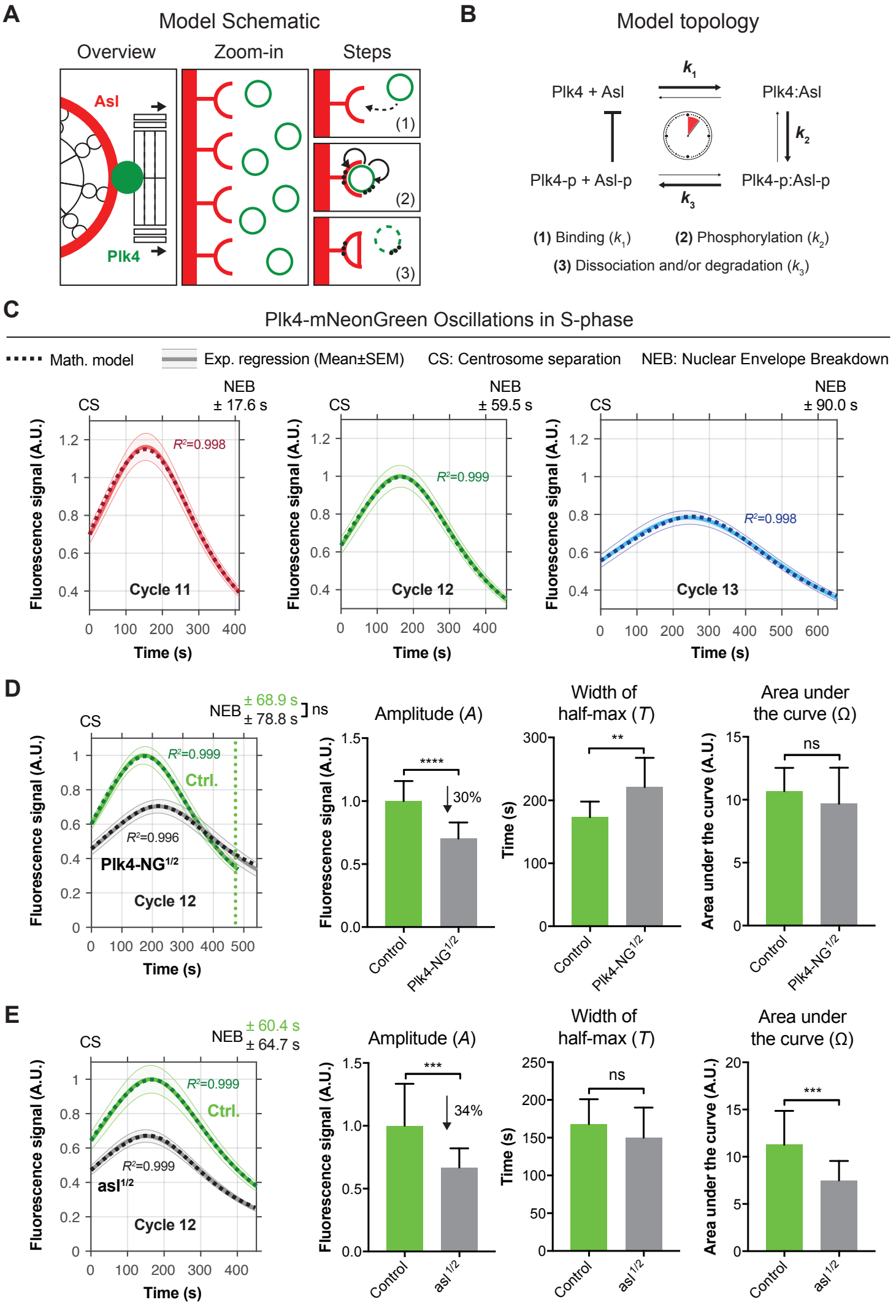

Figure 4. Mathematical modelling and experimental perturbation of the Plk4 oscillations.

(A) Cartoon of the model. The overview illustrates how Asl (*red*) surrounds the mother centriole (*black*, viewed end-on and only partially shown), organising a single focus of Plk4 (*green*) that will promote centriole growth (indicated by arrows) during S-phase. At the start of mitosis, very little Plk4 is bound to Asl (as depicted in the *Zoom-in*). Most Asl receptors are unbound, but they are capable of binding Plk4 with high affinity *(Step 1)* [27]. Once bound, Plk4 is activated, and it starts to phosphorylate itself and Asl at multiple sites (*Step 2*) (indicated by *black* arrows and dots) [25-27]. After several rounds of phosphorylation we speculate that Asl is converted to a state with low affinity for Plk4, so phosphorylated Plk4 is released—and probably degraded [30-32] (*Step 3*). **(B)** Schematic depicts the topology of the mathematical model (see *Materials and Methods* for full details). Asl-p and Plk4-p indicate phosphorylated proteins. Bold arrows indicate the dominant direction of the reactions. The blocked-line indicates that Asl-p effectively inhibits the first reaction, as Asl-p cannot recruit more Plk4. We speculate that a phosphatase removes the phosphate groups from Asl during mitosis to reset the system for the next oscillation (note that this is not incorporated into our model, which discretely models centriolar Plk4-NG levels during S-phase of each cycle). **(C)** Graphs show the regression data of the Plk4-NG oscillations during S-phase of cycles 11-13 (*solid lines*, same data as shown in Fig. 1B) overlaid with mathematical solutions to the model (*dotted lines*). **(D and E)** Graphs show the regression data (*solid lines*) and mathematical solutions to the model (*dotted lines*) for cycle 12 Plk4-NG oscillations, in experiments where either

the genetic dose of *Plk4-NG* was halved (D) (*Plk4-NG*$^{1/2}$), or the genetic dose of *asl* was halved (E) (*asl*$^{1/2}$) (*grey* lines) compared to controls (*green* lines). Note how the amplitude of the Plk4-NG oscillation is decreased when the genetic dosage of either *Plk4-NG* or *asl* is halved, but the period of the oscillation can only "adapt" to keep a relatively constant Ω when Plk4 levels are reduced. As a result, centrioles grow more slowly but for a longer period of time (and so reach the correct size) when Plk4 levels are reduced [1], whereas they grow slowly, but for the normal period of time (and so are too small) when Asl levels are reduced (Fig. S19). Importantly, these observations indicate that the threshold level of centriolar Plk4 required to promote centriole growth can vary depending on the conditions. When the dosage of Asl is reduced, for example, the Plk4 threshold that promotes centriole growth must be lower—as centrioles continue to grow for the same period as controls, even though less Plk4 is present at centrioles at any given timepoint. This is presumably because the ratio of Asl to the other factors promoting centriole growth (such as Plk4, Ana2 and Sas-6) is altered at the site of cartwheel assembly in the "half-dose" embryos. In (D), N≥11 embryos for each condition; n=47 and 42 centrioles (mean) per embryo in *Control* or *Plk4-NG*$^{1/2}$ groups respectively; in (E), N=18 embryos for each condition; n=44 and 43 centrioles (mean) per embryo in *Control* or *asl*$^{1/2}$ groups respectively. Data are presented as Mean±SEM. Bar charts quantify oscillation parameters, as indicated (Data are presented as Mean±SD). Statistical significance was assessed using an unpaired *t* test with Welch's correction (for Gaussian-distributed data) or an unpaired Mann-Whitney test (**, P<0.01; ***, P<0.001;

****, P<0.0001; ns, not significant). R^2 values indicate goodness-of-fit for the mathematical solutions.

References

1. Aydogan, M. G., Wainman, A., Saurya, S., Steinacker, T. L., Caballe, A., Novak, Z. A., Baumbach, J., Muschalik, N. & Raff, J. W. A homeostatic clock sets daughter centriole size in flies. *J Cell Biol* **217,** 1233–1248 (2018).
2. Takao, D., Yamamoto, S. & Kitagawa, D. A theory of centriole duplication based on self-organized spatial pattern formation. *bioRxiv* 424754 (2018). doi:10.1101/424754
3. Gard, D. L., Hafezi, S., Zhang, T. & Doxsey, S. J. Centrosome duplication continues in cycloheximide-treated Xenopus blastulae in the absence of a detectable cell cycle. *J Cell Biol* **110,** 2033–2042 (1990).
4. Sluder, G., Miller, F. J., Cole, R. & Rieder, C. L. Protein synthesis and the cell cycle: centrosome reproduction in sea urchin eggs is not under translational control. *J Cell Biol* **110,** 2025–2032 (1990).
5. McCleland, M. L. & O'Farrell, P. H. RNAi of Mitotic Cyclins in Drosophila Uncouples the Nuclear and Centrosome Cycle. *Curr. Biol* **18,** 245–254 (2008).
6. Claude, A. The constitution of protoplasm. *Science* **97,** 451–456 (1943).
7. Marsh, B. J., Mastronarde, D. N., Buttle, K. F., Howell, K. E. & McIntosh, J. R. Organellar relationships in the Golgi region of the pancreatic beta cell line, HIT-T15, visualized by high resolution electron tomography. *Proceedings of the National Academy of Sciences* **98,** 2399–2406 (2001).
8. Fırat-Karalar, E. N. & Stearns, T. The centriole duplication cycle. *Curr. Biol* **369,** 20130460–20130460 (2014).
9. Foe, V. E. & Alberts, B. M. Studies of nuclear and cytoplasmic behaviour during the five mitotic cycles that precede gastrulation in Drosophila embryogenesis. *J Cell Sci* **61,** 31–70 (1983).
10. Ohta, M., Ashikawa, T., Nozaki, Y., Kozuka-Hata, H., Goto, H., Inagaki, M., Oyama, M. & Kitagawa, D. Direct interaction of Plk4 with STIL ensures formation of a single procentriole per parental centriole. *Nat Commun* **5,** 5267 (2014).
11. Dzhindzhev, N. S., Tzolovsky, G., Lipinszki, Z., Schneider, S., Lattao, R., Fu, J., Debski, J., Dadlez, M. & Glover, D. M. Plk4 phosphorylates Ana2 to trigger Sas6 recruitment and procentriole formation. *Curr. Biol* **24,** 2526–2532 (2014).
12. Kratz, A.-S., Bärenz, F., Richter, K. T. & Hoffmann, I. Plk4-dependent phosphorylation of STIL is required for centriole duplication. *Biology Open* **4,** 370–377 (2015).
13. Arquint, C. & Nigg, E. A. The PLK4-STIL-SAS-6 module at the core of centriole duplication. *Biochem. Soc. Trans.* **44,** 1253–1263 (2016).
14. Banterle, N. & Gönczy, P. Centriole Biogenesis: From Identifying the Characters to Understanding the Plot. *Annu Rev Cell Dev Biol* **33,** 23–49 (2017).
15. Jacobs, H. W., Knoblich, J. A. & Lehner, C. F. Drosophila Cyclin B3 is required for female fertility and is dispensable for mitosis like Cyclin B. *Genes Dev* **12,** 3741–3751 (1998).

16. Sibon, O. C., Stevenson, V. A. & Theurkauf, W. E. DNA-replication checkpoint control at the Drosophila midblastula transition. *Nature* **388,** 93–97 (1997).
17. Nasmyth, K. At the heart of the budding yeast cell cycle. *Trends Genet.* **12,** 405–412 (1996).
18. Stern, B. & Nurse, P. A quantitative model for the cdc2 control of S phase and mitosis in fission yeast. *Trends Genet.* **12,** 345–350 (1996).
19. Orlando, D. A., Lin, C. Y., Bernard, A., Wang, J. Y., Socolar, J. E. S., Iversen, E. S., Hartemink, A. J. & Haase, S. B. Global control of cell-cycle transcription by coupled CDK and network oscillators. *Nature* **453,** 944–947 (2008).
20. Lu, Y. & Cross, F. R. Periodic cyclin-Cdk activity entrains an autonomous Cdc14 release oscillator. *Cell* **141,** 268–279 (2010).
21. Rahi, S. J., Pecani, K., Ondracka, A., Oikonomou, C. & Cross, F. R. The CDK-APC/C Oscillator Predominantly Entrains Periodic Cell-Cycle Transcription. *Cell* **165,** 475–487 (2016).
22. Zitouni, S., Francia, M. E., Leal, F., Gouveia, S. M., Nabais, C., Duarte, P., Gilberto, S., Brito, D., Moyer, T., Kandels-Lewis, S., Ohta, M., Kitagawa, D., Holland, A. J., Karsenti, E., Lorca, T., Lince-Faria, M. & Bettencourt-Dias, M. CDK1 Prevents Unscheduled PLK4-STIL Complex Assembly in Centriole Biogenesis. *Current Biology* **26,** 1127–1137 (2016).
23. Yuan, K. & O'Farrell, P. H. Cyclin B3 is a mitotic cyclin that promotes the metaphase-anaphase transition. *Curr. Biol.* **25,** 811–816 (2015).
24. Edgar, B. A., Kiehle, C. P. & Schubiger, G. Cell cycle control by the nucleo-cytoplasmic ratio in early Drosophila development. *Cell* **44,** 365–372 (1986).
25. Dzhindzhev, N. S., Yu, Q. D., Weiskopf, K., Tzolovsky, G., Cunha-Ferreira, I., Riparbelli, M., Rodrigues-Martins, A., Bettencourt-Dias, M., Callaini, G. & Glover, D. M. Asterless is a scaffold for the onset of centriole assembly. *Nature* **467,** 714–718 (2010).
26. Klebba, J. E., Galletta, B. J., Nye, J., Plevock, K. M., Buster, D. W., Hollingsworth, N. A., Slep, K. C., Rusan, N. M. & Rogers, G. C. Two Polo-like kinase 4 binding domains in Asterless perform distinct roles in regulating kinase stability. *J Cell Biol* **208,** 401–414 (2015).
27. Boese, C. J., Nye, J., Buster, D. W., McLamarrah, T. A., Byrnes, A. E., Slep, K. C., Rusan, N. M. & Rogers, G. C. Asterless is a Polo-like kinase 4 substrate that both activates and inhibits kinase activity depending on its phosphorylation state. *Mol Biol Cell* **29,** 2874–2886 (2018).
28. Cizmecioglu, O., Arnold, M., Bahtz, R., Settele, F., Ehret, L., Haselmann-Weiß, U., Antony, C. & Hoffmann, I. Cep152 acts as a scaffold for recruitment of Plk4 and CPAP to the centrosome. *J Cell Biol* **191,** 731–739 (2010).
29. Hatch, E. M., Kulukian, A., Holland, A. J., Cleveland, D. W. & Stearns, T. Cep152 interacts with Plk4 and is required for centriole duplication. *J Cell Biol* **191,** 721–729 (2010).
30. Holland, A. J., Lan, W., Niessen, S., Hoover, H. & Cleveland, D. W. Polo-like kinase 4 kinase activity limits centrosome overduplication by autoregulating its own stability. *J Cell Biol* **188,** 191–198 (2010).

31. Cunha-Ferreira, I., Bento, I., Pimenta-Marques, A., Jana, S. C., Lince-Faria, M., Duarte, P., Borrego-Pinto, J., Gilberto, S., Amado, T., Brito, D., Rodrigues-Martins, A., Debski, J., Dzhindzhev, N. & Bettencourt-Dias, M. Regulation of Autophosphorylation Controls PLK4 Self-Destruction and Centriole Number. *Current Biology* **23,** 2245–2254 (2013).
32. Klebba, J. E., Buster, D. W., Nguyen, A. L., Swatkoski, S., Gucek, M., Rusan, N. M. & Rogers, G. C. Polo-like Kinase 4 Autodestructs by Generating Its Slimb-Binding Phosphodegron. *Current Biology* **23,** 2255–2261 (2013).
33. Novák, B. & Tyson, J. J. Design principles of biochemical oscillators. *Nat Rev Mol Cell Biol* **9,** 981–991 (2008).
34. Novak, Z. A., Conduit, P. T., Wainman, A. & Raff, J. W. Asterless licenses daughter centrioles to duplicate for the first time in Drosophila embryos. *Curr. Biol.* **24,** 1276–1282 (2014).
35. Somvanshi, P. R., Patel, A. K., Bhartiya, S. & Venkatesh, K. V. Implementation of integral feedback control in biological systems. *Wiley Interdiscip Rev Syst Biol Med* **7,** 301–316 (2015).
36. Ferrell, J. E. Perfect and Near-Perfect Adaptation in Cell Signaling. *Cell Syst* **2,** 62–67 (2016).
37. Wang, Y., Song, L., Liu, M., Ge, R., Zhou, Q., Liu, W., Li, R., Qie, J., Zhen, B., Wang, Y., He, F., Qin, J. & Ding, C. A proteomics landscape of circadian clock in mouse liver. *Nat Commun* **9,** 1553 (2018).
38. Matsuo, T., Yamaguchi, S., Mitsui, S., Emi, A., Shimoda, F. & Okamura, H. Control mechanism of the circadian clock for timing of cell division in vivo. *Science* **302,** 255–259 (2003).
39. Yang, Q., Pando, B. F., Dong, G., Golden, S. S. & van Oudenaarden, A. Circadian gating of the cell cycle revealed in single cyanobacterial cells. *Science* **327,** 1522–1526 (2010).

Supplementary Materials

Materials and Methods

D. melanogaster stocks and husbandry

The specific *D. melanogaster* stocks used in this study are listed in Table S4, and the lines generated and tested here are listed in Table S5. To generate Plk4-mNeonGreen and Asl-mKate2 constructs: **1)** NheI restriction enzyme sites were introduced into an mCherry C-terminal Gateway vector [1], using the Quikchange II XL mutagenesis kit (Agilent Technologies). **2)** The mCherry tag was replaced with either mNeonGreen [2] (Allele Biotechnology) or mKate2 [3] tags by homologous recombination via In-fusion Cloning (TaKaRa). **3)** NheI restriction enzyme sites were removed via site-directed mutagenesis, using the Quikchange II XL mutagenesis kit (Agilent Technologies). These vectors were recombined via Gateway technology to pDONR-Zeo vectors (Thermo Fisher Scientific) where the genetic regions of either *Plk4* [4] or *asl* [5] were previously cloned from 2 kb upstream of the start codon up to (but excluding) the stop codon. Primer sequences are listed in Table S6. Transgenic lines were generated using standard P-element mediated transformation by the Fly Facility in the Department of Genetics, University of Cambridge (Cambridge, England, UK). Flies were maintained at 18°C or 25°C on *Drosophila* culture medium (0.77% agar, 6.9% maize, 0.8% soya, 1.4% yeast, 6.9% malt, 1.9% molasses, 0.5% propionic acid, 0.03% ortho-phosphoric acid, and 0.3% nipagin) in vials or bottles.

Hatching experiments

To measure embryo hatching rates, 0-3 h embryos were collected and aged for 24 h, and the % of embryos that hatched out of their chorion was calculated. At least 4 technical repeats were carried out over several days, and a total of at least 400 embryos were analysed.

Embryo collections and drug injections

For embryo collections, 25% cranberry-raspberry juice plates (2% sucrose and 1.8% agar with a drop of yeast suspension) were used. Embryos for imaging experiments were collected for 1h at 25°C, and aged at 25°C for ~45–60 min. Embryos were dechorionated by hand, mounted on a strip of glue on a 35-mm glass-bottom Petri dish with 14 mm micro-well (MatTek), and were left to desiccate for 1 min at 25°C. After desiccation, the embryos were covered with Voltalef grade H10S oil (Arkema). Embryos for drug injection experiments were treated in the same way except that the desiccation period was increased to 5-6 min. Colchicine in Schneider's insect medium was injected at a needle concentration of 100 µg/ml (diluted from a 20 mg/ml stock in water) [6]. Cycloheximide in Schneider's insect medium was injected at a needle concentration of 4 µg/ml (diluted from a 10 mg/ml stock in DMSO) [7].

Synthesis and injection of double-stranded RNA

Double-stranded RNAs (dsRNAs) were synthesised essentially as described previously [8]. Primer sequences used for gene amplification are listed in Table S6. The linker sequence 5'-GGGCGGGT-3' was added to the 5' end of each primer to facilitate the addition of the T7 promoter in the second round of PCR using a universal primer containing the linker (5'-TAATACGACTCACTATAGG GAGACCACGGGCGGGT-3'). The resulting RNA was precipitated with 8 µl of 3M Na-Acetate and 220 µl of 100% ethanol before washing with 70% cold ethanol. The RNA pellets were air dried and resuspended in 30 µl of RNase-free diethylpyrocarbonate-treated water (Thermo Fisher Scientific). To generate double-stranded molecules, RNAs were placed in a 67.5°C water bath for 30 min, and allowed to cool to room temperature over 90 min. Unincorporated UTPs were removed using CHROMA SPIN-100-DEPC-H_2O columns (Clontech) according to the manufacturer's instructions. To confirm the synthesis of the correct RNA product, 3 µl of the final reaction was subjected to electrophoresis on a 1.5% agarose gel using 2xRNA loading buffer (Thermo Fisher Scientific). A 1:1 mix of RNA and loading buffer was heated to 65°C for 5 min and then placed on ice to denature any secondary structure of RNA. Double-stranded RNA was injected at a concentration of approximately 0.6–0.8 mg/ml.

Centriole purification

Whole centrosomes, comprising centrioles with associated pericentriolar material (PCM), were isolated from extracts of 0-4 h old *Drosophila* embryos, using a modified version of an established centrosome isolation protocol [9]. Centrosomal and cytosolic fractions were purified on a sucrose step-gradient, as described previously [10]. Phosphatase treatment was performed by incubating the centriole fractions with alkaline phosphatase (Roche) for 4.5 hr at 37°C with or without phosphatase inhibitor cocktails 2 and 3 (Sigma).

Immunoblotting

Immunoblotting was performed as described previously [4]. Primary antibodies used in this study are as follows: rabbit anti-Asl [11], rabbit anti-γ-tubulin [12], mouse anti-GFP (Roche) and mouse anti-Actin (Sigma); all antibodies were used at 1:500 dilution in blocking solution [4]. For all blots, 10 or 30 staged early embryos were boiled in sample buffer and loaded in each lane. The incubation period for primary antibodies was 1 h. Membranes were quickly washed 3x in TBST (TBS and 0.1% Tween 20) and then incubated with HRPO-linked anti-mouse IgG (both GE Healthcare) diluted 1:3,000 in blocking solution for 45 min. Membranes were washed 3x15min in TBST and then incubated in SuperSignal West Femto Maximum Sensitivity Substrate (Thermo Fisher Scientific). Membranes were exposed to film using exposure times that ranged from <1 to 30s.

Image acquisition, processing, and analysis

Spinning disk confocal microscopy

Living embryos were imaged at room temperature using a system equipped with an EM-CCD Andor iXon+ camera on a Nikon Eclipse TE200-E microscope using a Plan-Apochromat 60×/1.42-NA oil DIC lens, controlled with Andor IQ2 software. Confocal sections of 17 slices at 0.5µm intervals were collected every 30 s. A 488nm laser was used to excite mNeonGreen and GFP, and a 568nm laser was used to excite mCherry and mKate2. Emission discrimination filters were applied when mNeonGreen and mCherry were imaged together.

Post-acquisition image processing was performed using Fiji (National Institutes of Health). Maximum-intensity projections of the images were first bleach-corrected with Fiji's *exponential fit* algorithm, and background was subtracted using the *subtract background* tool with a rolling ball radius of 10 pixels. Plk4-NG, Sas-6-mCherry or -GFP, and Asl-mCherry or -GFP were tracked using the Fiji plug-in TrackMate [13] with a track spot diameter size of 1.1 µm. The regressions for the centriole growth curves (Sas-6-GFP or -mCherry) were calculated in Prism 7 (GraphPad Software), as described previously [4]. The regressions for the Plk4 oscillation curves (Plk4-NG) were calculated using the *nonlinear regression* (curve fit) function in Prism 7. Discrete Plk4 oscillation curves in S-phase were initially fitted against four different functions to assess the most suitable regression model: 1) Lorentzian, 2) Gaussian, 3) Increase – Constant – Decrease, and 4) Increase – Decrease. Among these models, Lorentzian best fit the data (Fig. S1D). Thus, all the discrete Plk4 oscillation curves in S-phase were regressed using the Lorentzian function. The Lorentzian and Gaussian functions are described in Prism 7, while the latter two functions are in-house algorithms [14]. In order to plot the dynamics of Plk4-NG and Sas-6-mCherry together (see Fig. 2), the highest mean fluorescence signal for each tag was normalized to 1 and was accordingly scaled across cycles 11-13 (scaling factor for Plk4-NG was taken from Fig. 1, B and C).

In all the imaging experiments, the beginning of S-phase was taken as the time at which the old and new mother centrioles were first detected to separate from each other (termed "centrosome separation" or "CS"). Entry into mitosis was taken as the time of nuclear envelope breakdown (NEB), which could be determined in our movies by adjusting the contrast to visualise when the cytoplasmic pool of the fluorescent protein was first observed to enter into the nucleus.

Analysis of centriole "fertility" in "early" embryos injected with cyclin A-B-B3 dsRNA

In experiments where we depleted "early" embryos of mitotic cyclins, we observed qualitatively that "fertile" centrioles exhibited distinct Plk4-NG fluorescence peaks that appeared to approximately correlate with centriole

duplication events, while "sterile" centrioles, which did not duplicate during the imaging period, exhibited no obvious peaks (Fig. S9B). To test if we could more quantitatively distinguish between fertile and sterile centrioles, we analysed all 45 centrioles that we could track throughout the observation period in 3 different embryos. We first assessed the average signal-to-noise ratio (SNR) of each centriole over the entire observation period and found that fertile centrioles exhibited a significantly higher SNR than sterile centrioles—assessed using a *t*-test assuming equal variance (Fig. S9C). The distribution of SNR within sterile and fertile centriole signals was unimodal and symmetrically distributed (Fig. S9D), so we attempted to classify centrioles in an unbiased way by thresholding the SNR. Based on the bimodality of the SNR, an automatic threshold was determined from the data using Otsu thresholding (*red* dashed line; Fig. S9D); the classification performance was summarized in a visual confusion matrix, which shows the proportion of correctly and falsely classified signals (Fig. S9E). This unbiased computational method successfully classified ~74% of the fertile centrioles and ~71% of the sterile centrioles.

We next tested whether computationally identified peaks in the Plk4-NG signal were correlated with centriole duplication events. Peaks or local maxima in the Plk4-NG fluorescence signals were initially detected as points whose two direct neighbouring points have lower amplitude. This was implemented using Scipy's [15] *find_peaks* function with parameters, height=0, distance=1, prominence=0.1 (minimum). Direct application to the raw signal identified too many false positives, so the raw signal was first processed using an asymmetric least squares filter [16] with parameters, $\lambda=10^2$, p=0.1 run for 5 iterations—see Fig. S9B for examples of how the raw peak data (*black*) is converted to filtered peak data (*red*) by this process. To determine whether the filtered Plk4-NG peaks were predictive of centriole duplication, we determined all the peaks for the fertile centriole signals and assessed whether these peaks could be used to "retrieve" the real or relevant time points for centriole duplication. The performance of such retrieval can be evaluated using "precision" (the number of relevant retrievals amongst all retrieved instances—in this case the number of Plk4 peaks associated with a centriole duplication event divided by the total number of Plk4 peaks) and "recall" (the number of relevant instances retrieved of the total relevant instances—in this case the number of Plk4 peaks associated with a centriole duplication event divided by the total number of centriole duplication events), as defined below.

$$Precision = \frac{Number\ of\ (Relevant\ \&\ Retrieved)}{Number\ of\ (Retrieved)},$$

$$Recall = \frac{Number\ of\ (Relevant\ \&\ Retrieved)}{Number\ of\ (Relevant)}$$

The evaluation of such a system naturally depends on the cut-off to call a positive match between the Plk4-NG signal peak and its corresponding centriole duplication time. Too small a cut-off (e.g. 0 minutes) is unrealistic: no system can predict time perfectly; while too large a cut-off (e.g. 15 min) is too lenient and non-specific. Fig. S9F (graph on the left) plots the precision

evaluated over all centrioles for different temporal cut-offs attempting to uniquely match Plk4-NG peaks to the nearest duplication time. The elbow point (*red* dashed line) was selected at 5 min as an appropriate cut-off with a precision of ~80% (Note that the recall is not plotted in this graph). It was almost the same precision as *Number of (Relevant)* = 52, *Number of (Retrieved)* = 49, as visualized by a Venn diagram (Fig. S9F; mid panel). The temporal cut-off can also be interpreted as an estimate of the temporal accuracy to which Plk4-NG peak time associates with centriole duplication time. In addition, the impact of peak strength (as measured by peak prominence) on the retrieval performance was assessed by evaluating the ranked retrieval performance from the precision-recall curve (given a cut-off of 5 min). The resultant average precision (AP) was 63.1% (Fig. S9; graph on the right). The drop in performance suggested a dependence on Plk4-NG peak fluorescence intensity. Finally, the correlation between the Plk4-NG peaks and times of centriole duplication was examined (Fig. S9G), which provided an alternative accuracy test. Plk4-NG peaks were uniquely matched to the nearest centriole division times without using a temporal cut-off over individual centrioles from three independent embryos. Pearson correlation r, r-squared R^2 and *P* values are reported as goodness of fit. The fitted regression line, $y = 0.87x + 3.69$. Together, these unbiased computational analyses indicate that the Plk4 oscillations at individual centrioles are highly correlated with the time at which these centrioles duplicate.

Stochasticity of centriole duplication in the asynchronous cytoplasm

Given the ability of Plk4-NG peaks to predict centriole duplication, Plk4-NG peak times were used to assess the stochasticity of centriole duplication in the asynchronous “early” embryos depleted of mitotic cyclins versus un-injected control “synchronous” embryos (taken from Fig. S2). Fig. S9H plots the individual peak occurrences over the same 0-48 min interval with a density estimate using Gaussian kernel density. Compared to synchronous duplications, Plk4-NG peak events (from asynchronous duplications) were much more uniformly distributed over the same time interval. This was statistically tested by determining whether the density of Plk4-NG peak events, X from asynchronous duplications could be described with an equivalent uniform distribution, *U* with a mean of 24 min. The following hypothesis test was mathematically constructed with null H_0 and test H_1 hypotheses:

$$H_0: X \sim U(24\ \text{min})$$
$$H_1: X \nsim U(24\ \text{min})$$

Non-parametric Kolmogorov–Smirnov test was used to implement the test at 5% significance. The asynchronous Plk4-NG peak events cannot be distinguished from uniform sampling, whereas synchronous Plk4-NG peak events are significantly different (Fig. S9H).

3D-Structured Illumination Microscopy (3D-SIM)

Living embryos were imaged at room temperature using a DeltaVision OMX V3 Blaze microscope (GE Healthcare). The system was equipped with a 60×/1.42-NA oil UPlanSApo objective (Olympus Corp.), 488nm and 593nm diode lasers, and Edge 5.5 sCMOS cameras (PCO). Spherical aberration was reduced by matching the refractive index of the immersion oil (1.514) to that of the embryos. 3D-SIM image stacks consisting of six slices at 0.125μm intervals were acquired in five phases and from three angles per slice. The raw acquisition was reconstructed using softWoRx 6.1 (GE Healthcare) with a Wiener filter setting of 0.006 and channel-specific optical transfer functions (OTFs). Filters used for the green and red channels were a 540/80 centre band pass filter and a 605-long pass filter, respectively. For two-color 3D-SIM, images from green and red channels were registered with the alignment coordination information obtained from the calibrations using 0.2μm-diameter TetraSpeck beads (Thermo Fisher Scientific) in the OMX Editor software. The SIMCheck plug-in in ImageJ (National Institutes of Health) was used to assess the quality of the SIM reconstructions [17]; only images that passed this test were used.

Mathematical modelling

Fig. 4, A and B, specifies a regulatory network wherein Plk4 binds to an Asl receptor with high affinity; this activates Plk4, allowing it to phosphorylate itself and Asl multiple times. After a certain number of phosphorylations, Asl switches to a new state that binds Plk4 with low affinity. As a result, Plk4 unbinds, leaving Asl in a phosphorylated, low affinity state. In our model (which only attempts to discretely model the Plk4 oscillation through a single cycle of S-phase), Asl is not dephosphorylated after Plk4 dissociates. We suspect that, in reality, Asl is normally dephosphorylated in early mitosis, which "resets" it to a high-affinity state in preparation for the next oscillation. Thus, during each oscillation, centriolar Asl is gradually converted to a low affinity binding state; this forms a time-delayed negative feedback loop, as Asl effectively activates Plk4 to gradually promote its own inhibition via multiple rounds of phosphorylation. After making assumptions about the chemical kinetics of the system and imposing suitable initial conditions, the behavior of this regulatory network can be simulated by mapping it onto a set of coupled ordinary differential equations (see below).

In the model, it is assumed that Plk4 is well-mixed in the cytoplasm, and that centrioles are sufficiently large macromolecular structures, allowing Plk4 and Asl receptors on the centriole to follow mass-action kinetics. $[\boldsymbol{P}]$ and $[\boldsymbol{A}]$ denote the concentrations of unbound cytoplasmic Plk4 and unbound centriolar Asl, respectively. Plk4 binds to Asl with the fixed rate constant $\boldsymbol{k}$, and the rate constant of the reverse reaction is sufficiently small that any unbinding is ignored. Once Plk4 is bound to Asl, it can only unbind once it has phosphorylated Asl nine times (see below for an explanation of why this number was chosen). $[\boldsymbol{A_0}]$ denotes the concentration of Asl receptor that has bound Plk4, but has not yet been phosphorylated, while $[\boldsymbol{A_i}]$ denotes the

concentration of Asl receptors that have been phosphorylated *i* times. Each phosphorylation of Asl by Asl-bound Plk4 has rate constant $\boldsymbol{k_2}$ and, following nine phosphorylations, the Asl is switched to a state that binds Plk4 with very low affinity $[\boldsymbol{A_9}]$. Once Asl has been converted to this low affinity state, Plk4 unbinds at rate $\boldsymbol{k_3}$. The rate constant of the reaction where Plk4 binds to Asl receptor in this low affinity state is assumed to be sufficiently small that this reaction is ignored in the model.

Intuitively, k scales the affinity with which Plk4 binds to an Asl receptor. By mass action kinetics, the rate of this reaction is given by $k * [P] * [A]$. It is assumed in the model that Plk4 is abundant enough in the cytoplasm that its concentration does not decrease over the few minutes of the single S-phase cycle; this assumption means that $[P]$ is constant. Therefore, the number of parameters in the model is reduced by introducing the new rate constant $\boldsymbol{k_1 = k * [P]}$.

Using the assumptions above, the regulatory network in Fig. 4, A and B, is simulated using the following set of ordinary differential equations which are solved over the time domain 0 ≤ t ≤ S, where S is the length of S-phase:

$$\frac{d[A_0]}{dt} = k_1[A] - k_2[A_0] \tag{1}$$

$$\frac{d[A_1]}{dt} = k_2[A_0] - k_2[A_1] \tag{2}$$

$$\vdots$$

$$\frac{d[A_9]}{dt} = k_2[A_8] - k_3[A_9] \tag{3}$$

$$\frac{d[A]}{dt} = -k_1[A] \tag{4}$$

Appropriate initial conditions at t = 0 are,

$$[A_0] = \hat{A}_0; \;\; [A] = \hat{A}; \;\; [A_1] = [A_2] = \cdots = [A_9] = 0. \tag{5}$$

In equation (5), the positive constant $\boldsymbol{\hat{A}_0}$ is the initial amount of Plk4-bound Asl at the centriole at the start of each S-phase, which is determined experimentally for each cell cycle using the techniques described in the *Image acquisition, processing and analysis* section of the *Materials and Methods* and also in the *Supplementary Text* (Fig. 4, C–E). The constant $\boldsymbol{\hat{A}}$ is the initial amount of unbound Asl, so the total amount of Asl in the system is given by $A_{tot} = \hat{A}_0 + \hat{A}$.

The model specified by equations (1)–(5) has an analytical solution, which is solved using MATLAB's *dsolve*. Values for the parameters $\hat{A}$, k_1, k_2, and k_3 were determined by fitting the curve $[A_0](t) + [A_1](t) + \cdots + [A_9](t)$ to the experimentally measured data for the amount of Asl-bound Plk4 (i.e., the Plk4 that is recruited to the centriole) over time. Fitting was done using a *trust-region* algorithm to optimise a nonlinear least squares penalty function.

The fitting was constrained so that all parameters were positive, and k_1, k_2, and k_3 were between 0 and 1. Parameter values are shown in Tables S1–S3. As explained below, the solutions to this model are very insensitive to variations in k_3 (see Fig. S15), so in the solutions presented here k_3 was kept at a constant value of 0.06906, which was the best-fit parameter value for cycle 12 (Tables S1–S3).

In the model, we assumed that Asl had to be phosphorylated by Plk4 nine times before it switched to a low-affinity state—indicated by variables $[A_0], \cdots, [A_9]$. We chose this number because we tested the effect of the number of phosphorylation sites on the model solution. The best fit curves for $[A_0](t) + [A_1](t) + \cdots + [A_N](t)$ for N = 1, 4, 9, 14, or 16 suggested that the model fits the data slightly better when setting N=9 (R^2=0.9996) as opposed to N=1 (R^2=0.9152), N=4 (R^2=0.9886), N=14 (R^2=0.9962) or N=16 (R^2=0.9931), so we used 9 phosphorylation sites in all subsequent modelling. Interestingly, however, the curves for N=4, 9 or 14 were all within the standard error of the mean (Fig. S14), indicating that the model is relatively insensitive to the choice of the number of phosphorylation sites within this range.

Table S1 shows that the *trust-region* algorithm finds a good fit (R^2>0.99) for the model to the experimental data (Figs. 1B and 4C; cycles 11-13), but this provides little information about uniqueness of the fit: There may be other subsets of the parameter space that also provide a good fit to the data. To see if any such regions could be detected, the parameter space was further explored by using a *Metropolis-Hastings Markov chain Monte Carlo* algorithm. Four Markov chains were started at the positions in the parameter space specified in Table S7. Fig. S15A shows the six two-dimensional traces of the four-dimensional parameter space. For clarity, only points that provided a good fit to the cycle 12 data (R^2>0.95; Figs. 1B and 4C) are shown (Fig. S15A).

The results in Fig. S15, A and B, show how sensitive the model is to changes in each parameter value. Parameter k_3 is very insensitive, so we set it to a constant arbitrary value of 0.06906 to allow a more intuitive comparison of the other variables in Table S1–S3. In contrast, the model only fit the data well for a relatively narrow range of values for k_1, k_2, and $\hat{A}$. The Monte Carlo results also reveal correlations between k_1 and k_2, k_1 and $\hat{A}$, and k_2 and $\hat{A}$. For example, these results show that if $\hat{A}$ (the initial amount of unbound Asl receptor at the start of S-phase) is reduced, the model can still fit the data well if k_2 is decreased and k_1 is increased. While these results suggest that there is a single, continuous region of the parameter space that provides a good fit to the data, it is still possible that there are other such regions that the Markov chains in Fig. S15 did not explore. However, the results (in Fig. S15B) show

that the points, which are identified at the center of the parameter region, provide the best fit to the data. This suggests the nonlinear least squares minima found by the *trust-region* fitting is unlikely to be very sensitive to the initial seed that was chosen.

See *Supplementary Text* for more information about how this model was used to probe the effect of reducing the concentration of Plk4 and Asl, shown in Tables S2 and S3.

Fluorescence Correlation Spectroscopy (FCS)

FCS setup and measurements

Point FCS measurements were performed on a confocal Zeiss LSM 880 (Argon laser excitation at 488 nm and GaASP detector) with the Zen Black Software. A C-Apochromat 40x/1.2 W objective and a pinhole setting of 1AU were used. A laser power of 10 μW was used, and no photobleaching was observed during the measurements.

The effective volume of the imaging setup was estimated to be 0.28 fL by three independent methods as described previously [18]. These included: **1)** Measuring the concentration of soluble Alexa Fluor™ 488 NHS Ester dilution series (100 nM, 10 nM, 1 nM and 0.1 nM). **2)** Measuring the diffusion time for Alexa Fluor™ 488 NHS Ester (same concentrations) in water at 25 °C. The measured diffusion time was then compared to a previously reported diffusion coefficient for the Alexa Fluor™ 488 NHS Ester [19]. **3)** Imaging subresolution beads (FluoSpheres™ Carboxylate-Modified Microspheres, 0.1 µm) and determining the effective volume via Gaussian fitting with the *line tool* and *Z-axis profile* in ImageJ (Bethasda, USA).

Embryo collections (from mother flies expressing Asl-GFP under the control of its own promoter in an *asl* mutant background) were done as described in *Embryo collections and drug injections* section above, with the exception of using high precision 35 mm, high Glass Bottom µ-dishes (ibidi). Before every measurement, spherical aberrations were adjusted on the correction collar of the objective, based on the count-rate per molecule (CPM). At the beginning of S-phase in each cell cycle (when the old and new mother centrioles were separating), consecutive cytoplasmic measurements were made 6x for 10 sec (each) at the centriolar plane of the embryo. The individual recordings where centrioles were moving through the measurement spot were immediately discarded, given the erratic shape of their correlation curve. The microscope was kept precisely at 25 °C throughout the measurements.

Autocorrelation analysis and post-acquisition curve fitting

The autocorrelation function, $G(\tau)$, was calculated during each measurement in the Zen Black software using the following equation:

$$G(\tau) = \frac{\langle \delta I(t) \cdot \delta I(t+\tau) \rangle}{\langle \delta I(t) \rangle^2}$$

where $\langle\ \rangle$ denotes a time average, $\delta I(t)$ describes the intensity fluctuation at the time point *t*, and τ states the lag time of the autocorrelation.

All 10 sec-recordings were then fitted with 8 different 3D diffusion models using the software FoCuS-Point [20] with the following equation:

$$G_{3D}(\tau) = \sum_{k=1}^{D_S} A_k \left(1 + \left(\frac{\tau}{\tau_{xyk}}\right)^{\alpha^k}\right)^{-1} \left(1 + \left(\frac{\tau}{AR^2\tau_{xyk}}\right)\right)^{-1/2}$$

where A_k is inversely proportional to the average number of particles in the effective volume V_{eff}, τ_{xy} describes the average residence time of the diffusing species in V_{eff}, α accounts for anomalous subdiffusion within the cytoplasm, and *AR* is a structural parameter that describes the relationship among the x, y and z-axes of the excitation volume.

Dark states of the fluorophore were fitted with the following formula:

$$G_T(\tau) = 1 + \sum_{j=1}^{T_s} \frac{T_j}{1 - T_j} \cdot e^{-\tau/\tau_{Tj}}$$

where *T* depicts the triplet population, and τ_T states the triplet correlation time during which the fluorophore stays in the dark state [21].

The data was fitted within the boundaries of 4×10^{-4} ms and 1.5×10^{3} ms, and the dark states were restricted to 10-300 μs for the blinking, and 1-10 μs for the triplet state. The models (**Ms**) were defined as the following: **M1)** 1 diffusing species (ds) 0 blinking states (bs) 0 triplet states (ts); **M2)** 1ds 1bs 0ts; **M3)** 1ds 0bs 1ts; **M4)** 1ds 1bs 1ts; **M5)** 2ds 0bs 0ts; **M6)** 2ds 1bs 0ts; **M7)** 2ds 0bs 1ts; **M8)** 2ds 1bs 1ts. In all models, the structural parameter *AR* and the anomalous subdiffusion parameter α were kept constant at 5 and 0.7, respectively.

In order to avoid over-fitting the data, the most plausible model to describe the autocorrelation functions was selected using the Bayesian Information Criterion (BIC), which is based on the likelihood function, but introduces a penalty term for the complexity (number of variables) for the models [22]. In this study, **M4** was the preferred model (see Fig. S18A$_{(iv)}$) to describe Asl-GFP diffusion.

In some measurements a sudden drop in CPM was observed, possibly due to movements within the embryo or drifting away from the measurement plane. When the sudden drop in CPM happened, a strong, unreasonable increase in concentration was observed. Therefore, recordings with an average CPM of

less than 5000 were discarded (the *red dotted* restriction threshold in Fig. S18A$_{(v)}$). Only the embryos with 4-6 recordings (after thresholding) were included in the final analysis, and the concentration was calculated from the FoCuS-point fit data of the preferred model:

$$\langle N \rangle = \frac{1}{G_0}\,, conc. = \frac{\langle N \rangle}{V_{eff}}$$

where *N* states the average number of particles within the effective volume V_{eff}, and G_0 represents the height of the autocorrelation function at t=0.

Background corrections

In order to estimate the contribution of the background noise, 22 wild-type embryos were measured with the same laser intensity (10 μW) and in roughly the same plane and developmental stage as the Asl-GFP embryos. Despite no observable correlated background, the uncorrelated background contributed ~30% of the total photon count rate, presumably due to the low concentration of cytosolic Asl-GFP and the high autofluorescence of the embryo itself. Background corrections were performed after the autocorrelation analysis by calculating the correction factor χ^2 using the following formula [23]:

$$\frac{1}{\chi^2} = \frac{1}{(1 + \langle b \rangle / \langle f \rangle)^2}$$

$$\langle N \rangle = \frac{1}{\chi^2 G_0}$$

where $\langle b \rangle$ denotes the average background and $\langle f \rangle$ states the average count rate of the sample.

Quantification and Statistical Analysis

The details for quantification, statistical tests, sample numbers, definitions of centre, and the measures for dispersion and precision are described in the main text, relevant figure legends, or relevant sections of the *Materials and Methods*. Significance in statistical tests was defined by $P < 0.05$. To determine whether the data values were normally distributed, a D'Agostino–Pearson omnibus normality test was applied. Prism 7 was used for all the modelling and statistical analyses.

Supplementary Text

Further information about the mathematical modelling

To assess the validity of our mathematical model (Fig. 4, A and B; see *Mathematical Modelling* section in *Materials and Methods*), we first used the model to individually fit the discrete Plk4-NG oscillation data from S-phase of cycles 11, 12 and 13 (Fig. 4C). The best-fit parameter values fit the data for each cycle well (R^2≥0.99) and generated biologically plausible parameters for k_1, k_2 and k_3, and the total amount of Asl receptor at the centriole (A_{tot}). Note that k_2 describes the rate at which Plk4 phosphorylates Asl: as a simplification, we assumed that k_2 is constant for each of the multiple phosphorylation sites in Asl, and that the bound Plk4 molecule sequentially phosphorylates one site after another. The model worked best with 9 Asl phosphorylation sites, but produced reasonable fits with anywhere between 4-14 sites (Fig. S14). We therefore assumed 9 phosphorylation sites in all subsequent modelling. We then probed the parameter space for any parameter values that would provide a good fit to the data by using Markov chain Monte Carlo methods. For all parameters except k_3, the best-fit values occupied a single, narrow region of the parameter space. The Monte Carlo results revealed that parameter k_3 was very insensitive and could provide a good fit to the data for a broad range of values (Fig. S15). This is presumably because the rate of phosphorylating Asl at multiple sites is relatively slow compared to the rate at which Plk4 is subsequently released from the multiply phosphorylated Asl—so the rate of release is not limiting. To ease the intuitive comparison between different parameters, we held k_3 at an arbitrary constant value in all the models we show here (Tables S1–S3).

Interestingly, the best-fit parameters for cycles 11, 12 and 13 showed that the biggest difference between each cycle is in k_1—the rate at which Plk4 binds to Asl (which is dependent on the cytoplasmic concentration of Plk4). Although our model assumes that the cytoplasmic concentration of Plk4 remains constant during the S-phase period within each cycle, if the phosphorylated Plk4 molecules that are released from the Asl receptor are ultimately degraded—and there is good evidence that Asl activates Plk4 to promote Plk4 degradation [24]—there could be a wave of phosphorylated-Plk4 degradation in the cytoplasm towards the end of S-phase. If this were the case, the cytoplasmic levels of Plk4 would get successively lower at the start of each successive cycle, as predicted by the model (Table S1; see k_1). Unfortunately, we have been unable to monitor Plk4-NG levels using FCS as its cytoplasmic levels are too low.

We then tested the effect of reducing the genetic dose of *Plk4* by half (in *Plk4-NG*$^{1/2}$ embryos—see main text for details). We were unable to detect endogenous Plk4 by western blot in embryos [4], so we could not test how Plk4 protein levels respond to this reduction in gene dosage. When we fit our model to the Plk4-NG oscillation under *Plk4-NG*$^{1/2}$ conditions, however, the best-fit (R^2=0.996) parameter encouragingly had k_1 that was ~39% of the control value (Table S2). In addition, these parameter values suggested that the total amount of centriolar Asl (A_{tot}) should remain relatively unchanged

between the *Plk4-NG* and *Plk4-NG*$^{1/2}$ conditions (Table S2). To test this, we looked at centriolar Asl levels in embryos expressing Asl-mCherry in either WT vs *Plk4*$^{1/2}$ conditions, and found that this was the case (Fig. S16, A and B). Furthermore, the model indicated that the initial amount of Plk4-NG bound to Asl ($\hat{A}_0$) in *Plk4-NG*$^{1/2}$ conditions should be 75% of that in WT conditions (Table S2). Our measurements of centriolar Plk4-NG in these conditions suggested that this difference is ~73%, supporting the prediction of our model (Fig. 4D).

We next modelled the effect of reducing the genetic dose of *asl* by half (*asl*$^{1/2}$ embryos). The best-fit parameter values (R^2=0.999) predicted that the total centriolar Asl levels (A_{tot}) would be reduced by 28% in *asl*$^{1/2}$ embryos (Table S3). We therefore directly measured this value in embryos expressing either one or two copies of Asl-GFP (under the control of its own promoter in an *asl* mutant background) and encouragingly found that reducing the genetic dose of Asl-GFP by half led to a reduction of ~30-35% in centriolar Asl-GFP levels (Fig. S16, C and D). In addition, these parameter values suggested that the concentration of Plk4 (incorporated in the k_1 term) should not vary significantly between WT and *asl*$^{1/2}$ conditions (Table S3). Despite extensive efforts, we could not detect Plk4-NG in immunoblots with any of the commercially available anti-mNeonGreen antibodies we tried, probably because its levels are too low (data now shown). We were, however, able to weakly detect Plk4-GFP in immunoblots (Fig. S16E), so we tested the prediction of the model by blotting for Plk4-GFP (transgenically expressed from its own promoter in a *Plk4* mutant background) in control or *asl*$^{1/2}$ embryos. This revealed that the amount of Plk4-GFP did not change dramatically between the control and *asl*$^{1/2}$ conditions (Fig. S16E). Moreover, the model suggested that the initial amount of Plk4-NG bound to Asl ($\hat{A}_0$) in *asl*$^{1/2}$ conditions should be 73% of that in control conditions (Table S3). Encouragingly, our direct measurements of centriolar Plk4-NG in these conditions suggested that this difference is ~67% (Fig. 4E). Taken together, these observations suggest that our model can robustly describe the Plk4-NG oscillations under normal conditions (Fig. 4C) and when the levels of either Plk4 or Asl are perturbed experimentally (Fig. 4D and E). Moreover, the model makes plausible predictions about the relative levels of these proteins in the perturbed conditions that are close to the levels that we subsequently measured experimentally.

Finally, we noticed that the best-fit value of k_2 (reflecting the kinase activity of individual Plk4 molecules) decreased slightly between cycles 11 to 12 and decreased more significantly between cycles 12 to 13 (by ~9% and ~37%, respectively); k_2 also decreased when levels of Plk4 were genetically reduced in *Plk4-NG*$^{1/2}$ embryos (by ~25%)—but not when Asl levels were genetically reduced in *asl*$^{1/2}$ embryos (Tables S1–S3). We do not currently understand the molecular basis for this potential decrease in kinase activity at successive cycles, but we have suggested previously that centriolar Plk4 must integrate several inputs at the start of each cycle (from, for example, cell cycle regulators, or its activator Ana2/STIL), allowing it to lower its kinase activity in response to the lengthening of S-phase during successive nuclear cycles [4].

Our mathematical model describes how Plk4 levels oscillate during S-phase at a single site on the side of the mother centriole where the daughter centriole assembles, as our super-resolution imaging indicates that Plk4-NG is only detectable at this site during S-phase (Fig. S4). We suspect that a similar model can explain how Plk4 binds to and dissociates from the Asl receptor that surrounds the rest of the mother centriole, but that this pool of Asl is phosphorylated by Plk4 (and so effectively inactivated) very rapidly during mitosis—perhaps because there is very little Ana2 and/or Sas-6 associated with this pool of Asl/Plk4. Thus, Plk4 initially binds to Asl around the entire mother centriole during mitosis but this binding is very transient, as Plk4 rapidly phosphorylates Asl and so dissociates. At the site of daughter centriole assembly, the presence of other factors (such as Ana2, Sas-6 and Sas-4), might modify the behaviour of the Asl:Plk4 complex, so that Plk4 is retained for longer and can promote cartwheel assembly. While speculative, this idea could also explain how new-mother and old-mother centrioles can both assemble a daughter centriole with similar kinetics, even though new-mother centrioles initially associate with much less total Asl than old-mother centrioles [5] (Fig. S16); perhaps the new-mother and old-mother centrioles have similar amounts of Asl specifically at the site of daughter centriole assembly, while new-mother centrioles have less Asl at other sites.

Figure S1

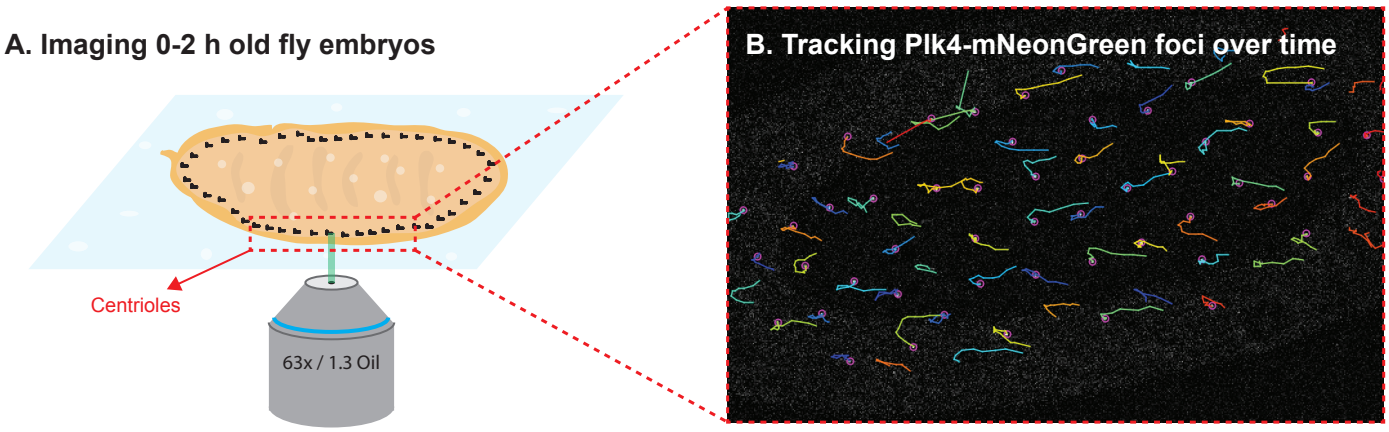

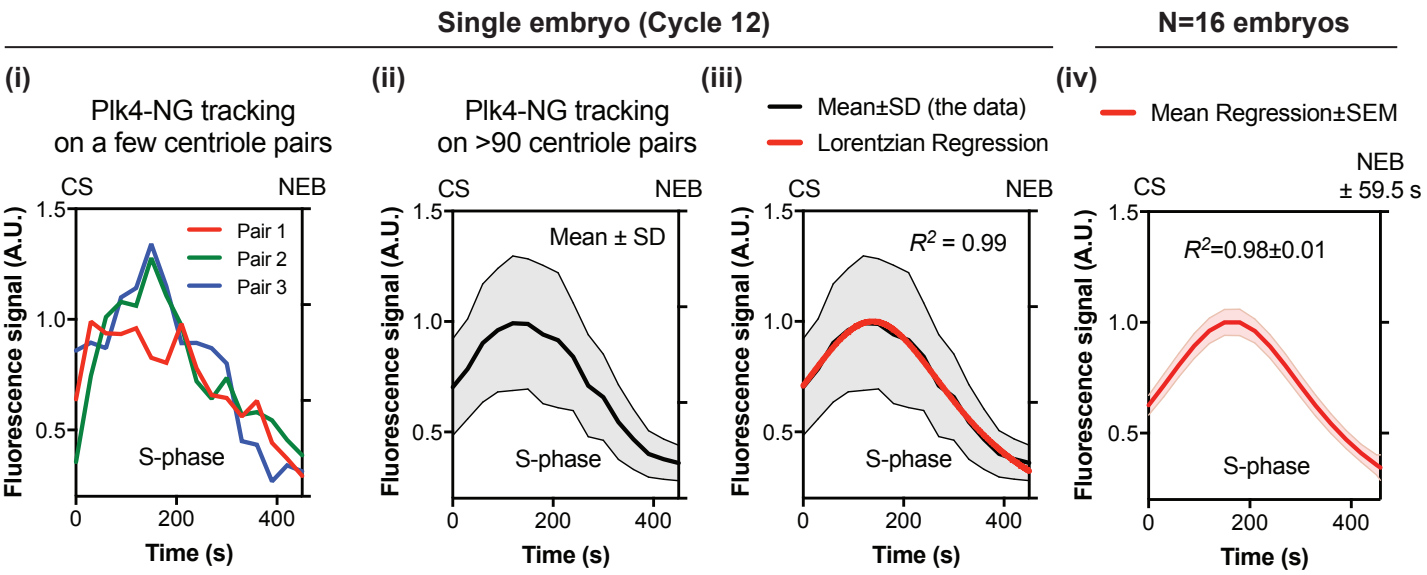

D. Rationale for the regressian analysis (above)

N = 27 embryos*	Lorentzian	Gaussian	Inc. - Const. - Dec.	Inc. - Dec.
	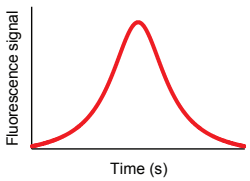	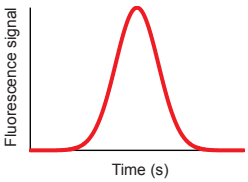	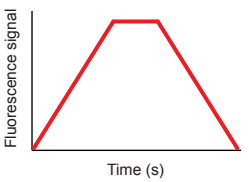	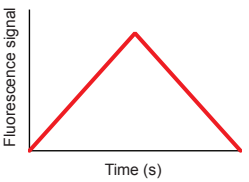
Deg. of freedom	13	13	11	12
R^2 value	0.98±0.01	0.97±0.01	0.98±0.01	0.97±0.01
SS_{Abs}	0.015±0.009	0.022±0.022	0.017±0.021	0.022±0.021
% of fit preference	52%	40%	4%	4%

*Data used for this analysis (cycle 12) were taken from figs. 1B and 4D.

Supplementary Figure Legends

Figure S1. Summary of the protocol for image acquisition, processing and analysis of the Plk4-NG oscillations.
(A) Cartoon illustrates the centrioles in ~2 h old embryo expressing Plk4-NG being imaged on a spinning-disk confocal system. **(B)** Micrograph shows a typical image of the tracks of the Plk4-NG centrioles in S-phase of cycle 12, tracked using the ImageJ plugin, TrackMate. **(C)** Graphs show the Plk4-NG oscillation during cycle 12 in a single embryo quantified from the tracks of either several individual centriole pairs (i), or the Mean±SD oscillation calculated from the tracks of >90 centriole pairs (ii). The data for each embryo was then regressed using a Lorentzian equation (*red line*, iii)—see (D) for an explanation of the rationale for choosing this function. This process was repeated for multiple embryos to calculate a Mean±SEM regression for nuclear cycle 12 (iv). R^2 values indicate the goodness-of-fit (Mean±SD) of the regression. CS=time of centrosome separation (set to 0); NEB=time of nuclear envelope breakdown. **(D)** Table shows the various models that were tested to fit the Plk4-NG oscillation data. R^2 and SS_{Abs} (absolute sum of squares) values indicate the goodness of fit. The Lorentzian function was the best fit for the majority of embryos, so it was used for all further analyses. Further details of these models are provided in *Materials* and *Methods*.

Figure S2

Plk4-NG oscillations in individual embryos

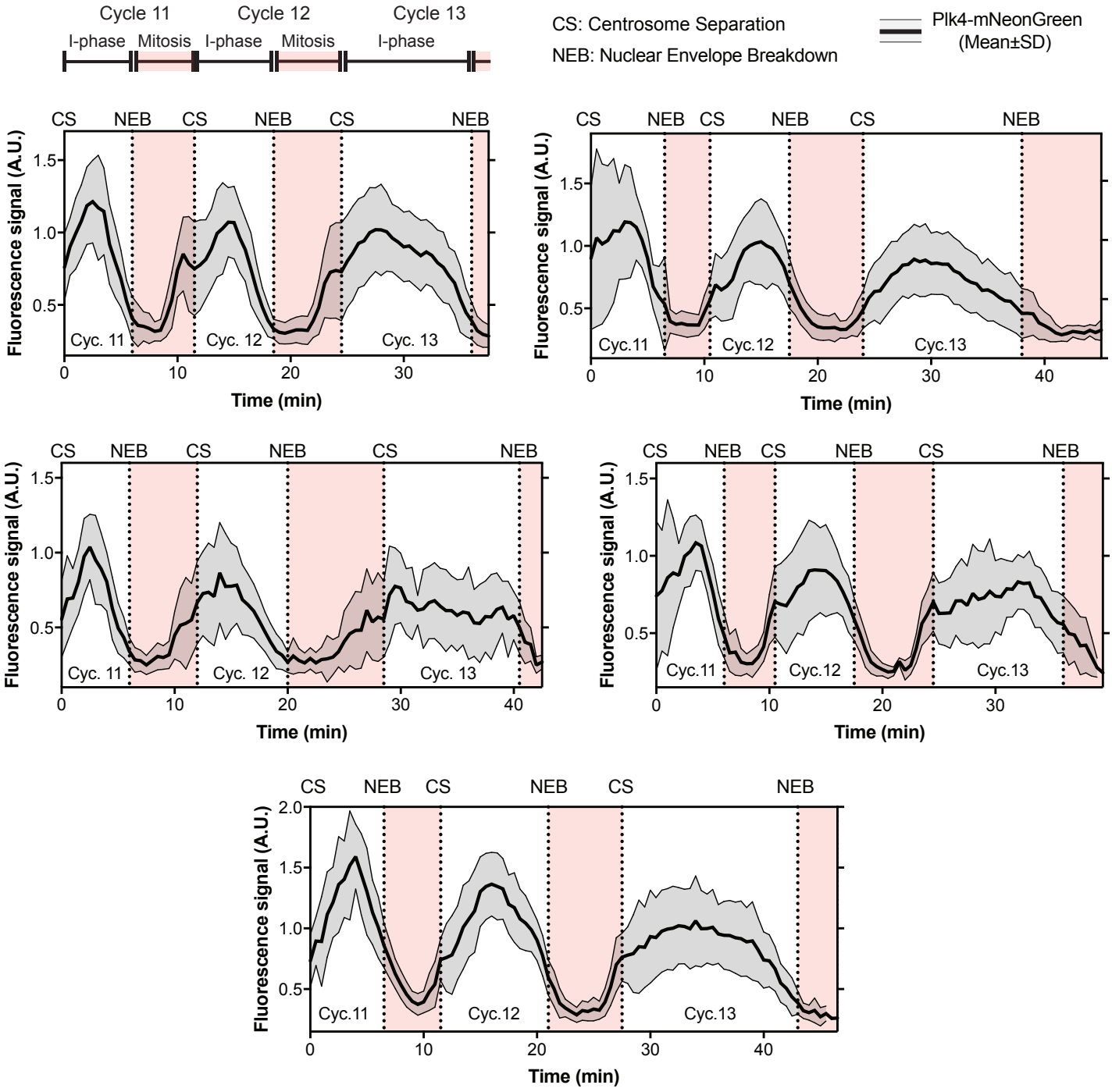

Figure S2. Plk4-NG oscillations in individual embryos.
Graphs show the Mean±SD centriolar fluorescence intensity of Plk4-NG (two copies of a transgene expressed from its own promoter in a *Plk4* null mutant background) during nuclear cycles 11-13 in 5 different embryos imaged on a spinning-disk confocal system. n=26 centrioles (mean) tracked starting from cycle 11 per embryo. See *Materials* and *Methods* for full details of image acquisition and data analysis.

Figure S3

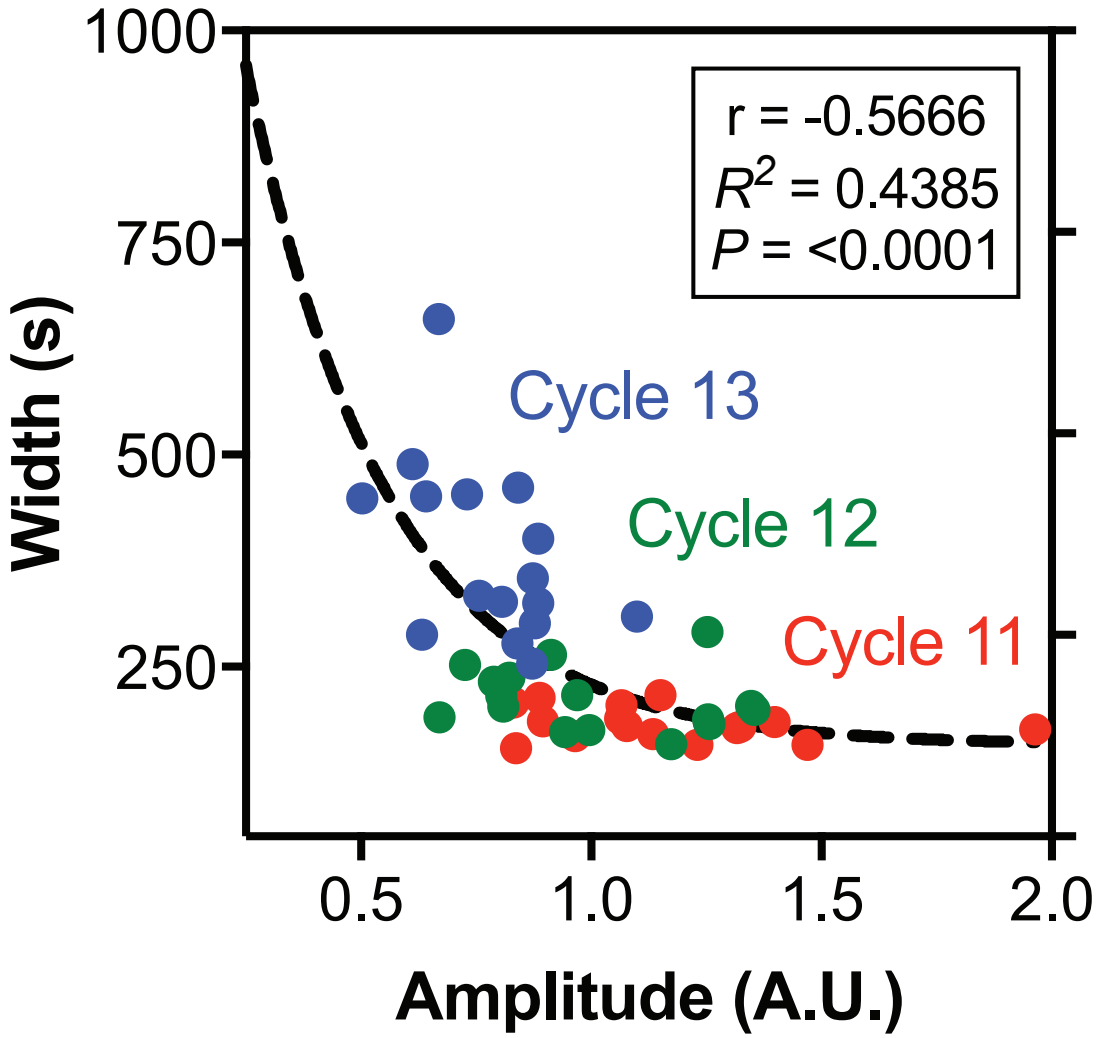

Figure S3. The inverse relationship between the width and amplitude of the Plk4-NG oscillations suggests an adaptive mechanism.
Scatter plot shows the negative correlation between the width (full width at half maximum amplitude; *T*) and the amplitude of Plk4-NG oscillations in cycles 11-13 (colour coded *red*, *green* and *blue*, respectively)—derived from the data shown in Fig. 1B. The plot was regressed using the *one phase decay* function in Prism 7 (GraphPad). Correlation strength was examined using Pearson's correlation coefficient ($r<0.40$ weak; $0.40<r<0.60$ moderate; $r>0.6$ strong), and the significance of correlation was determined by the p-value ($P<0.05$).

Figure S4

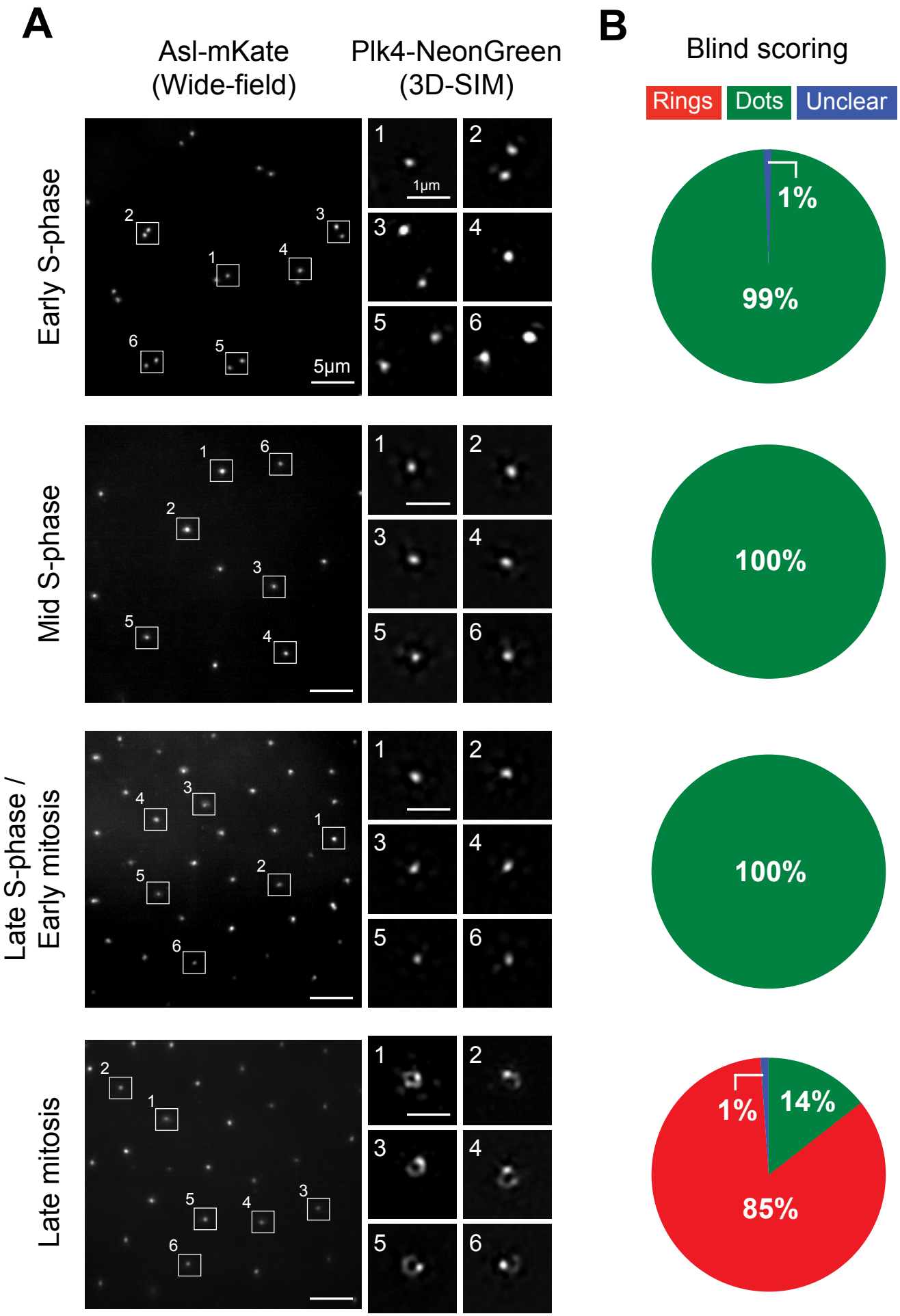

Figure S4. A spatiotemporal analysis for the Plk4-NG localization on the mother centriole.

(A) Micrographs show the centriolar localisation of either Asl-mKate2 (a mother centriole marker) observed by widefield microscopy (left panels), or a close up view of Plk4-NG at selected centrioles (indicated by numbered boxes) observed by 3D-Structured Illumination super-resolution Microscopy (3D-SIM). Individual living embryos were monitored by widefield microscopy and a single 3D-SIM image of Plk4-NG was taken at the desired stage (as indicated). Plk4-NG was observed either as a single dot (during early S-phase to late S-phase/early mitosis—see corresponding 3D-SIM images), or as a ring around the mother centriole that was usually somewhat or highly enriched at a single dot on the ring (during late mitosis—see corresponding 3D-SIM images). We conclude that centriolar Plk4-NG is localised as a single dot throughout S-phase, which is the period during which our analysis of the Plk4-NG oscillation is performed. The assessment for signal quality in the SIM data was done using the *Modulation contrast-to-noise ratio (MCNR) heat map* function in SIMCheck, a plugin of ImageJ [17]. Only centrioles that passed this quality control were analysed. **(B)** Pie charts quantify the percentage of centrioles in a dot (*green*) or ring-like (*red*) conformation at each time point. This analysis was performed blind by 3 independent assessors, none of whom were involved in collecting the data; pie charts show the average of the three scores. N=6 embryos per cell cycle stage indicated; n=20 centrioles per embryo.

Figure S5

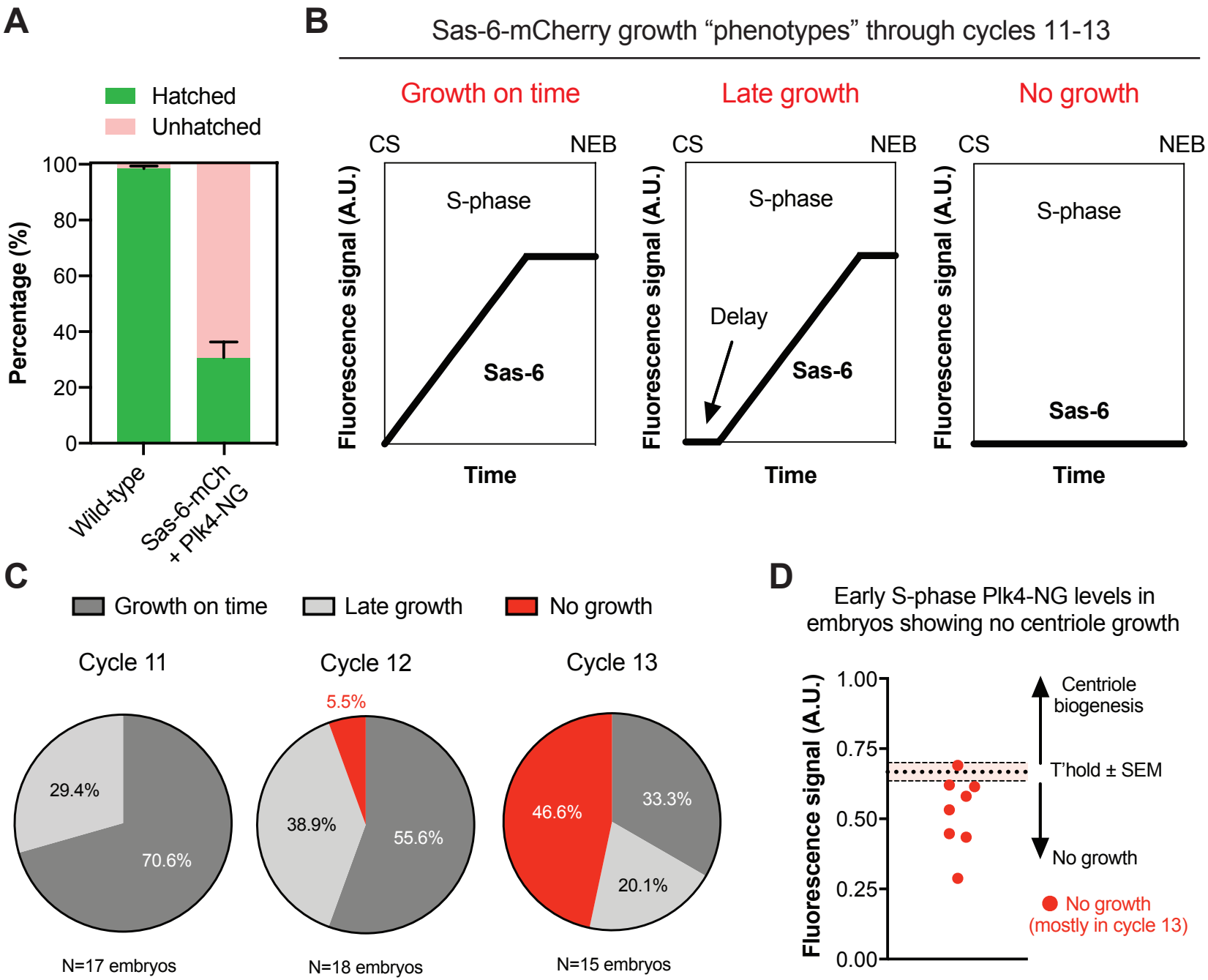
A
Hatched
Unhatched
Percentage (%)
100
80
60
40
20
0
Wild-type
Sas-6-mCh + Plk4-NG
B
Sas-6-mCherry growth "phenotypes" through cycles 11-13
Growth on time
Late growth
No growth
CS
NEB
S-phase
Sas-6
Delay
Fluorescence signal (A.U.)
Time
C
Growth on time
Late growth
No growth
Cycle 11
Cycle 12
Cycle 13
29.4%
70.6%
5.5%
38.9%
55.6%
46.6%
33.3%
20.1%
N=17 embryos
N=18 embryos
N=15 embryos
D
Early S-phase Plk4-NG levels in embryos showing no centriole growth
Fluorescence signal (A.U.)
1.00
0.75
0.50
0.25
0.00
Centriole biogenesis
T'hold ± SEM
No growth
No growth (mostly in cycle 13)

Figure S5. Embryos whose Plk4 oscillations do not reach a minimum threshold amplitude do not appear to assemble daughter centrioles. **(A)** Graph quantifies the embryo hatching frequency in wild-type (Oregon R) flies or in flies that simultaneously express Sas-6-mCherry and Plk4-NG in a *Plk4* mutant background (all mated with WT males). The latter flies laid embryos that were less efficient in hatching in comparison to the wild-type ones. **(B)** Cartoon graphs illustrate the three different centriole growth "phenotypes" we observed in these *Plk4* mutant embryos that simultaneously express 2 copies of Plk4-NG and one copy of Sas-6-mCherry. CS=centrosome separation and NEB=nuclear envelope breakdown. In our previous analysis of centriole growth kinetics [4] almost all embryos started to incorporate Sas-6-GFP at the very start of S-phase ("Growth on time", left graph). In the embryos analysed here (with a more complicated genotype, and expressing Sas-6-mCherry rather than Sas-6-GFP) some of the embryos exhibited a clear delay in initiating the incorporation of Sas-6-mCherry ("Late growth", middle graph), while others did not appear to incorporate significant amounts of Sas-6-mCherry at all ("No growth", right graph)—and, as described above, many of these embryos failed to hatch as larvae. Embryos exhibiting this last phenotype were excluded from the analysis shown in Fig. 2, but were analysed separately, as described below. **(C)** Pie charts quantify the percentage of embryos exhibiting the centriole growth "phenotypes" illustrated in (A) at each nuclear cycle. **(D)** We observed 8 embryos in total that exhibited the "No growth" phenotype (1 in cycle 12, and 7 in cycle 13). Centriolar Plk4-NG levels continued to oscillate in these embryos, and the scatter chart plots the amplitude of the Plk4-NG oscillations in these 8 embryos overlaid on the average "threshold" level of Plk4-NG at which centrioles started to grow in the population of these embryos that did exhibit Sas-6-mCherry incorporation (i.e. the "Growth on time" and "Late growth" embryos). This threshold was very similar at cycle 12 and 13, so the threshold shown here is taken from cycle 13 embryos. Note how the Plk4-NG oscillation in all but one of these 8 embryos fails to reach the average "threshold" level that would normally initiate centriole growth in these embryos.

Figure S6

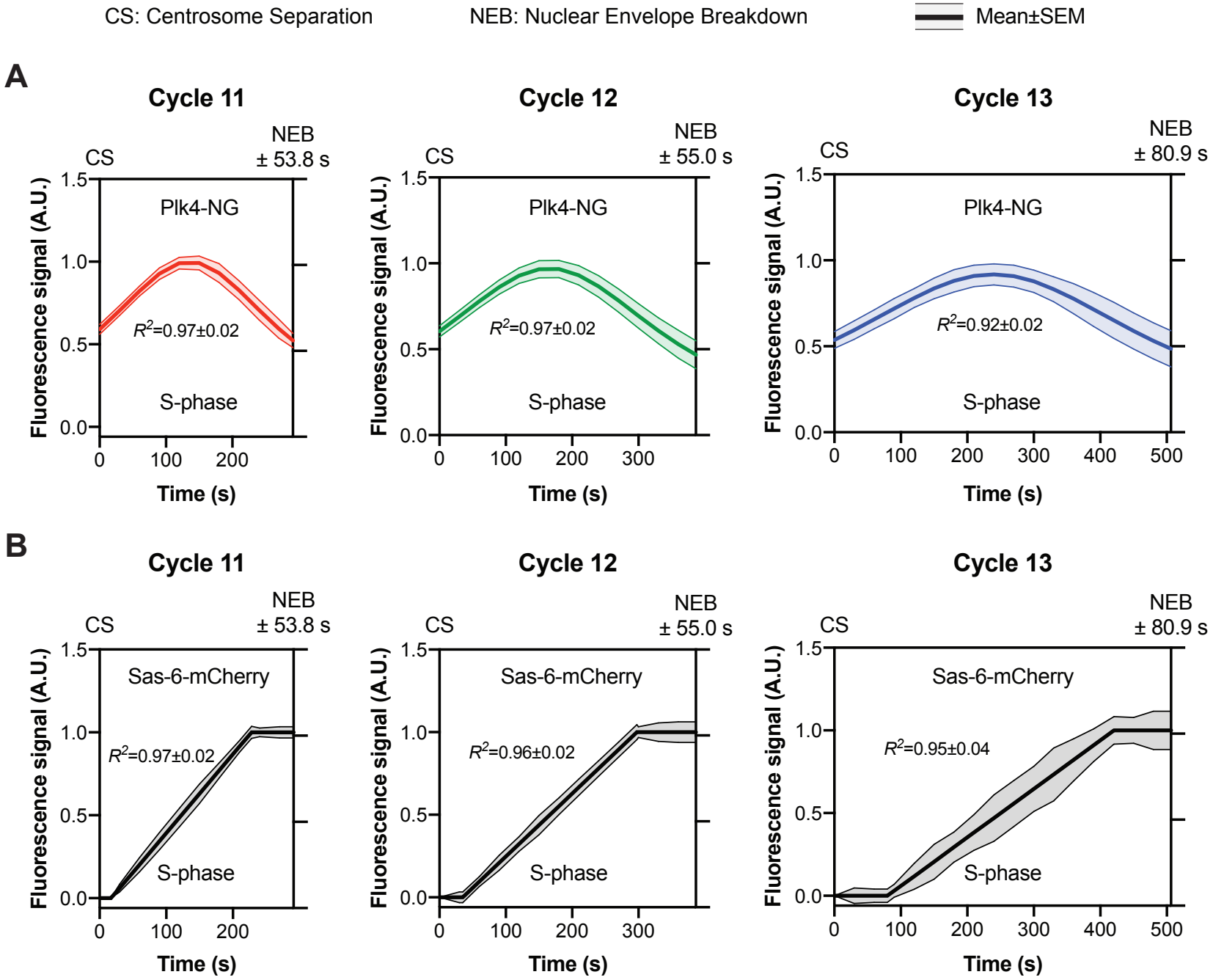
CS: Centrosome Separation
NEB: Nuclear Envelope Breakdown
Mean±SEM
A
Cycle 11
Cycle 12
Cycle 13
CS
NEB
± 53.8 s
± 55.0 s
± 80.9 s
Plk4-NG
R^2=0.97±0.02
R^2=0.97±0.02
R^2=0.92±0.02
S-phase
Fluorescence signal (A.U.)
Time (s)
B
Cycle 11
Cycle 12
Cycle 13
Sas-6-mCherry
R^2=0.97±0.02
R^2=0.96±0.02
R^2=0.95±0.04
S-phase
Fluorescence signal (A.U.)
Time (s)

Figure S6. Plk4-mNeonGreen and Sas-6-mCherry fluorescence intensities showing the standard error.
In Fig. 2, the graphs for Plk4-NG and Sas-6-mCherry fluorescence intensity are plotted without the deviation or error bars for ease of presentation. The graphs shown here show the same data together with the standard error of the mean for **(A)** the Plk4-mNeonGreen and **(B)** the Sas-6-mCherry fluorescence intensity profiles. CS=centrosome separation and NEB=nuclear envelope breakdown. R^2 values indicate the goodness of fit.

Figure S7

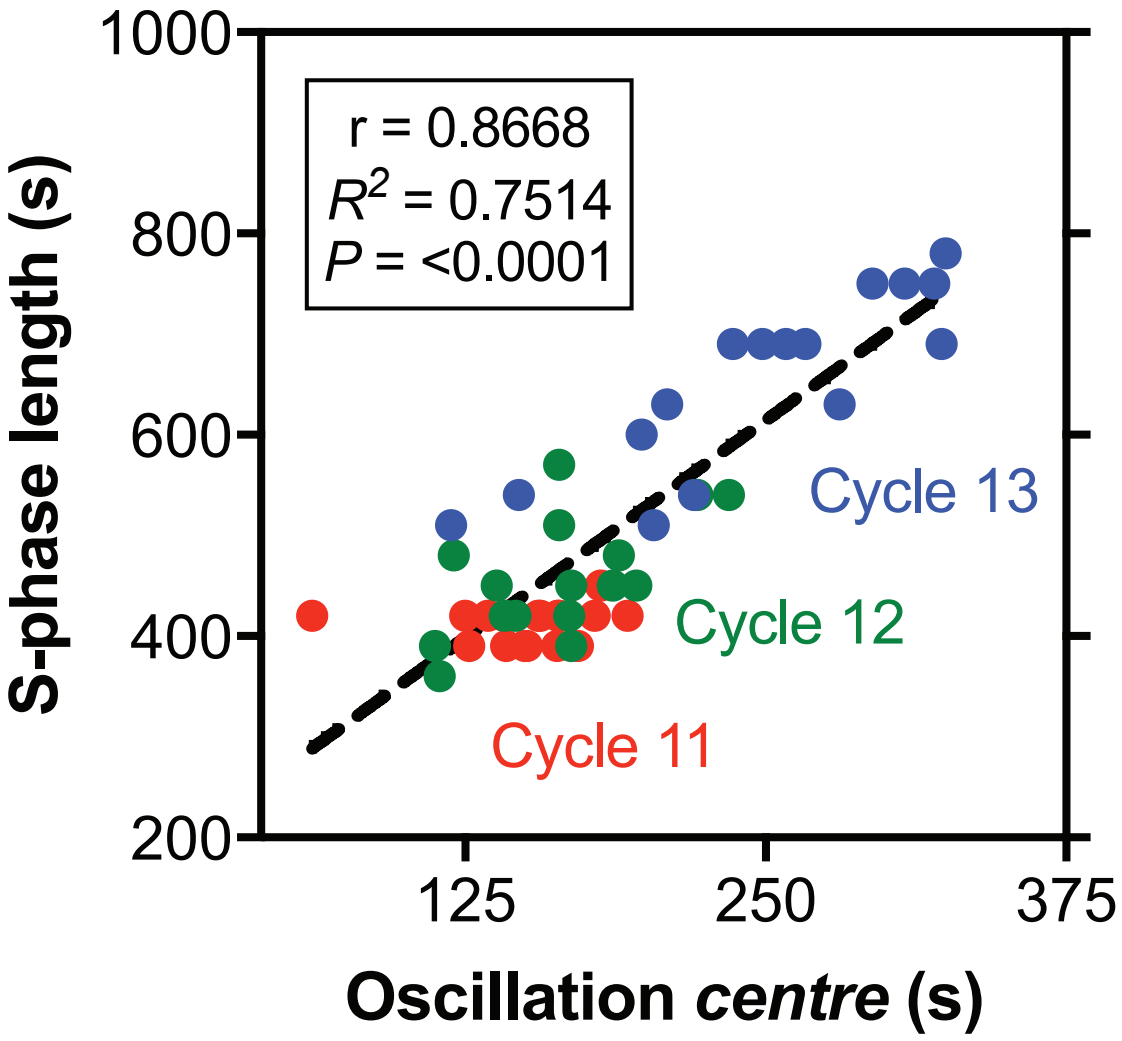

Figure S7. S-phase length and the *centre* (peak) timing of the Plk4-NG oscillations are strongly correlated.

Scatter plot shows the strong positive correlation between S-phase length and the *centre* (peak) of the Plk4-NG oscillations in cycles 11-13 (colour coded with *red*, *green* and *blue*, respectively). The plot was regressed using the *line* function in Prism 7 (GraphPad). Correlation strength was examined using Pearson's correlation coefficient ($r<0.40$ weak; $0.40<r<0.60$ moderate; $r>0.6$ strong), and the significance of correlation was determined by the p-value ($P<0.05$). The data were extracted from the data shown in Fig. 1B.

Figure S8

Late Cyclin A-B-B3 dsRNA injection experiments

*Example experiment schematic from Figure 3

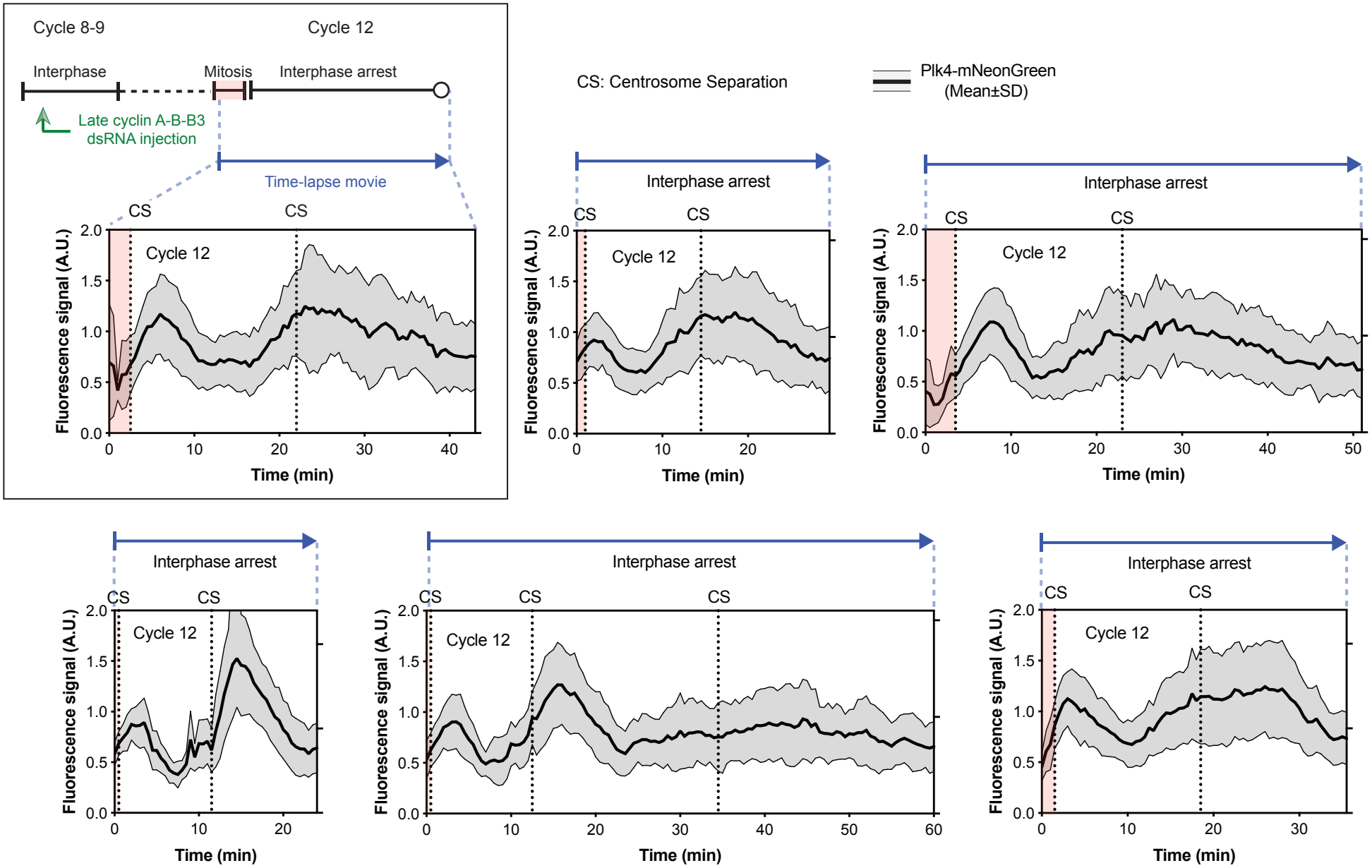

Figure S8. Plk4-NG oscillations and centriole duplication continue in embryos arrested in interphase by mitotic cyclin depletion.
Graphs follow the same schema for the “late” Cyclin A-B-B3 dsRNA injection experiment shown in Fig. 3C (which is reproduced here in the box); graphs from 5 additional injected embryos are shown here. Note how Plk4-NG goes through multiple synchronous oscillations in these embryos that are arrested in interphase.

Figure S9

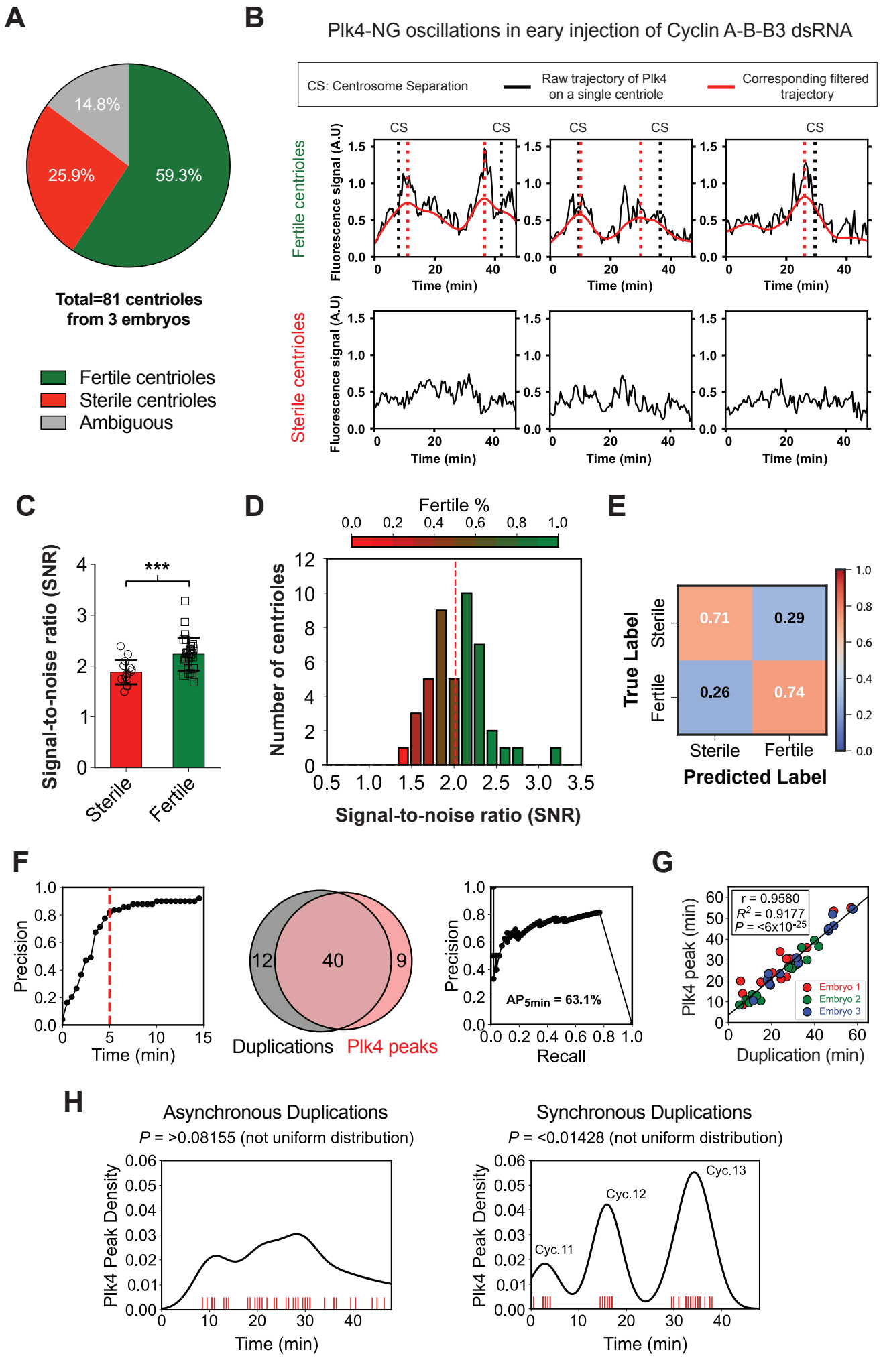

Figure S9. Plk4-NG oscillations continue on stochastically duplicating centrioles in embryos arrested in interphase by mitotic cyclin depletion. **(A)** The pie chart quantifies the percentage of centrioles that continued to duplicate in embryos where Cyclin A-B-B3 dsRNA was injected "early": i.e. into younger embryos, and centriole behaviour was then assayed ~60mins later. *Ambiguous* (grey) indicates the fraction of centrioles whose duplication state was difficult to determine due to their drifting out of view at some point during imaging. **(B)** Graphs show representative Plk4-NG fluorescence signals from individual fertile and sterile centrioles in a single injected embryo. *Black solid* trajectory is the raw Plk4-NG signal; *Red solid* trajectory is the corresponding filtered signal; *Black dotted* lines mark observed centriole duplication events (CS: Centrosome Separation). *Red dotted* lines mark the computationally determined Plk4-NG fluorescence peaks on fertile centrioles (see *Materials and Methods*). **(C)** Barchart shows the mean signal-to-noise ratio (SNR) of Plk4-NG fluorescence signals from sterile and fertile centrioles (*red* and *green*, respectively). Data are presented as Mean±SD. Statistical significance of SNR was tested using *t*-test assuming equal variance (***, $P<0.001$). **(D)** Heatmap histogram of all SNR values from sterile and fertile centrioles. *Red* dashed line shows the unbiased threshold, determined automatically from Otsu thresholding for distinguishing sterile and fertile centrioles. Heatmap (*Red*: Sterile and *Green*: Fertile) indicates the fraction of fertile/sterile centrioles in each column. Note that, the higher the SNR, the more fertile the centrioles are. **(E)** Confusion matrix showing the classification performance of sterile versus fertile centriole Plk4-NG signals using the Otsu threshold in (D) as a proportion of the total number of signals, n=45 centrioles from 3 embryos. **(F)** Graph (left) shows the precision of using Plk4-NG fluorescence peaks to predict the time of centriole duplication as a function of the cut-off time allowed to score a positive prediction (see *Materials and Methods*). *Red dashed* line marks the 5 min cut-off (i.e. when a Plk4-NG peak and centriole duplication (CS) event are less than 5 min apart): using this cut-off, the prediction precision is ~80%. The Venn diagram shows the prediction performance of Plk4-NG peaks for centriole duplication based on a 5 min time cut-off for a positive prediction. Graph (on the right) shows the "precision" versus "recall", using Plk4-NG peak times to predict centriole duplication, given a 5 min cut-off for a positive match. Average precision using this threshold denoted AP_{5min} is also the area under the plotted curve. **(G)** Scatter plot shows the strong linear correlation between the time of Plk4-NG peaks and the time of nearest centriole duplications (N=3 embryos, n=45 centrioles; colored in *red*, *green* and *blue*). Correlation strength was examined using Pearson's correlation coefficient ($r<0.40$ weak; $0.40<r<0.60$ moderate; $r>0.6$ strong), and the significance of correlation was determined by the p-value ($P<0.05$). The fitted linear line has the equation $y=0.87x+3.69$. **(H)** Graphs show the distribution of the detected Plk4-NG fluorescence peaks in asynchronous (n=45) and synchronous (n=225) centriole duplications over a time-window of 48 min. Data for the synchronous centriole duplications were taken from all the uninjected embryos shown in Fig. S2. *Black* solid trajectories show the estimated probability density using Gaussian kernel density estimation (bandwidth=3). *Red* ticks show the time of Plk4-NG peaks. The stochasticity of centriole duplication was statistically assessed by testing departure from a uniform distribution defined on the time interval (0,48 min)

using two-tailed non-parametric Kolmogorov–Smirnov test at 5% significance level (see *Materials and Methods*). Overall, these graphs suggest that the centriole duplications, which happen in embryos injected “early” with cyclin A-B-B3 dsRNA, are stochastic.

Figure S10

Colchicine injection experiments

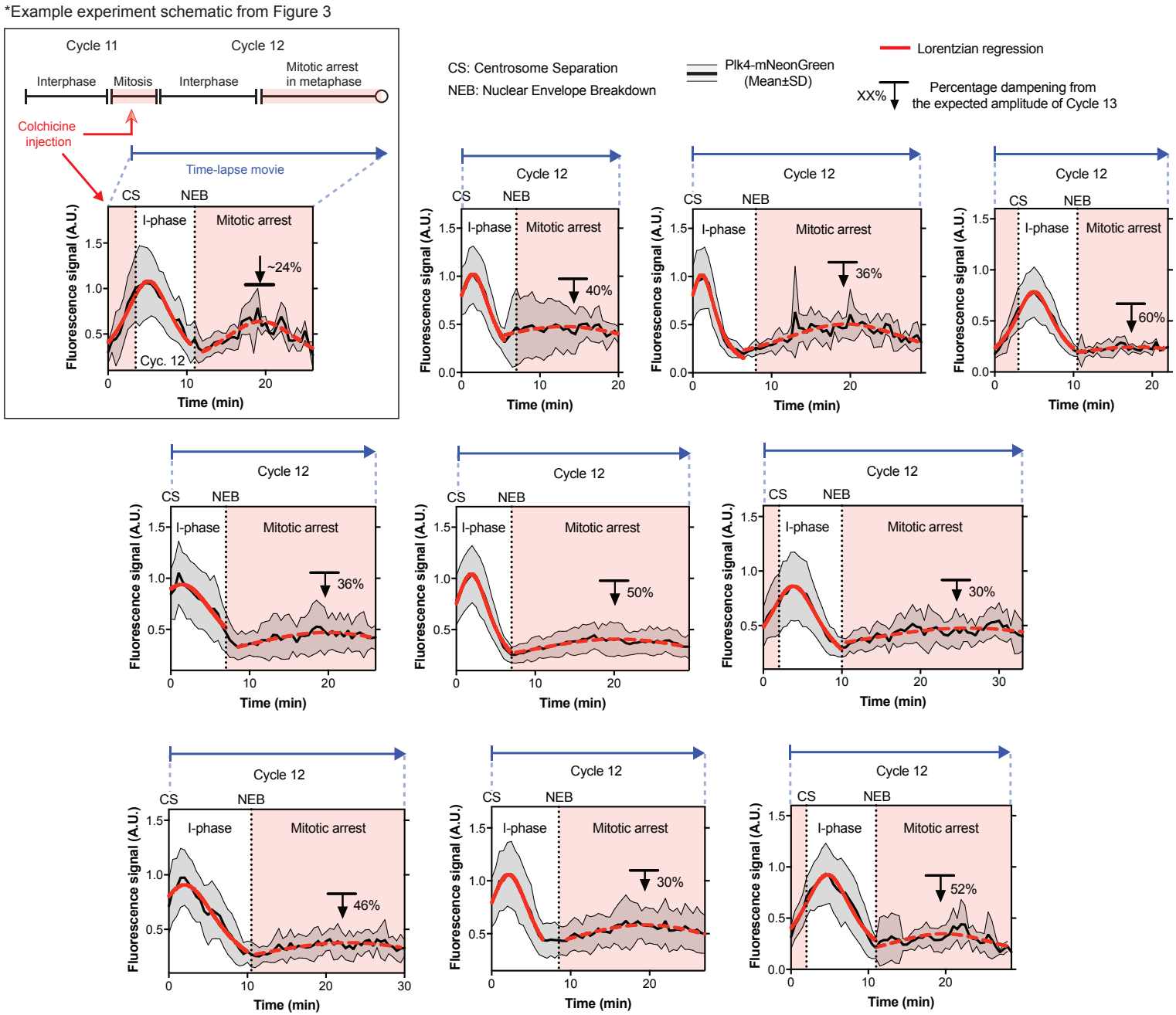

Figure S10. Plk4-NG oscillations continue in embryos after colchicine injection, but with a strongly dampened amplitude.
Graphs follow the same schema for the colchicine injection experiment shown in Fig. 3D (which is reproduced here in the box); graphs from 9 additional injected embryos are shown here. The data was subjected to Lorentzian regression analysis (*solid red* curve for the 1st oscillation after drug-injection; *dashed red* curve for the 2nd oscillation). Note how the second oscillation starts almost immediately after the first oscillation, but its amplitude is strongly decreased in these mitotically arrested embryos (The arrow above each oscillation peak indicates the percentage of dampening compared to the usual cycle 13 oscillation that follows cycle 12). This dampened amplitude makes the oscillation difficult to appreciate in some embryos, but analysis of the regressed data indicates that the average peak amplitude of the second Plk4-NG oscillation in these embryos is significantly higher than the baseline ($P<0.0001$; see Fig. S11A).

Figure S11

A

Amplitude of Plk4 oscillations in colchicine injected embryos

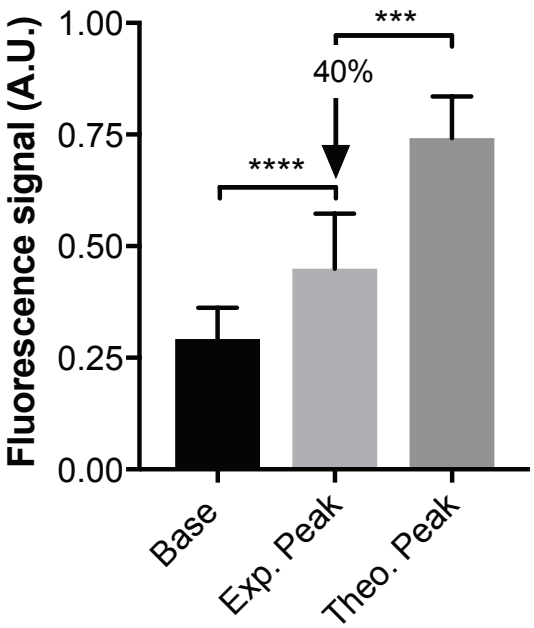

B

Plk4 oscillations in colchicine injected embryos are sub-threshold

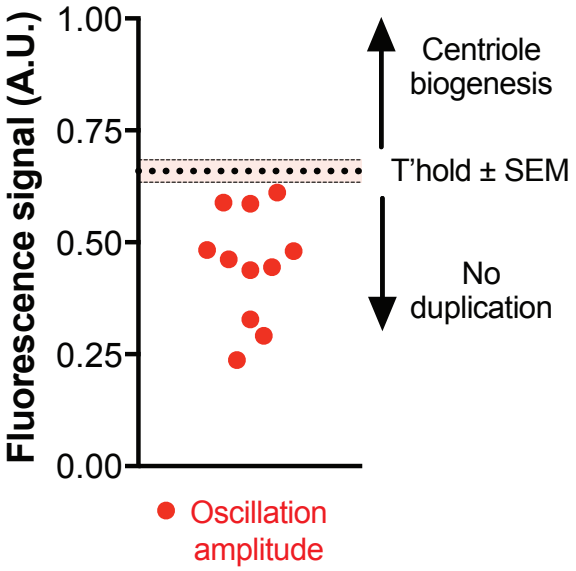

Figure S11. Colchicine injected embryos display sub-threshold Plk4 oscillations for centriole biogenesis.

(**A**) Bar chart illustrates that the amplitude of the second Plk4-NG oscillation observed after colchicine injection (the Experimental Peak—see data in Fig. S10) has a statistically significant difference between the base and the peak of the oscillation. On average, however, this peak is ~40% lower in amplitude than the expected mean amplitude (Theoretical Peak) of the normal Plk4-NG oscillation in cycle 13 (calculated from Fig. 1B). Data are presented as Mean±SD. Statistical significance was assessed using an unpaired *t* test with Welch's correction (for Gaussian-distributed data) or an unpaired Mann-Whitney test (***, P<0.001; ****, P<0.0001). **(B)** Scatter chart shows that the amplitude of the Plk4-NG oscillations observed during the mitotic arrest are below the normal threshold for centriole biogenesis in cycle 13 (threshold adapted and rescaled from the cycle 13 data in Fig. 2). This presumably explains why we do not observe extra rounds of centriole duplication in colchicine-injected embryos despite the continuation of Plk4 oscillations.

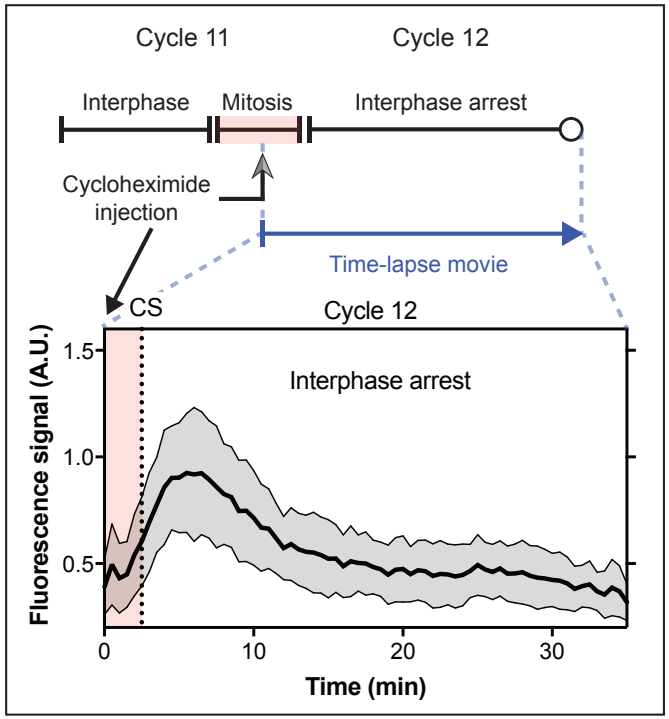

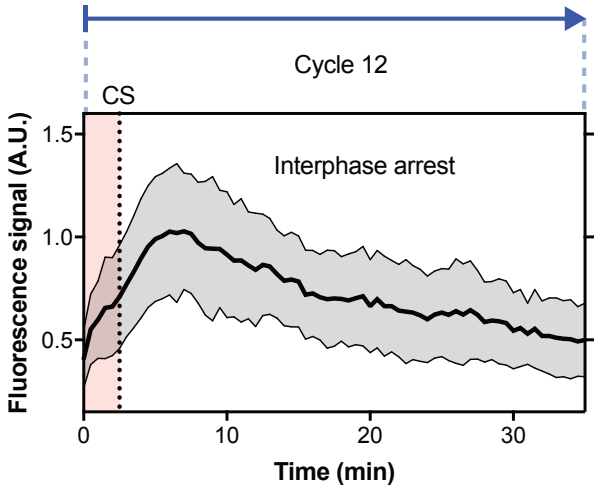

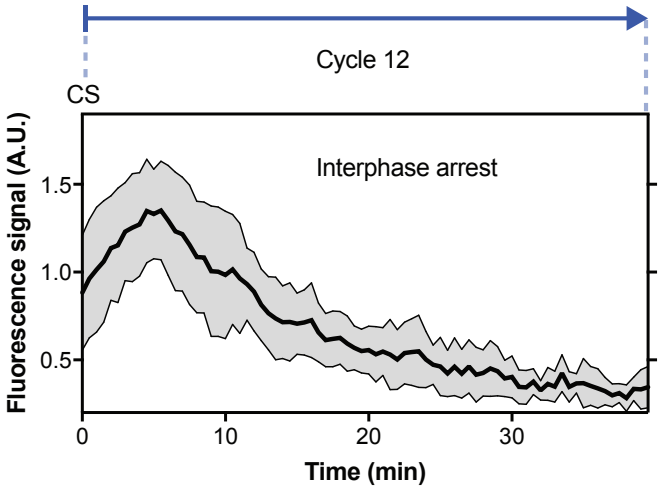

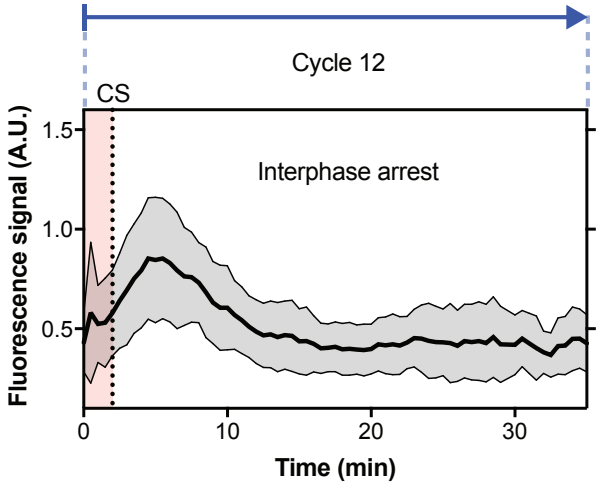

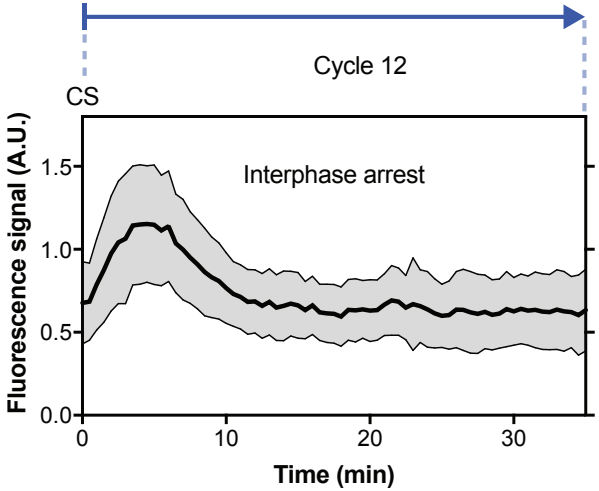

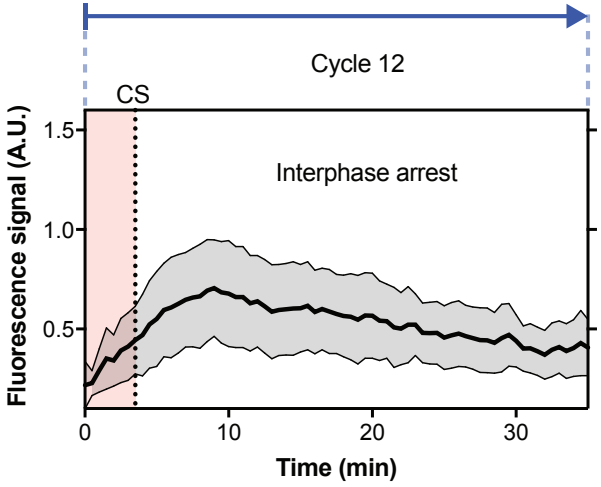

Figure S12

Cycloheximide injection experiments

Figure S12. Plk4-NG oscillations are blocked in embryos after cycloheximide injection.

Graphs follow the same schema for the cycloheximide injection experiment shown in Fig. 3E (which is reproduced here in the box); graphs from 5 additional injected embryos are shown here. Note how Plk4-NG goes through one oscillation after the drug injection, but no further oscillations are observed in these embryos.

Figure S13

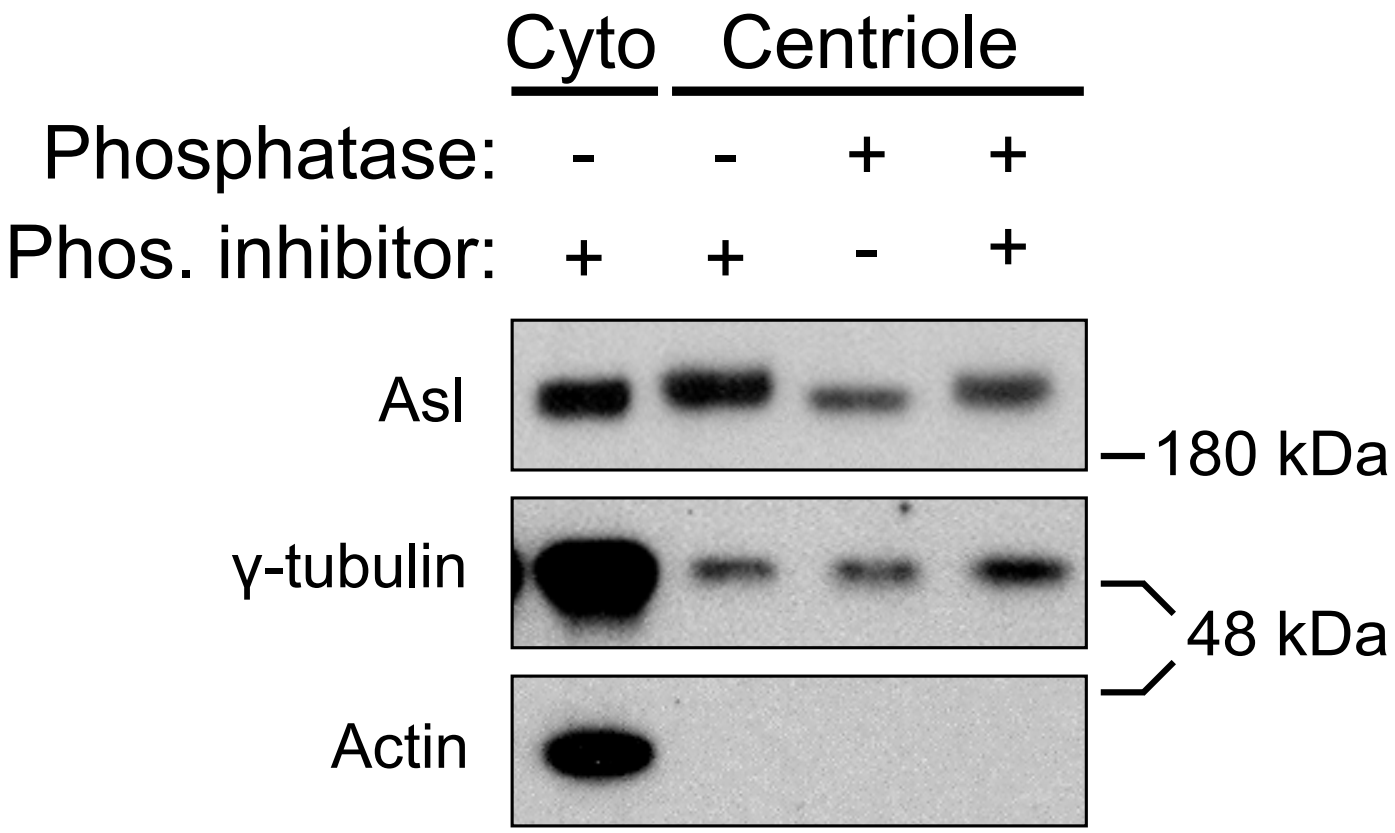

Figure S13. Asterless (Asl) is specifically phosphorylated at centrioles. A western blot of either the cytosolic-fraction or centriole-containing-fraction from embryo extracts in which the centriole-fraction was treated with phosphatase or phosphatase inhibitor (as indicated), and probed with the indicated antibodies. Note that Asl in the centriole-fraction migrates slightly slower than in the cytoplasmic fraction, and this difference is abolished if the centriole-fraction is treated with phosphatase, but not if phosphatase inhibitor is included in the reaction. This suggests that Asl is specifically phosphorylated in the centriole-fraction. The γ-tubulin in the centriole-fraction does not exhibit such a migration shift. Actin is shown as a control that should be present in the cytosolic fractions, but absent in the centriole fractions. Note also that the Actin blot shown here is identical to the one we presented in a previous publication [10], as this blot was performed contemporaneously with the Asl and γ-tubulin blots shown here.

Figure S14

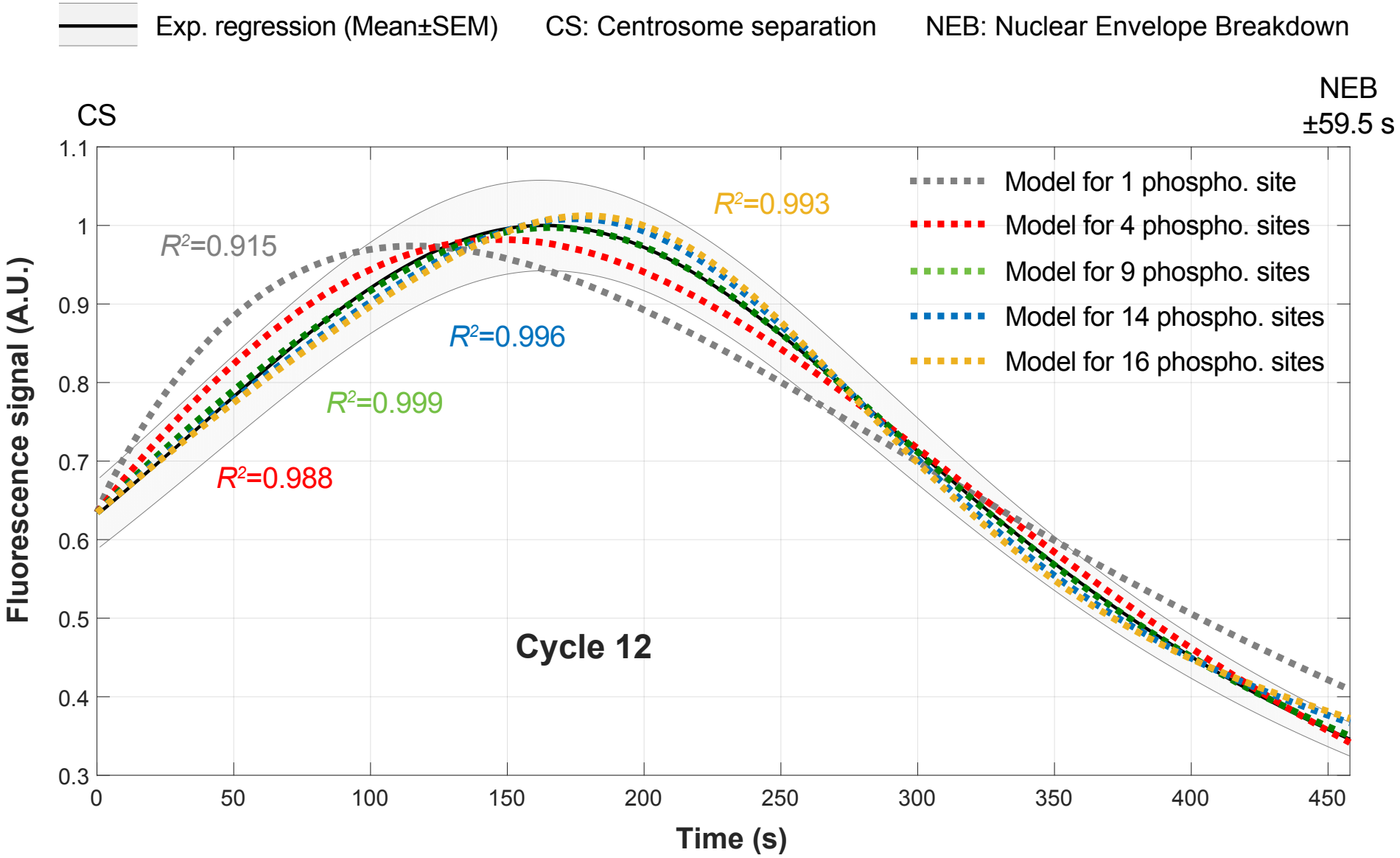
Exp. regression (Mean±SEM)
CS: Centrosome separation
NEB: Nuclear Envelope Breakdown
CS
NEB
±59.5 s
Fluorescence signal (A.U.)
Time (s)
Cycle 12
R²=0.915
R²=0.988
R²=0.999
R²=0.996
R²=0.993
Model for 1 phospho. site
Model for 4 phospho. sites
Model for 9 phospho. sites
Model for 14 phospho. sites
Model for 16 phospho. sites
1.1
1
0.9
0.8
0.7
0.6
0.5
0.4
0.3
0
50
100
150
200
250
300
350
400
450

Figure S14. Determining the effect of the number of phosphorylation sites on the solution to the mathematical model.
Graph shows five different models, each using different values for the number of sites on Asl that are phosphorylated sequentially by Plk4 (*dotted* lines), fit to experimental data (*solid black* line—taken from cycle 12 in Fig. 1B) . The curve $[A_0](t) + [A_1](t) + \cdots + [A_N](t)$ was fit to the data where *N* (the number of sites on Asl that are phosphorylated)=1, 4, 9, 14 or 16 (*grey*, *red*, *green*, *blue* and *yellow dotted* lines, respectively). R^2 values indicate goodness-of-fit for the mathematical solutions. The model with 9 phosphorylation sites fits the data best, so this number was used in all subsequent modelling.

Figure S15

A

Monte Carlo Results

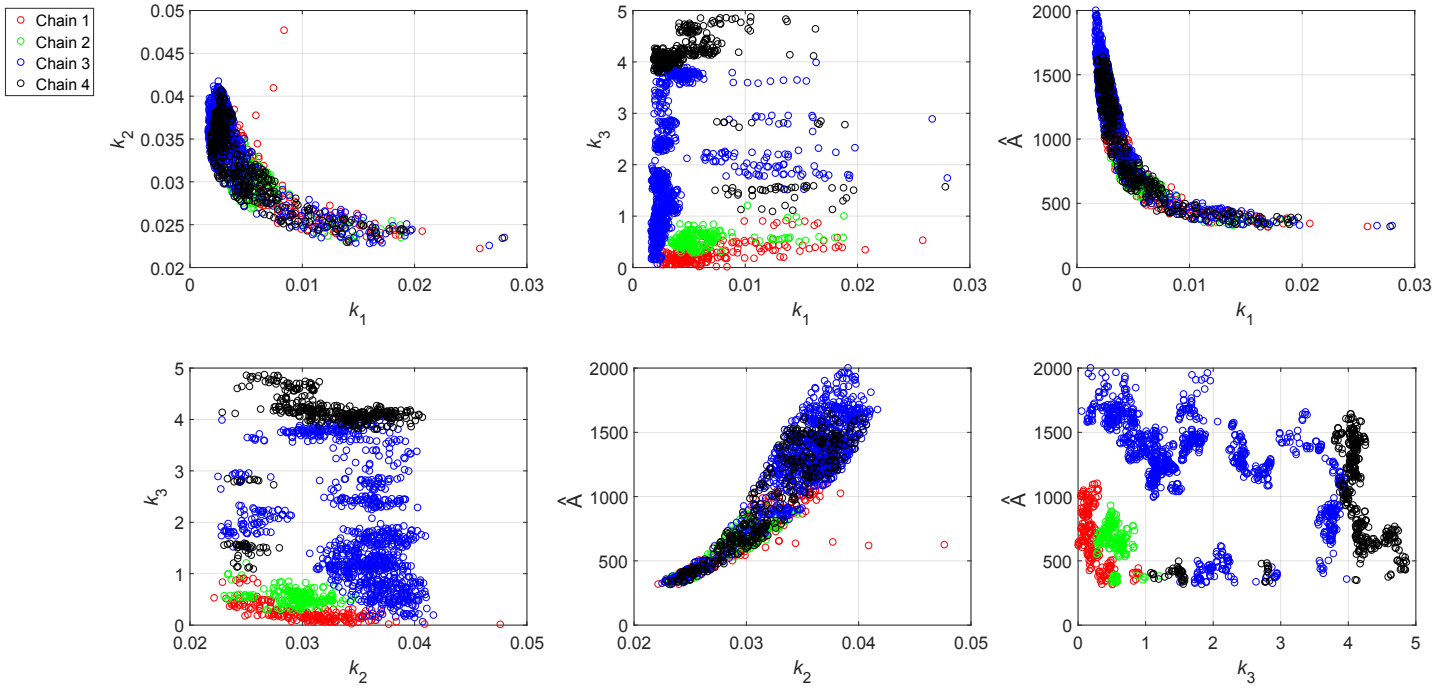

B

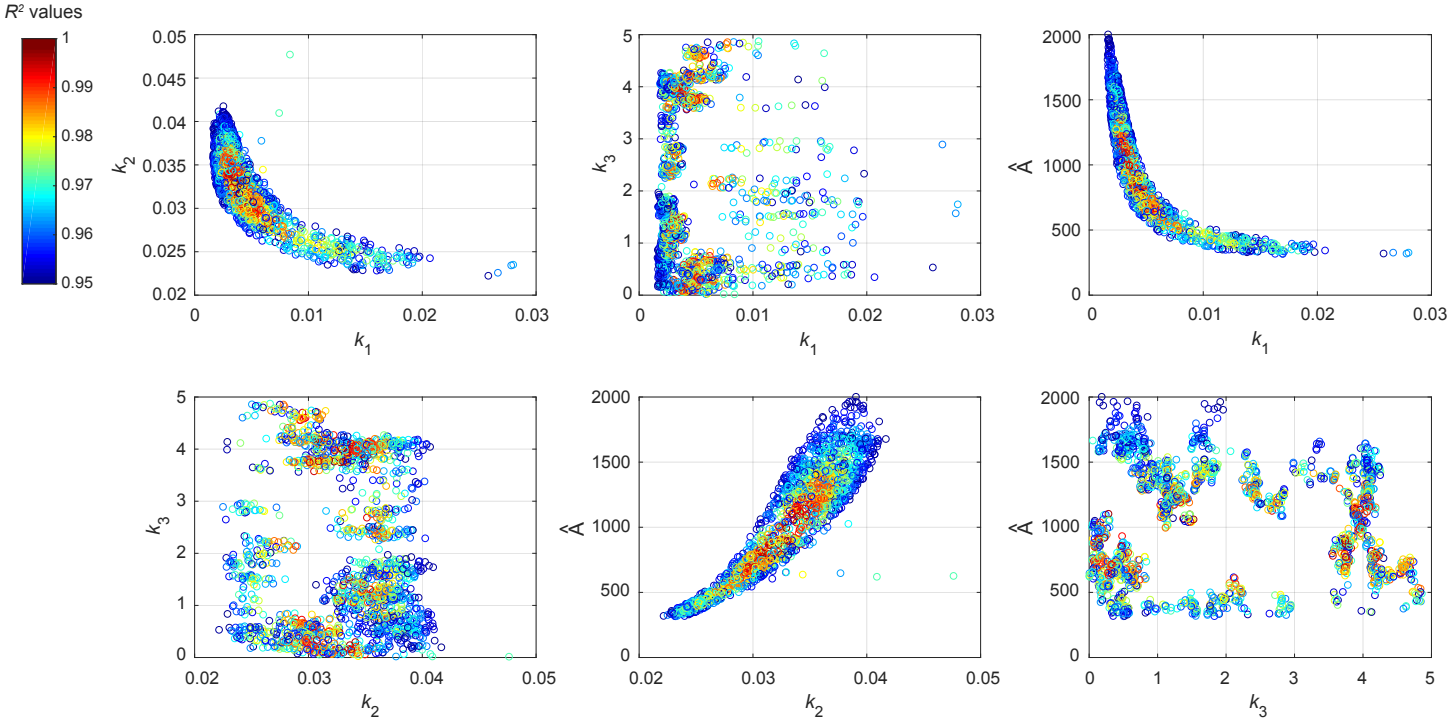

Figure S15. Monte Carlo simulations for the parameter space of the mathematical model.

(A) Scatter plots show the results of four Markov chain Monte Carlo simulations (shown in different colours, as indicated). The six two-dimensional projections of the four-dimensional parameter space shown here show only those points that allowed the model to fit the data well (R^2>0.95). **(B)** Scatter plots show the same data points as (A), but heat-mapped to show the R^2 value of each point. As in (A), only the data points with R^2>0.95 are shown. Points with a low R^2 value are shown in cool colours, while points with a high R^2 value are shown in warm colours (for the definition of parameters, see *Mathematical modelling* section in *Materials and Methods*). These results indicate that the parameter values that allow the model to fit the data are likely to occupy a single, continuous region of the parameter space.

Figure S16

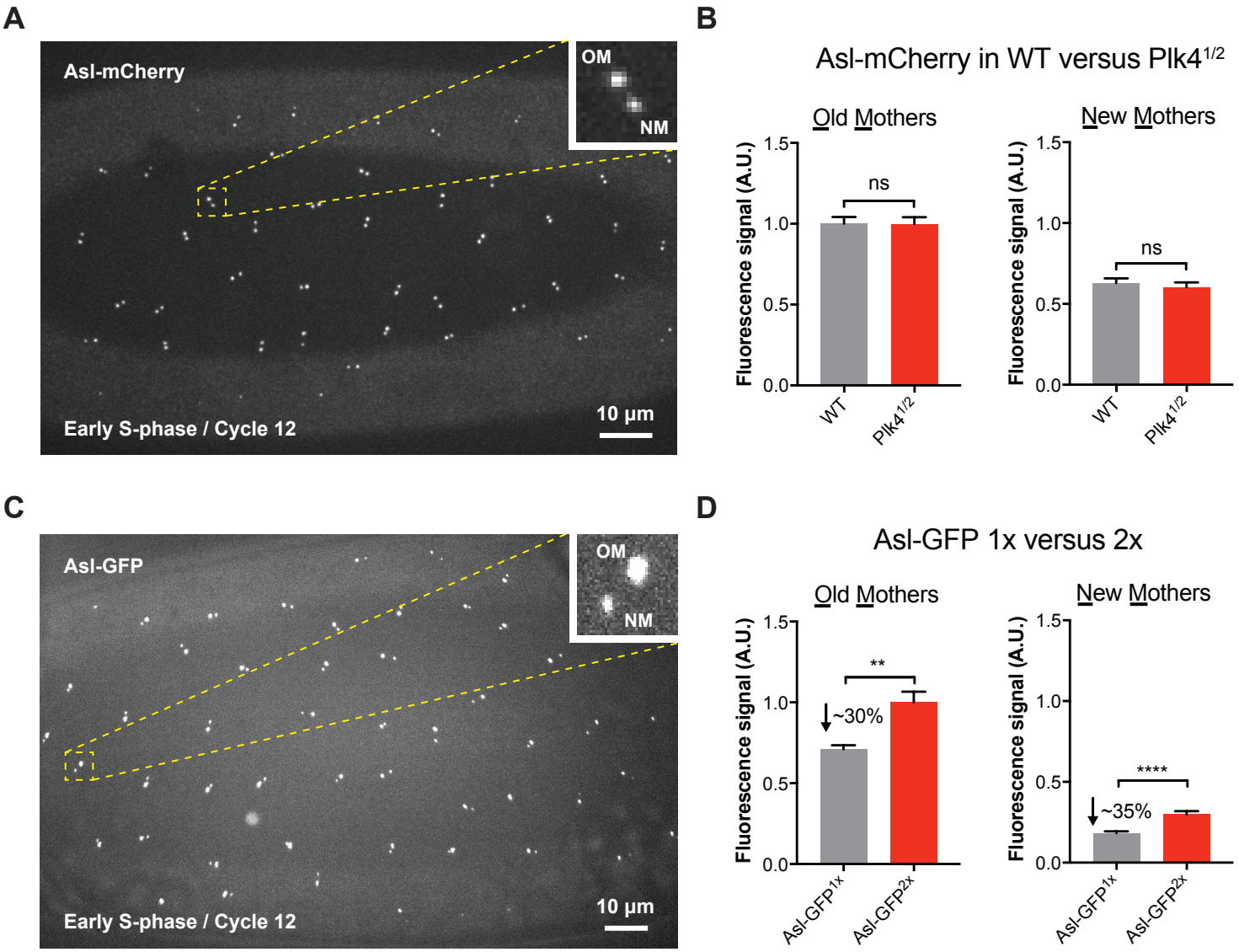

Figure S16. Quantification of Asl and Plk4 levels under various genetic conditions.

(A) Micrograph shows an image of Asl-mCherry at centrioles in an embryo in early S-phase (just after centrosome separation). More Asl is present on the older mother centriole (OM) than the new mother centriole (NM), as shown previously [5]. **(B)** Bar charts quantify the centriolar Asl-mCherry levels at OM and NM centrioles in early S-phase in either WT embryos (WT) or in embryos where the genetic dose of *Plk4* has been halved (*Plk4*$^{1/2}$). N=17 embryos for each condition; n=67 and 58 centrioles (mean) per embryo in WT or *Plk4*$^{1/2}$ groups, respectively. This analysis reveals that centriolar Asl levels do not change significantly when the genetic dosage of *Plk4* is halved, in good agreement with the prediction of our model. **(C and D)** Same schema as (A and B), but showing the localisation of Asl-GFP, and quantifying the centriolar levels of Asl-GFP in *asl* mutant embryos expressing either 1 (Asl-GFP^{1x}) or 2 (Asl-GFP^{2x}) copies of Asl-GFP. N=10 embryos for each condition; n=59 and 54 centrioles (mean) per embryo in Asl-GFP^{1x} or Asl-GFP^{2x} groups, respectively**.** This analysis reveals that centriolar Asl-GFP levels drop by ~30-35% when the genetic dosage of *Asl-GFP* is halved, in good agreement with the prediction of our model. Data are represented as Mean±SEM. Statistical significance was assessed using an unpaired *t* test with Welch's correction (for Gaussian-distributed data) or an unpaired Mann-Whitney test was used (**, P<0.01; ****, P<0.0001; ns, not significant). **(E)** Western blot compares the protein levels of Plk4-GFP (*arrow*) (expressed under the control of its own promoter in a *Plk4* mutant background) in otherwise WT embryos or embryos in which the genetic dosage of *asl* has been halved. This analysis reveals that Plk4-GFP levels in the embryo do not change dramatically when the genetic dosage of *asl* is halved, in agreement with the prediction of our model. WT embryos (Lane 1) are shown as a negative control to demonstrate that the Plk4-GFP band is only detected in embryos expressing Plk4-GFP. Prominent non-specific bands are indicated (*). Actin is shown as a loading control. A representative blot is shown from two technical repeats.

Figure S17

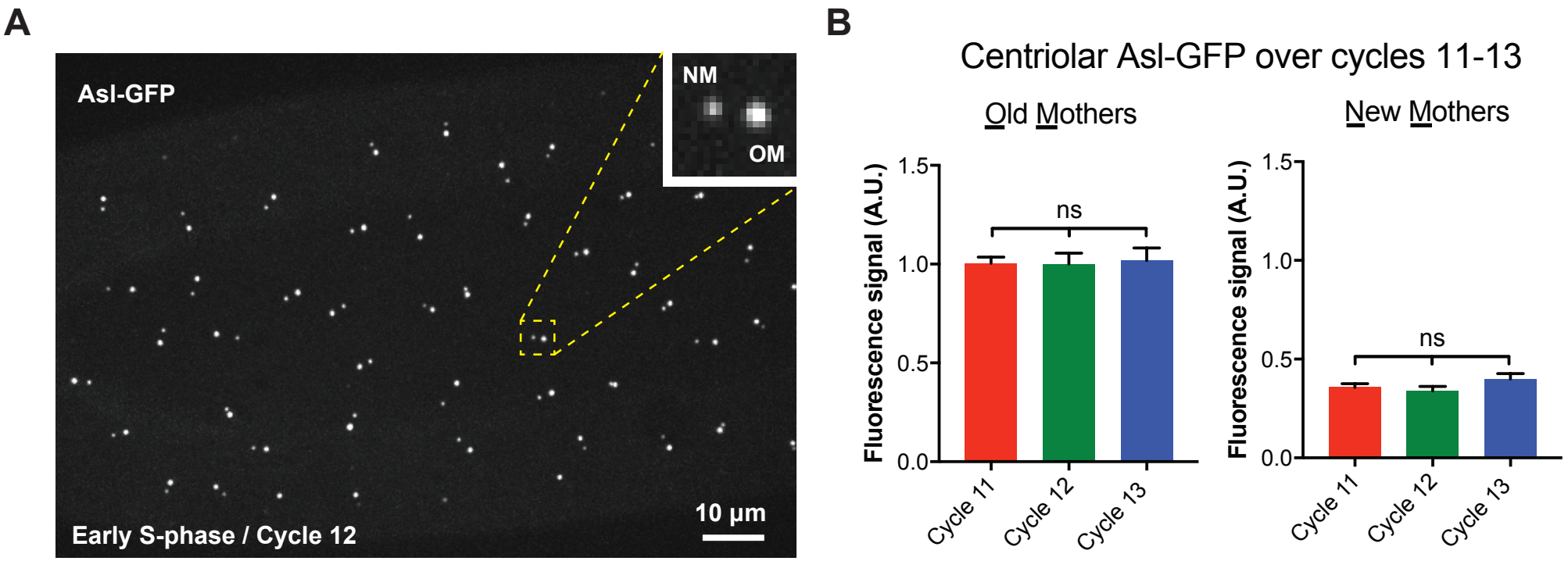
A
Asl-GFP
NM
OM
10 µm
Early S-phase / Cycle 12
B
Centriolar Asl-GFP over cycles 11-13
Old Mothers
New Mothers
Fluorescence signal (A.U.)
1.5
1.0
0.5
0.0
ns
Cycle 11
Cycle 12
Cycle 13

Figure S17. Centriolar Asl-GFP levels remain unchanged over cycles 11-13.

(A) Micrograph shows an image of Asl-GFP (two copies of a transgene expressed from the endogenous promotor) at centrioles in an *asl* mutant embryo in early S-phase (just after centrosome separation). **(B)** Bar charts quantify the centriolar Asl-GFP levels at such embryos in early S-phase at cycles 11-13. This analysis reveals that centriolar Asl-GFP levels at the start of S-phase remain relatively constant over successive nuclear cycles, in agreement with the prediction of our model. N≥14 embryos for each cell cycle; n=48, 70, and 130 centrioles (mean) per embryo in cycle 11-13, respectively. Data are represented as Mean±SEM. Statistical significance was assessed using an ordinary one-way ANOVA test (for Gaussian-distributed data) or a Kruskal-Wallis test (ns, not significant).

Figure S18

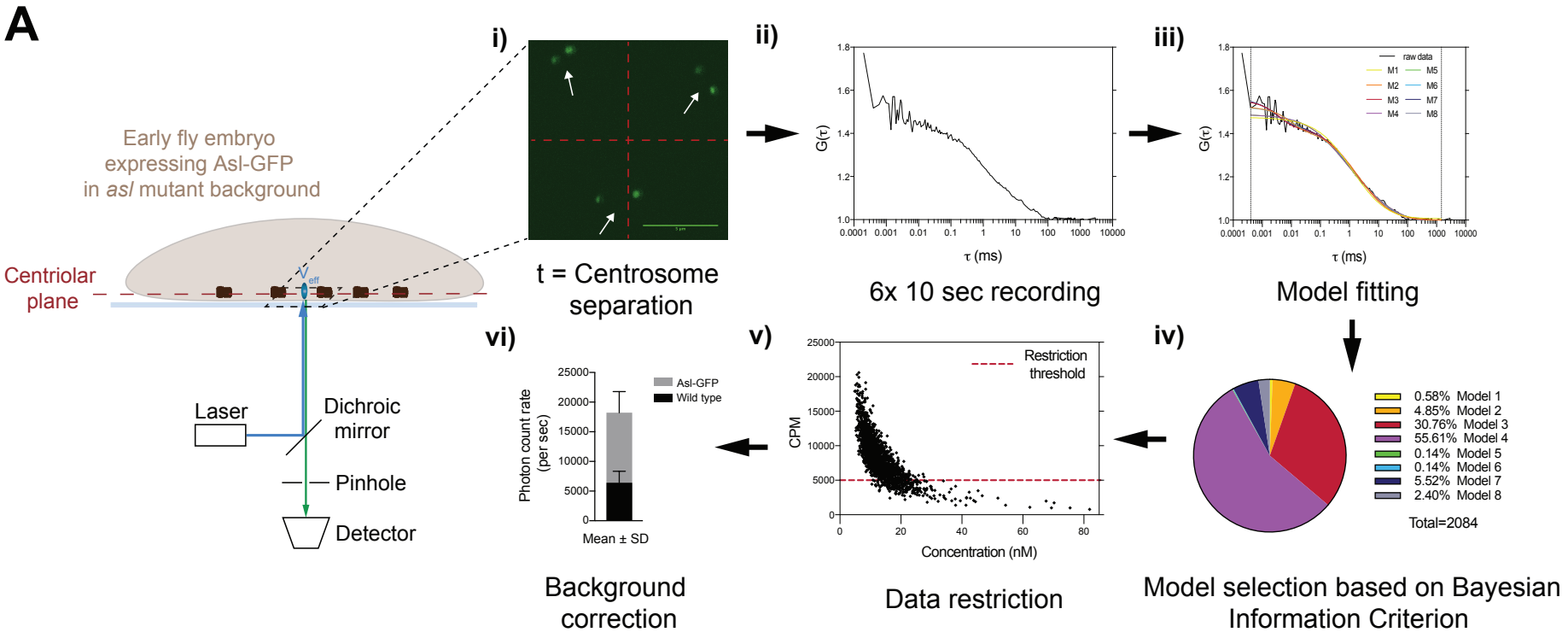
A
Early fly embryo
expressing Asl-GFP
in asl mutant background
Centriolar
plane
Laser
Dichroic
mirror
Pinhole
Detector
i)
t = Centrosome
separation
ii)
6x 10 sec recording
iii)
Model fitting
iv)
Model selection based on Bayesian
Information Criterion
0.58% Model 1
4.85% Model 2
30.76% Model 3
55.61% Model 4
0.14% Model 5
0.14% Model 6
5.52% Model 7
2.40% Model 8
Total=2084
v)
Data restriction
Restriction
threshold
CPM
Concentration (nM)
vi)
Background
correction
Photon count rate
(per sec)
Asl-GFP
Wild type
Mean ± SD

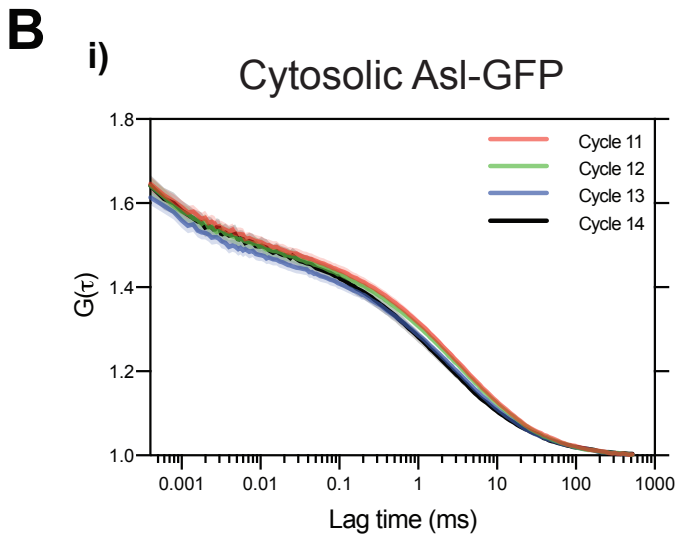
B
i)
Cytosolic Asl-GFP
Cycle 11
Cycle 12
Cycle 13
Cycle 14
G(τ)
Lag time (ms)

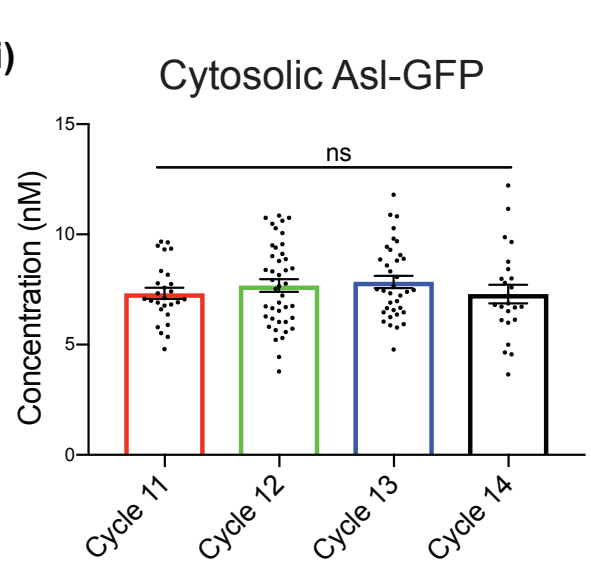
ii)
Cytosolic Asl-GFP
ns
Concentration (nM)
Cycle 11
Cycle 12
Cycle 13
Cycle 14

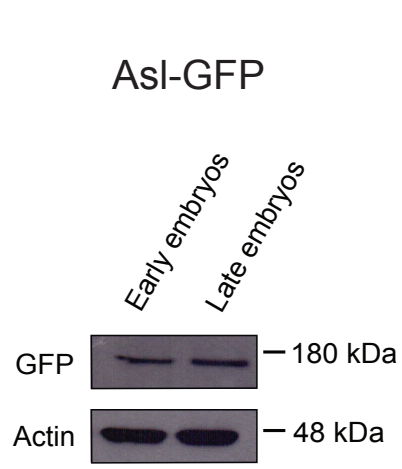
C
Asl-GFP
Early embryos
Late embryos
GFP
180 kDa
Actin
48 kDa

Figure S18. Cytoplasmic Asl-GFP levels remain unchanged over cycles 11-14.

(A) Schematic workflow describes the acquisition and analysis of point Fluorescence Correlation Spectroscopy (FCS) measurements. The 488nm laser beam is positioned at the centriolar plane in embryos expressing 2 copies of Asl-GFP (under the control of its own promoter in an *asl* mutant background). **(i)** At the beginning of every cycle, when the old and new mother centrioles are separating (*white* arrows), six 10 sec long FCS measurements were taken **(ii)**. **(iii)** In the FoCuS-point software, 8 different models were fitted to the autocorrelation functions (ACFs), and the model that describes the data the best was chosen based on the Bayesian information criterion **(iv)**. Post-regression data were restricted based on excluding measurements where the count-rate per molecule (CPM) was low **(v)**, and were then corrected for background noise **(vi)** (see *Materials and Methods* for further details). **(B) (i)** Graph shows the ACFs (represented as Mean±SEM) from all the embryos measured in cycles 11-14, prior to the background correction. Note that the height of the ACF is inversely proportional to the average number of particles in the excitation volume. **(ii)** Bar chart quantifies the FCS measurements after the background corrections. Statistical significance was assessed using an ordinary one-way ANOVA test (for Gaussian-distributed data) or a Kruskal-Wallis test (ns, not significant). Every data point represents the average of 4-6 recordings from each embryo measured. **(C)** Western blot shows the protein levels of the Asl-GFP in either the early or late cell cycles from embryos of the same genotype used in (A) and (B), as a secondary method to verify the results obtained from the FCS measurements. Early and late embryos were separated based on their distinct morphology (judged by eye under a dissection microscope). Actin is shown as a loading control. A representative blot is shown from two technical repeats.

Figure S19

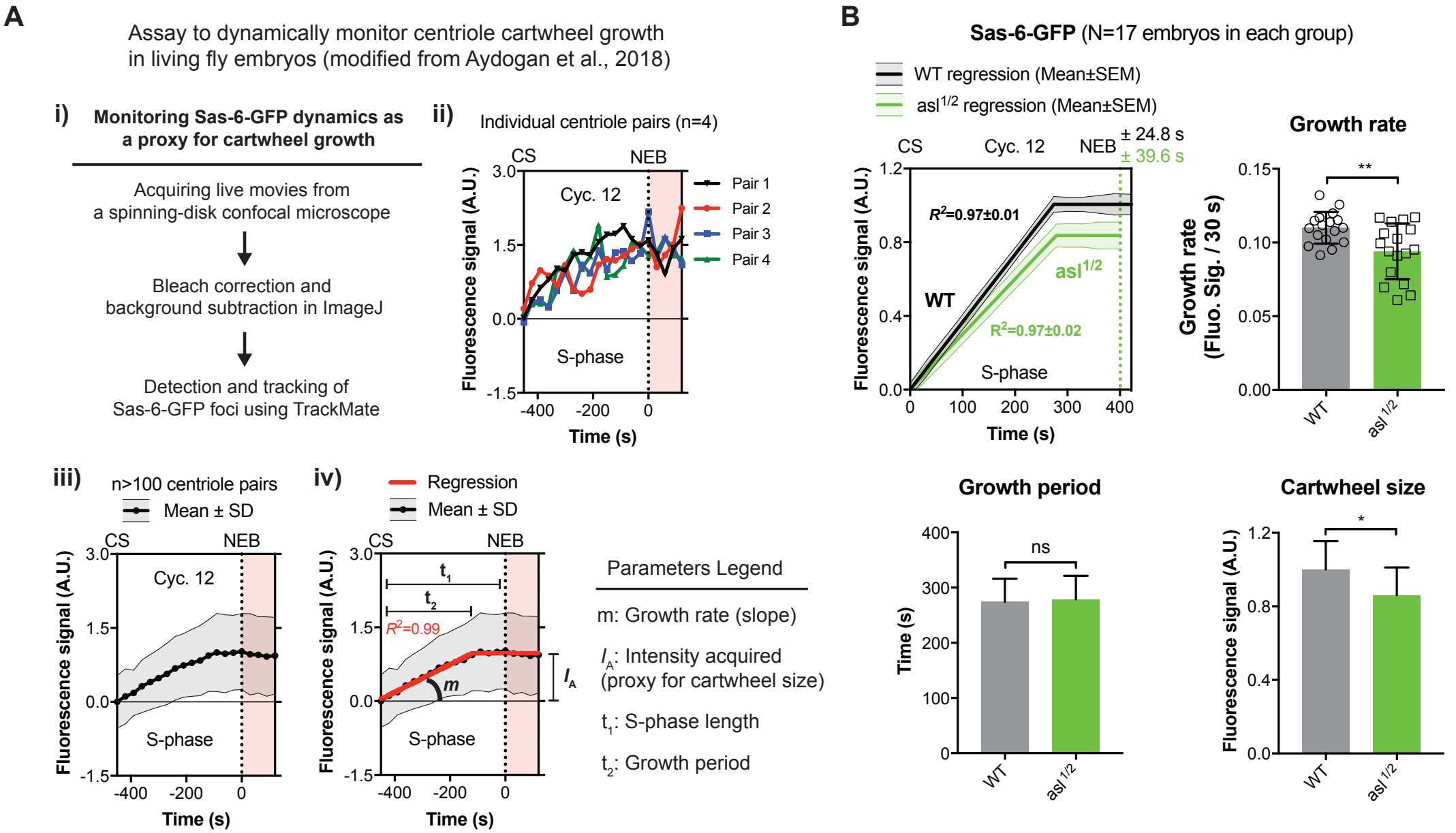
A
Assay to dynamically monitor centriole cartwheel growth
in living fly embryos (modified from Aydogan et al., 2018)
i) Monitoring Sas-6-GFP dynamics as a proxy for cartwheel growth
Acquiring live movies from a spinning-disk confocal microscope
Bleach correction and background subtraction in ImageJ
Detection and tracking of Sas-6-GFP foci using TrackMate
ii) Individual centriole pairs (n=4)
CS
NEB
Cyc. 12
S-phase
Pair 1
Pair 2
Pair 3
Pair 4
Fluorescence signal (A.U.)
Time (s)
iii) n>100 centriole pairs
Mean ± SD
iv) Regression
Mean ± SD
t_1
t_2
R^2=0.99
m
I_A
Parameters Legend
m: Growth rate (slope)
I_A: Intensity acquired (proxy for cartwheel size)
t_1: S-phase length
t_2: Growth period
B
Sas-6-GFP (N=17 embryos in each group)
WT regression (Mean±SEM)
asl1/2 regression (Mean±SEM)
± 24.8 s
± 39.6 s
R^2=0.97±0.01
R^2=0.97±0.02
WT
asl1/2
Growth rate
Growth rate (Fluo. Sig. / 30 s)
**
Growth period
ns
Time (s)
Cartwheel size
*
Fluorescence signal (A.U.)

Figure S19. Asterless levels influence the size of the centriole cartwheel. **(A)** Schematic summary of a previously published protocol to monitor centriole cartwheel growth in living fly embryos using Sas-6-GFP as a proxy for cartwheel elongation [4]. **(i)** Workflow describes the process of image acquisition, post-acquisition processing and the dynamic tracking of Sas-6-GFP. **(ii)** Graph shows the Sas-6-GFP fluorescence signal over time measured from 4 independent centriole-pair tracks during cycle 12. **(iii)** Graph shows the Sas-6-GFP fluorescence signal over time measured from >100 independent centriole pairs from the same embryo (Mean±SD). **(iv)** The growth profile in (iii) was mathematically regressed to extract the indicated growth parameters, as described previously in [4]. Pink shaded time domains indicate mitotic periods in the cell cycle. **(B)** Graphs compare the Sas-6-GFP incorporation profile during cycle 12 in WT embryos (WT; *grey*) or in embryos where the genetic dose of *asl* was halved ($asl^{1/2}$; *green*). Bar charts quantify and compare parameters of centriole growth. Halving the genetic dose of *asl* leads to a slowing of the cartwheel growth rate, but no change in the growth period, and so the cartwheel is ultimately too small. N=17 embryos for each condition; n=77 and 72 centrioles (mean) per embryo in WT or $asl^{1/2}$ groups, respectively**.** Bar charts are represented as Mean±SD. Statistical significance was assessed using an unpaired *t* test with Welch's correction (for Gaussian-distributed data) or an unpaired Mann-Whitney test was used (*, P<0.05; **, P<0.01; ns, not significant). CS=centrosome separation; NEB=nuclear envelope breakdown.

Figure S20

A

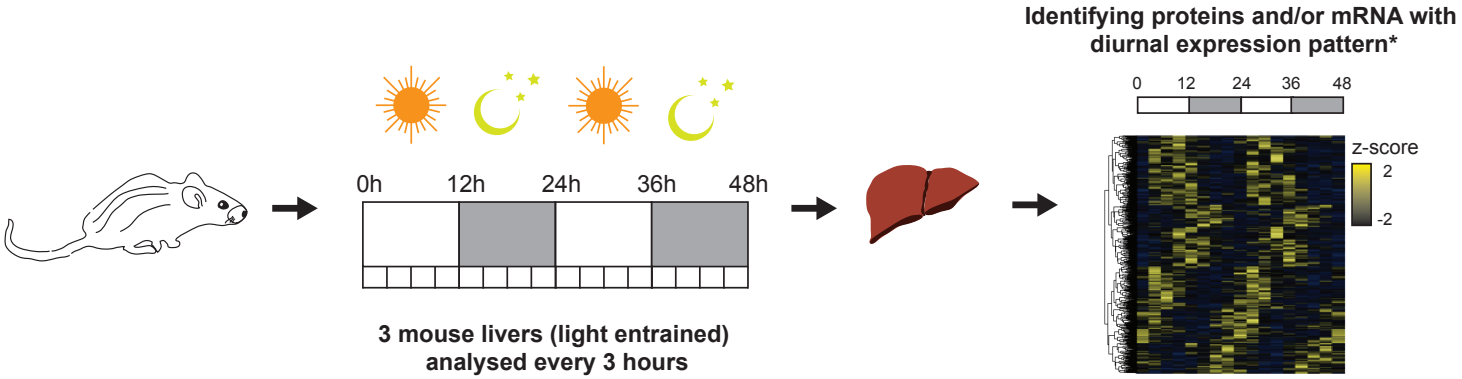

*Modified from Wang et al., 2018

B

Positive circadian clock controls (transcripts) showing the tissue was entrained to the light/dark cycles*

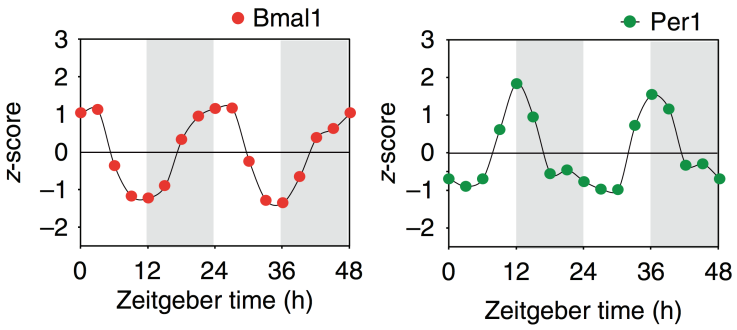

*Graphs above are taken from Wang et al., 2018

Data-mining from Supplementary Data 9 of Wang et al., 2018

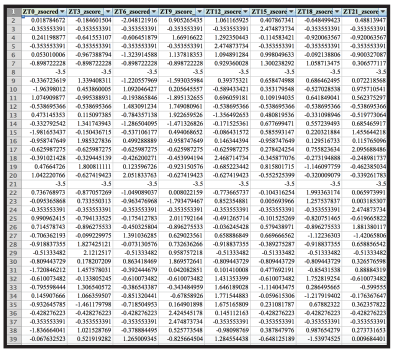

Supp. Data 9: Matrix of total 6,780 proteins identified in the whole liver proteome during 2 circadian cycles over 48 hours

C

Data-mining results: Change in protein amount over 48 hours

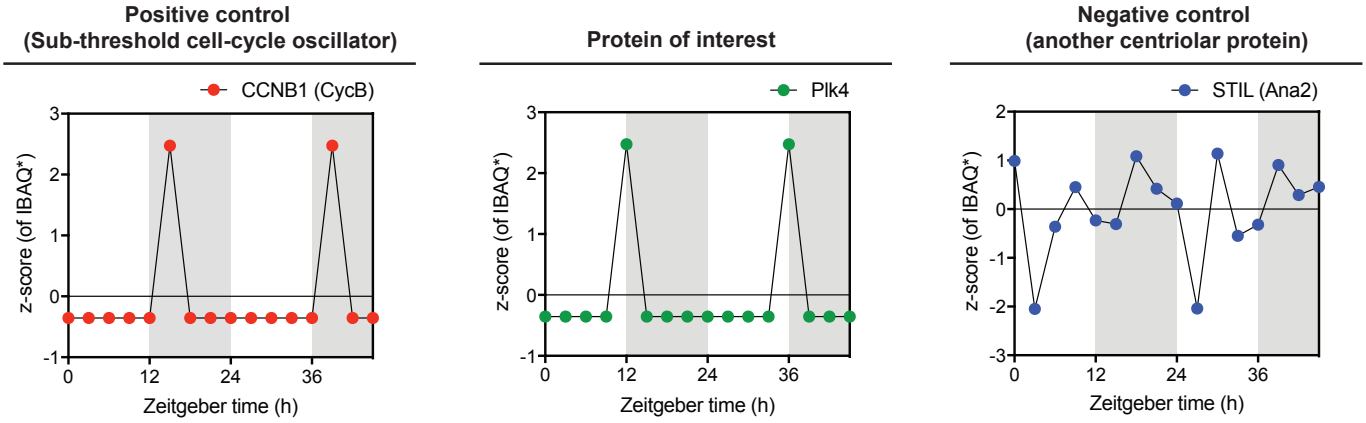

***IBAQ:** Intensity-based absolute protein quantification

Figure S20. Plk4 may also form a free running oscillator in mammals that, like the cell cycle oscillator, can be entrained by the circadian clock.

(A) Cartoon shows the workflow used by Wang et al. to obtain a diurnal proteome of the whole liver of light/dark-entrained mice [25]. **(B)** Graphs reproduced from Wang et al. (2018), show the relative diurnal expression of the circadian clock transcripts Bmal1 and Per1 as an internal control. We analysed the diurnal proteome produced in this study (comprising a matrix of z-scores for 6,780 proteins identified during 2 circadian cycles over 48h—Supplementary Data set #9). **(C)** Graphs show the relative protein levels of Cyclin B (CCNB1 in mammalians), Plk4 and the cartwheel component STIL (Ana2 in flies) over the two 24hr periods. Although these liver cells are generally not proliferating, Cyclin B levels oscillate and spike strongly during evening times, consistent with previous reports that the core Cdk/Cyclin cell cycle oscillator (CCO) can continue to oscillate (at levels that do not trigger mitosis) in non-dividing cells [26] and also is strongly entrained by the circadian clock [27,28]. Remarkably, our analysis reveals that Plk4 levels strongly spike at 12 and 36 hrs (just before the Cyclin B levels peak). As these cells are not proliferating, centrioles should not be duplicating in these cells, so these oscillations are presumably sub-threshold for duplication. These observations suggest that both Plk4 and Cyclin B levels naturally oscillate in these quiescent liver cells, and the period of their oscillations is tightly entrained by the circadian clock. In contrast, protein levels of STIL/Ana2, a core component of the centriole cartwheel that interacts with Plk4, does not show any discernible pattern of oscillation or entrainment to the circadian clock. We speculate, therefore, that Plk4 forms a free-running oscillator also in non-dividing mammalian cells, and that this oscillator is likely to be entrained by both the cell cycle and circadian clocks.

Supplementary Tables

Table S1: The best-fit k_1, k_2, k_3, and $\widehat{A}$ parameter values* for cycles 11-13 (Fig. 4C).

Parameters	Cycle 11	Cycle 12	Cycle 13
k_1	0.004762	0.003644	0.001272
k_2	0.03756	0.03443	0.02164
k_3	0.06906	0.06906	0.06906
$\widehat{A}$	1012	940	1030
$\widehat{A}_0$	701	637	557
A_{tot}	1713	1577	1587
R^2	0.998	0.9996	0.998

*For the definition of parameters, see *Materials and Methods* under Mathematical modeling and Monte Carlo simulations.

Table S2: The best-fit k_1, k_2, k_3, and $\widehat{A}$ parameter values* for the Plk4$^{1/2}$ experiment (Fig. 4D).

Parameters	Control	Plk4$^{1/2}$
k_1	0.003862	0.001513
k_2	0.03699	0.02767
k_3	0.06906	0.06906
$\widehat{A}$	4884	5607
$\widehat{A}_0$	3152	2390
A_{tot}	8036	7997
R^2	0.9992	0.996

*For the definition of parameters, see *Materials and Methods* under Mathematical modeling and Monte Carlo simulations.

Table S3: The best-fit k_1, k_2, k_3, and $\widehat{A}$ parameter values* for the *asl*$^{1/2}$ experiment (Fig. 4E).

Parameters	Control	asl$^{1/2}$
k_1	0.003437	0.002724
k_2	0.03246	0.03324
k_3	0.06906	0.06906
$\widehat{A}$	1938	1408
$\widehat{A}_0$	1298	950
A_{tot}	3236	2358
R^2	0.9996	0.9991

*For the definition of parameters, see *Materials and Methods* under Mathematical modeling and Monte Carlo simulations.

Table S4: *D. melanogaster* alleles used in this study.

Allele*	Source (reference #)	ID
Plk4-mNeonGreen	This paper	N/A
$Plk4^{Aa74}$ (Plk4 null mutant)	[4]	N/A
Asl-mKate2	This paper	N/A
Sas-6-mCherry	[29]	N/A
$CycB^{2}$	[30]	FlyBase ID: Fbal0094855
grp^{fsA4}	[31]	FlyBase ID: Fbal0062815
Asl-mCherry	[32]	N/A
Asl-GFP	[33]	FlyBase ID: FBtp0040947
asl^{B46}	[34]	N/A
Sas-6-GFP	[4]	N/A

*The alleles listed here were all expressed under their endogenous promoters.

Table S5: *D. melanogaster* strains generated and/or used in this study.

Strain Genotype	Tissue	Type of experiment
Plk4-mNeonGreen, $Plk4^{Aa74}$ / Plk4-mNeonGreen, $Plk4^{Aa74}$	Embryo	Confocal Microscopy; Drug injections
Asl-mKate2 / Cyo; Plk4-mNeonGreen, $Plk4^{Aa74}$ / Plk4-mNeonGreen, $Plk4^{Aa74}$	Embryo	3D Structured Illumination Microscopy
Sas-6-mCherry / +; Plk4-mNeonGreen, $Plk4^{Aa74}$ / Plk4-mNeonGreen, $Plk4^{Aa74}$	Embryo	Confocal Microscopy
$CycB^{2}$ / +; Plk4-mNeonGreen, $Plk4^{Aa74}$ / Plk4-mNeonGreen, $Plk4^{Aa74}$	Embryo	Confocal Microscopy
grp^{fsA4} / +; Plk4-mNeonGreen, $Plk4^{Aa74}$ / Plk4-mNeonGreen, $Plk4^{Aa74}$	Embryo	Confocal Microscopy
Oregon-R (Wild-type strain)	Embryo	Western Blot; Fluorescence Correlation Spectroscopy
Plk4-mNeonGreen, $Plk4^{Aa74}$ / $Plk4^{Aa74}$	Embryo	Confocal Microscopy
Asl-mCherry / +	Embryo	Confocal Microscopy
Asl-mCherry / +; $Plk4^{Aa74}$ / +	Embryo	Confocal Microscopy
Plk4-mNeonGreen / +; Plk4-mNeonGreen, $Plk4^{Aa74}$ / $Plk4^{Aa74}$	Embryo	Confocal Microscopy
Plk4-mNeonGreen / +; Plk4-mNeonGreen, $Plk4^{Aa74}$ / asl^{B46}, $Plk4^{Aa74}$	Embryo	Confocal Microscopy
Asl-GFP / Asl-GFP; asl^{B46} / asl^{B46}	Embryo	Confocal Microscopy; Fluorescence Correlation Spectroscopy; Western Blot
Asl-GFP / +; asl^{B46} / asl^{B46}	Embryo	Confocal Microscopy
Sas-6-GFP / +	Embryo	Confocal Microscopy
Sas-6-GFP / +; asl^{B46} / +	Embryo	Confocal Microscopy

Table S6: Oligonucleotides used in this study.

Oligonucleotide name	Sequence	Source
Primer to introduce the NheI restriction enzyme sites into the mCherry C-terminal Gateway vector: **Forward**	GTTCGATATCCAGCACAGTGGCGGCCGCTCGAGGCTAGCATGGTGAGCAAGGGCGAGGAGGATAACATGGCCATC	Invitrogen, Thermo Fisher Scientific
Primer to introduce the NheI restriction enzyme sites into the mCherry C-terminal Gateway vector: **Reverse**	GATGGCCATGTTATCCTCCTCGCCCTTGCTCACCATGCTAGCCTCGAGCGGCCGCCACTGTGCTGGATATCGAAC	Invitrogen, Thermo Fisher Scientific
Primer to replace rhe mCherry tag with mNeonGreen by homologous recombination on the destination vector: **Forward**	CAGTGGCGGCCGCTCGAGGCTAGCATGGTGAGCAAGGGCGAGGAGGATAAC	Invitrogen, Thermo Fisher Scientific
Primer to replace rhe mCherry tag with mNeonGreen by homologous recombination on the destination vector: **Reverse**	GATGGGCATGGACGAGCTGTACAAGTAACCGCGGTGGCGGCCGCTCTAG	Invitrogen, Thermo Fisher Scientific
Primer to replace rhe mCherry tag with mKate2 by homologous recombination on the destination vector: **Forward**	GTGGCGGCCGCTCGAGGCTAGCATGGTGAGCGAGCTGATTAAGGAGAAC	Invitrogen, Thermo Fisher Scientific
Primer to replace rhe mCherry tag with mKate2 by homologous recombination on the destination vector: **Reverse**	GTTCTAGAGCGGCCGCCACCGCGGTCATCTGTGCCCCAGTTTGCTAG	Invitrogen, Thermo Fisher Scientific

Table S6 Cont'd: Oligonucleotides used in this study.

Oligonucleotide name	Sequence	Source
Primer to remove the NheI restriction enzyme sites from the destination vector via site-directed mutagenesis (mNeonGreen vector): **Forward**	GATATCCAGCACAGTGGCGGCCGCTCGAGATGGTGAGCAAGGGCGAGGAGGATAACATGG	Invitrogen, Thermo Fisher Scientific
Primer to remove the NheI restriction enzyme sites from the destination vector via site-directed mutagenesis (mNeonGreen vector): **Reverse**	CCATGTTATCCTCCTCGCCCTTGCTCACCATCTCGAGCGGCCGCCACTGTGCTGGATATC	Invitrogen, Thermo Fisher Scientific
Primer to remove the NheI restriction enzyme sites from the destination vector via site-directed mutagenesis (mKate2 vector): **Forward**	GTTCGATATCCAGCACAGTGGCGGCCGCTCGAGATGGTGAGCGAGCTGATTAAGGAGAACATGC	Invitrogen, Thermo Fisher Scientific
Primer to remove the NheI restriction enzyme sites from the destination vector via site-directed mutagenesis (mKate2 vector): **Reverse**	GCATGTTCTCCTTAATCAGCTCGCTCACCATCTCGAGCGGCCGCCACTGTGCTGGATATCGAAC	Invitrogen, Thermo Fisher Scientific
Primer to amplify Cyclin A: **Forward**	TACAATTGCAAGCAGAAAGAGG	Invitrogen, Thermo Fisher Scientific
Primer to amplify Cyclin A: **Reverse**	GGAGTTCACAGAACATTTACGG	Invitrogen, Thermo Fisher Scientific
Primer to amplify Cyclin B: **Forward**	TAATTCTTGGAGAGACAACGCC	Invitrogen, Thermo Fisher Scientific
Primer to amplify Cyclin B: **Reverse**	CTACAACAAGTACCAGGGCAGC	Invitrogen, Thermo Fisher Scientific

Table S6 Cont'd: Oligonucleotides used in this study.

Oligonucleotide name	Sequence	Source
Primer to amplify Cyclin B3: **Forward**	GAACGAAATATTGGC GTAATCC	Invitrogen, Thermo Fisher Scientific
Primer to amplify Cyclin B3: **Reverse**	CGCCATGGATATATT CAACTACC	Invitrogen, Thermo Fisher Scientific

Table S7: Starting parameter values and proposal acceptance rates for each of four Markov chains used in Metropolis-Hastings Markov chain Monte Carlo.

Parameters	Chain 1	Chain 2	Chain 3	Chain 4
k_1	0.0035	0.01	0.1	0.0035
k_2	0.035	0.09	0.2	0.035
k_3	0.05	0.5	0.1	4
$\widehat{A}$	1000	500	1500	1500
Acceptance	36%	36%	29%	37%

Supplementary Movie Captions

Movie S1. Monitoring Plk4-NG oscillations in a *Drosophila* embryo.
Time-lapse movie of an embryo expressing two copies of Plk4-NG (expressed transgenically from the endogenous *Plk4* promoter) in a *Plk4* mutant background, observed on a spinning-disk confocal microscope through nuclear cycles 11-13. The movie is a maximum-intensity projection that has been photo-bleach corrected, but not background subtracted for visual clarity. Time (min:sec) is shown at the top left, and stage of the cell cycle is indicated at the bottom left.

Movie S2. Monitoring Sas-6-mCherry incorporation and Plk4-NG oscillations simultaneously in the same embryo.
Time-lapse movie of an embryo expressing one copy of Sas-6-mCherry (expressed transgenically from the endogenous *Sas-6* promotor) and two copies of Plk4-NG (expressed transgenically from the endogenous *Plk4* promoter) in a *Plk4* mutant background, observed on a spinning-disk confocal microscope during S-phase of nuclear cycle 12. The movie is a maximum-intensity projection that has been photo-bleach corrected, but not background subtracted for visual clarity. Time (Min:Sec) is shown at the top left, and stage of the cell cycle is indicated at the bottom left.

Movie S3. Plk4-NG oscillations continue in "late" embryos arrested in interphase by mitotic cyclin depletion.
Time-lapse movie of an embryo expressing two copies of Plk4-NG (expressed transgenically from the endogenous *Plk4* promoter) in a *Plk4* mutant background, observed on a spinning-disk confocal microscope through nuclear cycle 12. The embryo was injected with cyclin A-B-B3 dsRNA in ~cycle 8, approximately 30-40 min prior to the start of the movie. The movie on the left is the maximum intensity projection of the slices where centrioles are in focus. The movie on the right is the maximum intensity projection of the slices where nuclei are in focus. Note how the centrioles undergo at least two rounds of duplication, the second of which is more asynchronous and occurs without nuclear envelope breakdown (indicating that the nuclei are arrested in an interphase-like state). These videos have been photo-bleach corrected, but not background subtracted for visual clarity. Time (Min:Sec) is shown at the top left.

Movie S4. Plk4-NG oscillations continue on stochastically duplicating centrioles in "early" embryos arrested in interphase by mitotic cyclin depletion.
Time-lapse movie of an embryo expressing two copies of Plk4-NG (expressed transgenically from the endogenous *Plk4* promoter) in a *Plk4* mutant background, observed on a spinning-disk confocal microscope. The embryo was injected with cyclin A-B-B3 dsRNA in ~cycle 2-4, approximately 90 min prior to the start of the movie. The movie on the left is the maximum intensity projection of the slices where centrioles are in focus. The movie on the right is the maximum intensity projection of the slices where nuclei are in focus. Note that a small number of large nuclei are present throughout the time-course of the movie (indicating that they are arrested in an interphase-like state), but

some centrioles duplicate one or more times in an apparently stochastic manner. The Plk4-NG oscillations on individual centrioles are less obvious than in normally cycling embryos, but an unbiased computational analysis of these movies indicates that individual centriole duplication events are correlated with individual centriolar Plk4-NG oscillations (Fig. S9). These videos have been photo-bleach corrected, but not background subtracted for visual clarity. Time (Min:Sec) is shown at the top left.

Movie S5. Plk4-NG oscillations continue after colchicine injection, but with a strongly reduced amplitude.
Time-lapse movie of an embryo expressing two copies of Plk4-NG (expressed transgenically from the endogenous *Plk4* promoter) in a *Plk4* mutant background, observed on a spinning-disk confocal microscope through nuclear cycle 12. The embryo was injected with colchicine in mitosis of nuclear cycle 11, approximately 30 sec prior to the start of the movie. The movie is a maximum-intensity projection that has been photo-bleach corrected, but not background subtracted for visual clarity. Time (Min:Sec) is shown at the top left, and stage of the cell cycle is indicated at the bottom left.

Movie S6. Plk4-NG oscillations are blocked after cycloheximide injection.
Time-lapse movie of an embryo expressing two copies of Plk4-NG (expressed transgenically from the endogenous *Plk4* promoter) in a *Plk4* mutant background, observed on a spinning-disk confocal microscope through nuclear cycle 12. The embryo was injected with cycloheximide in mitosis of nuclear cycle 11, approximately 30 sec prior to the start of the movie. The movie is a maximum-intensity projection that has been photo-bleach corrected, but not background subtracted for visual clarity. Time (Min:Sec) is shown at the top left, and stage of the cell cycle is indicated at the bottom left.

References

1. Basto, R., Brunk, K., Vinadogrova, T., Peel, N., Franz, A., Khodjakov, A. & Raff, J. W. Centrosome amplification can initiate tumorigenesis in flies. *Cell* **133,** 1032–1042 (2008).
2. Shaner, N. C., Lambert, G. G., Chammas, A., Ni, Y., Cranfill, P. J., Baird, M. A., Sell, B. R., Allen, J. R., Day, R. N., Israelsson, M., Davidson, M. W. & Wang, J. A bright monomeric green fluorescent protein derived from Branchiostoma lanceolatum. *Nat Methods* **10,** 407–409 (2013).
3. Shcherbo, D., Murphy, C. S., Ermakova, G. V., Solovieva, E. A., Chepurnykh, T. V., Shcheglov, A. S., Verkhusha, V. V., Pletnev, V. Z., Hazelwood, K. L., Roche, P. M., Lukyanov, S., Zaraisky, A. G., Davidson, M. W. & Chudakov, D. M. Far-red fluorescent tags for protein imaging in living tissues. *Biochem. J.* **418,** 567–574 (2009).
4. Aydogan, M. G., Wainman, A., Saurya, S., Steinacker, T. L., Caballe, A., Novak, Z. A., Baumbach, J., Muschalik, N. & Raff, J. W. A homeostatic clock sets daughter centriole size in flies. *J Cell Biol* **217,** 1233–1248 (2018).
5. Novak, Z. A., Conduit, P. T., Wainman, A. & Raff, J. W. Asterless licenses daughter centrioles to duplicate for the first time in Drosophila embryos. *Curr. Biol.* **24,** 1276–1282 (2014).
6. Raff, J. W. & Glover, D. M. Centrosomes, and not nuclei, initiate pole cell formation in Drosophila embryos. *Cell* **57,** 611–619 (1989).
7. Edgar, B. A., Kiehle, C. P. & Schubiger, G. Cell cycle control by the nucleo-cytoplasmic ratio in early Drosophila development. *Cell* **44,** 365–372 (1986).
8. McCleland, M. L. & O'Farrell, P. H. RNAi of Mitotic Cyclins in Drosophila Uncouples the Nuclear and Centrosome Cycle. *Curr. Biol* **18,** 245–254 (2008).
9. Lehmann, V., Müller, H. & Lange, B. M. H. Immunoisolation of centrosomes from Drosophila melanogaster. *Curr Protoc Cell Biol* **Chapter 3,** Unit 3.17 (2006).
10. Conduit, P. T., Feng, Z., Richens, J. H., Baumbach, J., Wainman, A., Bakshi, S. D., Dobbelaere, J., Johnson, S., Lea, S. M. & Raff, J. W. The centrosome-specific phosphorylation of Cnn by Polo/Plk1 drives Cnn scaffold assembly and centrosome maturation. *Dev Cell* **28,** 659–669 (2014).
11. Conduit, P. T., Brunk, K., Dobbelaere, J., Dix, C. I., Lucas, E. P. & Raff, J. W. Centrioles regulate centrosome size by controlling the rate of Cnn incorporation into the PCM. **20,** 2178–2186 (2010).
12. Raff, J. W., Kellogg, D. R. & Alberts, B. M. Drosophila gamma-tubulin is part of a complex containing two previously identified centrosomal MAPs. *J Cell Biol* **121,** 823–835 (1993).
13. Tinevez, J.-Y., Perry, N., Schindelin, J., Hoopes, G. M., Reynolds, G. D., Laplantine, E., Bednarek, S. Y., Shorte, S. L. & Eliceiri, K. W. TrackMate: An open and extensible platform for single-particle tracking. *Methods* **115,** 80–90 (2016).
14. Alvarez Rodrigo, I., Conduit, P. T., Baumbach, J., Novak, Z. A., Aydogan, M. G., Wainman, A. & Raff, J. W. A positive feedback loop

drives centrosome maturation in flies. 380907 (2018). doi:10.1101/380907

15. Raff, J. W., Whitfield, W. G. & Glover, D. M. Two distinct mechanisms localise cyclin B transcripts in syncytial Drosophila embryos. *Development* **110,** 1249–1261 (1990).
16. Raff, J. W. & Glover, D. M. Nuclear and cytoplasmic mitotic cycles continue in Drosophila embryos in which DNA synthesis is inhibited with aphidicolin. *J Cell Biol* **107,** 2009–2019 (1988).
17. Ball, G., Demmerle, J., Kaufmann, R., Davis, I., Dobbie, I. M. & Schermelleh, L. SIMcheck: a Toolbox for Successful Super-resolution Structured Illumination Microscopy. *Sci Rep* **5,** 15915 (2015).
18. Rüttinger, S., BUSCHMANN, V., KRÄMER, B., ERDMANN, R., MACDONALD, R. & KOBERLING, F. Comparison and accuracy of methods to determine the confocal volume for quantitative fluorescence correlation spectroscopy. *J Microsc* **232,** 343–352 (2008).
19. Petrášek, Z. & Schwille, P. Precise Measurement of Diffusion Coefficients using Scanning Fluorescence Correlation Spectroscopy. *Biophys J* **94,** 1437–1448 (2008).
20. Waithe, D., Clausen, M. P., Sezgin, E. & Eggeling, C. FoCuS-point: software for STED fluorescence correlation and time-gated single photon counting. *Bioinformatics* **32,** 958–960 (2016).
21. Schönle, A., Middendorff, Von, C., Ringemann, C., Hell, S. W. & Eggeling, C. Monitoring triplet state dynamics with fluorescence correlation spectroscopy: bias and correction. *Microsc Res Tech* **77,** 528–536 (2014).
22. Schwarz, G. Estimating the Dimension of a Model. *The Annals of Statistics* **6,** 461–464 (1978).
23. Koppel, D. E. Statistical accuracy in fluorescence correlation spectroscopy. *Physical Review A* **10,** 1938–1945 (1974).
24. Klebba, J. E., Galletta, B. J., Nye, J., Plevock, K. M., Buster, D. W., Hollingsworth, N. A., Slep, K. C., Rusan, N. M. & Rogers, G. C. Two Polo-like kinase 4 binding domains in Asterless perform distinct roles in regulating kinase stability. *J Cell Biol* **208,** 401–414 (2015).
25. Wang, Y., Song, L., Liu, M., Ge, R., Zhou, Q., Liu, W., Li, R., Qie, J., Zhen, B., Wang, Y., He, F., Qin, J. & Ding, C. A proteomics landscape of circadian clock in mouse liver. *Nat Commun* **9,** 1553 (2018).
26. Jord, Al, A., Shihavuddin, A., Servignat d'Aout, R., Faucourt, M., Genovesio, A., Karaiskou, A., Sobczak-Thépot, J., Spassky, N. & Meunier, A. Calibrated mitotic oscillator drives motile ciliogenesis. *Science* **358,** 803–806 (2017).
27. Matsuo, T., Yamaguchi, S., Mitsui, S., Emi, A., Shimoda, F. & Okamura, H. Control mechanism of the circadian clock for timing of cell division in vivo. *Science* **302,** 255–259 (2003).
28. Yang, Q., Pando, B. F., Dong, G., Golden, S. S. & van Oudenaarden, A. Circadian gating of the cell cycle revealed in single cyanobacterial cells. *Science* **327,** 1522–1526 (2010).
29. Rogers, G. C., Rusan, N. M., Peifer, M. & Rogers, S. L. A multicomponent assembly pathway contributes to the formation of acentrosomal microtubule arrays in interphase Drosophila cells. *Mol Biol Cell* **19,** 3163–3178 (2008).

30. Jacobs, H. W., Knoblich, J. A. & Lehner, C. F. Drosophila Cyclin B3 is required for female fertility and is dispensable for mitosis like Cyclin B. *Genes Dev* **12,** 3741–3751 (1998).
31. Sibon, O. C., Stevenson, V. A. & Theurkauf, W. E. DNA-replication checkpoint control at the Drosophila midblastula transition. *Nature* **388,** 93–97 (1997).
32. Conduit, P. T., Wainman, A., Novak, Z. A., Weil, T. T. & Raff, J. W. Re-examining the role of Drosophila Sas-4 in centrosome assembly using two-colour-3D-SIM FRAP. *Elife* **4,** 1032 (2015).
33. Blachon, S., Gopalakrishnan, J., Omori, Y., Polyanovsky, A., Church, A., Nicastro, D., Malicki, J. & Avidor-Reiss, T. Drosophila asterless and vertebrate Cep152 Are orthologs essential for centriole duplication. *Genetics* **180,** 2081–2094 (2008).
34. Baumbach, J., Novak, Z. A., Raff, J. W. & Wainman, A. Dissecting the function and assembly of acentriolar microtubule organizing centers in Drosophila cells in vivo. *PLoS Genet* **11,** e1005261 (2015).